

Diss. ETH No. 15875 and
ETHZ-IPP Internal Report 2005-01



Heavy quarks in photoproduction at HERA and a linking algorithm for the Fast Track Trigger

A dissertation submitted to the
Swiss Federal Institute of Technology Zurich
for the degree of
Doctor of Natural Sciences

presented by

David Meer

Dipl. Phys. ETH
born on April 10, 1973
citizen of Eriswil (BE)

accepted on the recommendation of
Prof. Dr. Ralph Eichler, examiner and
Prof. Dr. Günther Dissertori, co-examiner

February 2005

Abstract

The first part of this thesis describes a measurement of heavy quark production at the ep collider HERA. The analysis is based on a data set with an overall integrated luminosity of $\mathcal{L} = 52.5 \text{ pb}^{-1}$, recorded during the years 1999 and 2000. Only photoproduction events where the scattered electron is detected are considered.

To detect events with heavy quarks their finite lifetime is exploited. Therefore secondary vertices of hypothetical heavy quark decays are searched for in events with two jets. The analysis is restricted to the kinematical region of $Q^2 < 0.01 \text{ GeV}^2$, $0.28 < y < 0.65$, $E_T^{\text{jet}_1(\text{jet}_2)} > 9(7) \text{ GeV}$ and $|\eta_{\text{jet}}| < 1$. In this region the measured production cross section is $\sigma(ep \rightarrow e'c\bar{c}X \rightarrow e'\text{jet}_1\text{jet}_2X') = [452 \pm 44(\text{stat.}) \pm 109(\text{syst.})] \text{ pb}$ for charm and $\sigma(ep \rightarrow e'b\bar{b}X \rightarrow e'\text{jet}_1\text{jet}_2X') = [65.1 \pm 9.1(\text{stat.}) \pm 24.2(\text{syst.})] \text{ pb}$ for beauty events. The prediction of the next-to-leading order calculations in the model of quantum chromo-dynamics is compatible with both measured values.

The second part of this thesis covers the functionality and implementation of the L2 linker algorithm for the new Fast Track Trigger. This trigger is one of the important upgrade projects of the H1 detector within the scope of the luminosity upgrade to HERA-II. It allows to form a detector readout decision in real-time based on reconstructed charged particle tracks. The described L2 linking algorithm is one of the important components to derive precise particle tracks using analog drift chamber signals.

Zusammenfassung

Der erste Teil dieser Arbeit beschreibt die Produktion von schweren Quarks am ep Beschleuniger HERA. Die Analyse basiert auf dem Datensatz mit einer totalen integrierten Luminosität von $\mathcal{L} = 52.5 \text{ pb}^{-1}$, der mit dem H1 Detektor während der Jahre 1999 und 2000 aufgezeichnet wurde. Nur Photoproduktionsereignisse werden berücksichtigt, bei denen das gestreute Elektron detektiert wurde.

Um Ereignisse mit schweren Quarks zu detektieren wird deren endliche Lebensdauer ausgenutzt. Dazu wird in Ereignissen mit zwei Jets nach sekundären Vertizes von möglichen Zerfällen schwerer Quarks gesucht. Die Analyse ist auf den kinematischen Bereich $Q^2 < 0.01 \text{ GeV}^2$, $0.28 < y < 0.65$, $E_T^{\text{Jet}_1(\text{Jet}_2)} > 9(7) \text{ GeV}$ und $|\eta_{\text{Jet}}| < 1$ beschränkt. In diesem Bereich ist die gemessene Produktionsrate für Charm $\sigma(ep \rightarrow e'c\bar{c}X \rightarrow e'\text{Jet}_1\text{Jet}_2X') = [452 \pm 44(\text{stat.}) \pm 109(\text{syst.})] \text{ pb}$ und für Beauty Ereignisse $\sigma(ep \rightarrow e'b\bar{b}X \rightarrow e'\text{Jet}_1\text{Jet}_2X') = [65.1 \pm 9.1(\text{stat.}) \pm 24.2(\text{syst.})] \text{ pb}$. Die Vorhersage der Berechnung in nächstführender Ordnung im Modell der Quantenchromodynamik ist kompatibel mit beiden gemessenen Werten.

Der zweite Teil der Arbeit beschreibt die Funktionalität sowie die Implementierung des L2 Linkingalgorithmus für den neu gebauten schnellen Spurtrigger. Dieser Spurtrigger ist eines der wichtigsten Aufrüstprojekte des H1 Detektors im Rahmen der Luminositätssteigerung auf HERA-II. Mit ihm können Ausleseentscheide für den Detektor aufgrund von rekonstruierten Teilchenspuren in Echtzeit getroffen werden. Der beschriebene L2 Linkingalgorithmus ist dabei eine wichtige Komponente, um von analogen Driftkammersignalen auf präzise Teilchenspuren zu kommen.

Contents

List of Figures	viii
List of Tables	x
Introduction	1
1 The H1 experiment at HERA	3
1.1 The HERA ring accelerator	3
1.2 The H1 detector	4
1.2.1 Central tracking chambers	4
1.2.2 Calorimeter	6
1.2.3 Luminosity system	7
1.3 Detector simulation	7
1.4 Parametrization of a track in the H1 coordinate system	7
I Inclusive measurement of heavy quarks in tagged photoproduction	9
2 Photoproduction at H1 (Theory)	10
2.1 Kinematical description of the ep scattering	10
2.2 From QED to QCD	12
2.3 Photoproduction	13
2.3.1 Resolved processes	14
2.4 Production of heavy quarks	15
2.5 Fragmentation and hadronization	16
2.5.1 Lund model of string fragmentation	16
2.5.2 Peterson fragmentation	16
2.6 Monte Carlo Event Generator	16
3 Analysis Method	18
3.1 General introduction to this analysis	18
3.1.1 Lifetime of hadrons with heavy quarks	19
3.1.2 Analysis method	19
3.2 Kinematical variables	20
3.3 Jet reconstruction	22
3.3.1 The longitudinal invariant k_T jet algorithm	22
3.3.2 Resolved contribution and jets	23
3.4 Secondary vertex finder	26
3.4.1 Deterministic annealing	26
3.4.2 Adaptive vertex fitter	27
3.4.3 Extraction of the heavy quark fraction	30

4	Event selection	31
4.1	Tagged photoproduction	31
4.1.1	Acceptance of electron tagger	31
4.1.2	Level 1 Trigger	32
4.1.3	Luminosity calculation	34
4.1.4	Level 4 trigger	34
4.2	Non <i>ep</i> background suppression	35
4.3	Jet selection	36
4.3.1	Jet pedestal	37
4.3.2	Jet cut on generator level	40
4.4	Comparison of data and MC events for base selection	44
4.4.1	Resolved contributions from MC events	44
4.5	Secondary vertex	48
4.5.1	Strangeness suppression	48
4.5.2	Comparison of MC with data for vertexing	48
4.5.3	Extraction of the flavour fractions	54
5	Results	56
5.1	Cross section for the acceptance region	56
5.2	Systematic uncertainties	57
5.3	Additional cross-checks	58
5.4	Comparison with other measurements	59
5.5	Summary and Outlook	59
II	The L2 linking algorithm of the Fast Track Trigger FTT	62
6	FTT introduction	63
6.1	The HERA luminosity upgrade	63
6.2	The H1 trigger system	64
6.2.1	Dead-time free Level 1	65
6.2.2	Starting readout at Level 2	65
6.2.3	Abort readout on Level 3	65
6.2.4	Event filtering and online reconstruction at Level 4 & 5	65
6.3	Concept of the FTT	66
6.3.1	Track segment finding on level 1	67
6.3.2	Track segment linking and fitting on level 2	68
6.3.3	Search for particle resonances on level 3	68
7	Hardware for the FTT	69
7.1	Hardware for trigger level 1	69
7.2	Hardware for trigger level 2	72
7.2.1	Multifunctional processor board	73
7.2.2	Piggyback cards	76
7.2.3	Message system	77
7.3	Hardware for trigger level 3	78
7.4	Key technology	79
7.4.1	Logic element	79
7.4.2	Embedded system blocks	80
7.4.3	Phase-locked loops (PLLs)	81
7.4.4	Software tools for developers	81
7.5	Overall FTT simulation	81

8	The L2 Linking Algorithm	82
8.1	Functional description of the L2 linker	82
8.1.1	General requirements	82
8.1.2	The κ - ϕ histogram	82
8.1.3	Pipelined linking process	85
8.1.4	Evaluation of the link quality matrix	87
8.1.5	Message generator	87
8.2	The VHDL implementation	88
8.2.1	The core of the L2 linker	89
8.2.2	Peripheral connection	91
8.2.3	Place and route	92
	Bibliography	95
A	Data analysis	100
A.1	Definition of the subtrigger 83	100
A.2	Alternative jet cuts on generator level	101
B	Technical specification of the FTT L2 linker	102
B.1	L2 linker memory	102
B.2	Assignment of data and control lines	104
B.3	Long search seed format	105
	Danksagung	106
	Curriculum Vitae	107

List of Figures

1.1	The HERA storage ring (left) and the pre-accelerators (right) at DESY.	4
1.2	View of the H1 detector and the definition of the coordinate system.	5
1.3	Side view of the H1 tracking system.	6
1.4	The H1 luminosity system.	7
1.5	Definition of the track parameters κ , ϕ_0 , θ , d_{ca} and z_0 in the H1 coordinate system.	8
2.1	Neutral current and charged current process of ep scattering	11
2.2	Feynman diagram for a direct and a resolved process.	14
2.3	Factorization of heavy quark production for resolved photoproduction.	15
3.1	Decay length distribution for charm and beauty hadrons	20
3.2	Correlation of y_{ET} and y_{JB} and the relative difference.	22
3.3	Correlation and the relative difference of x_γ^{gen} and x_γ^{rec}	24
3.4	Reconstructed x_γ distribution for different jet cuts.	25
3.5	Reconstructed x_γ for resolved and direct processes.	25
3.6	Charged track multiplicity for charm and beauty hadron decays in MC events.	26
3.7	Definition of vertexing parameters.	27
3.8	Definition of the sign of the impact parameter d	28
3.9	Example of a secondary vertex with a vertex multiplicity of 4 tracks.	29
4.1	Acceptance of the electron tagger.	32
4.2	L4 classification of selected events.	35
4.3	Distribution of the z vertex for MC events and data.	36
4.4	Jet profiles for several bins in jet rapidity.	37
4.5	Rapidity slice with a jet cone and the area for jet pedestal measurement.	38
4.6	Energy of jet pedestal as function of the jet rapidity.	38
4.7	Radius of a cone around the jet axis containing a fraction of the total jet energy.	39
4.8	Distribution of the first radial moment M_r^1	40
4.9	Distribution of the jet mass.	41
4.10	Jet E_T spectra measured at the generator level.	41
4.11	Correlation between \hat{p}_T and the jet energy.	42
4.12	Correlation between E_T of jets on generator level and after H1SIM.	43
4.13	Distribution of inelasticity and longitudinal hadronic energy.	44
4.14	Distribution of the transverse jet energy E_T and the jet rapidity η	45
4.15	Distribution of the jet rapidity η forward / backward.	46
4.16	Distribution of x_γ for the selected kinematical region.	46
4.17	Distribution of x_γ after downscaling resolved MC events by 25%.	47
4.18	Relation of the d'_{ca} point of a track and the angle between the jet axis.	49
4.19	Number of tracks and number of well measured tracks in the jet.	49
4.20	Track multiplicity of secondary vertices found by the adaptive vertex fitter.	50
4.21	Distributions of l , σ_l and S_l of all secondary vertices with at least one track.	51
4.22	Distributions of l , σ_l and S_l for each vertex multiplicity.	52

4.23	Invariant mass distribution of vertices.	53
4.24	Simultaneous fit of vertices with a multiplicity of 1, 2 and 3 or more tracks.	55
5.1	Data over theory for the beauty cross section.	60
6.1	The multi-level trigger system of H1	64
6.2	The CJC1/CJC2 in the r - ϕ plane showing the four trigger layers.	67
7.1	Overview of the hardware implementation of the FTT.	70
7.2	Device placement on a FEM	71
7.3	Functional block diagram of the MPB with four connected piggybacks.	74
7.4	Device placement of the MPB. Dotted devices are mounted on the bottom side.	75
7.5	Eye diagram of the bidirectional signal between the main board and a piggyback.	76
7.6	Device placement on a piggyback card.	77
7.7	A LFSR with feed-back signals tapped from the second, fourth, and last register.	77
7.8	Example of a routing table in the Data control FPGA.	78
7.9	Schematic view of a logic element from a FPGA	79
7.10	Example of a combination of a CAM with a RAM to implement a lookup table LUT.	80
8.1	Sliding window technique	83
8.2	Storage of a track segment in the virtual κ - ϕ histogram.	84
8.3	Linking of track segments within the virtual κ - ϕ histogram.	86
8.4	Adaptation of the sub array number.	86
8.5	Entities of the data controller FPGA of the L2 linker card.	88
8.6	Block diagram of the L2 linker core.	89
8.7	State machine of the Fpga.Ctrl entity.	92
8.8	Simulation of a L2 linking cycle with some showcase data.	94

List of Tables

1	Properties of the fermions in the standard model	1
2	Interactions in the standard model	1
1.1	Important design parameters of HERA.	3
2.1	Calculated cross section in NLO for charm and beauty production in ep -scattering.	15
2.2	Sets of MC events used in this analysis.	17
2.3	Lifetime, mass and fragmentation fraction of charm and beauty hadrons.	17
4.1	Efficiency of dedicated TE of the subtrigger 83.	33
4.2	Integrated luminosity of the analyzed data set	34
4.3	Definition of Jet phase space.	36
4.4	Jet cuts applied on generator level before simulation and reconstruction.	42
4.5	Track selection cuts for vertexing.	48
5.1	Definition of the visible kinematical region for the cross section	56
5.2	Summary of systematic uncertainties.	57
5.3	Relative variation of the cross section under additional cross-checks.	58
5.4	Visible cross section for different methods and the results of the NLO calculation.	59
6.1	Expected level 1 prescale factors before and after the luminosity upgrade	66
6.2	Tasks, trigger decision, and technology on the three FTT trigger levels.	66
6.3	Subset of CJC wires used as input for the FTT.	67
7.1	Time budget at level 1 of FTT.	72
7.2	Possible configuration of the MPB	73
8.1	Simulated multiplicity of sub array number for 128 track segments.	85
8.2	The weight matrix of a sliding 3×3 window.	85
8.3	Priority of track segments from the same trigger layer within a 3×3 sliding window.	85
8.4	Conditions for switching the L2 linker mode.	91
8.5	Splitting of the piggyback data bus in the command mode	92
8.6	Usage of embedded system blocks (ESB) in FPGA.	93
8.7	Performance of the L2 linker.	93
A.1	Accepted events for several jet cuts after reconstruction.	101
B.1	Configuration of the Seed RAM.	102
B.2	Configuration of a CAM.	102
B.3	Configuration of the Tag RAM.	103
B.4	Configuration of the Seed RAM.	103
B.5	Data format of unlinked track segments.	104
B.6	Data format of L2 messages containing linked track segments.	104
B.7	Assignment of the control lines between the piggyback card and the data controller.	104

B.8	Assignment of the control lines between the DSP controller and the data controller.	105
B.9	Binary representation of the CAM number in the <i>long CAM number</i> format. . . .	105

Introduction

The discovery of the J/ψ meson [1, 2] in 1974 was a big success for particle physics and after the interpretation as a bound state of a new quark-antiquark pair, it marked the beginning of heavy quarks in the history of particle physics. The discovery completed the picture of the second generation of quarks and was so "charming" that this new quark was called *charm*. With the help of the quark model, the puzzling and manifold spectra of hadrons discovered during the previous ten years could be explained.

Only three years later the *beauty* quark was discovered [3, 4] which established the third generation of even more massive quarks. The third generation is completed with the *top* quark discovered in 1995 [5, 6].

Today, the understanding of the basic building blocks of matter and the forces between them is summarized by the standard model of particle physics. This model describes matter and its interaction by forces at a fundamental level. The components of matter are fermions (quarks and leptons), with properties shown in table 1. Three different forces¹ describe the interaction

Generation	Quarks			Leptons		
	Flavour	Charge (e)	Mass [GeV/ c^2]	Flavour	Charge (e)	Mass [MeV/ c^2]
1st	u	+2/3	0.0015 – 0.004	ν_e	0	$< 3 \cdot 10^{-6}$
	d	-1/3	0.004 – 0.008	e^-	-1	0.5110
2nd	c	+2/3	0.08 – 0.13	ν_μ	0	< 0.19
	s	-1/3	1.15 – 1.35	μ^-	-1	105.66
3rd	t	+2/3	178	ν_τ	0	< 18.2
	b	-1/3	4.1 – 4.4	τ^-	-1	1777

Table 1: Properties of the fermions in the standard model [7]. Values for quark masses depend on the underlying theoretical model.

between these fermions by an exchange of gauge bosons. Properties of the different interactions are summarized in table 2.

Interaction	Gauge boson(s)	Relative strength	Range [m]	Participating fermions
strong	gluons (g)	1	$\leq 10^{-15}$	quarks
electromagnetic	photon (γ)	10^{-2}	∞	all charged
weak	W^\pm, Z^0	10^{-6}	10^{-18}	all
gravitational	[graviton (G)]	10^{-39}	∞	all

Table 2: Interactions in the standard model and the corresponding gauge bosons. The relative strengths of the forces are roughly given for short distance scales of a few fm.

In this analysis, the production of heavy quarks (charm and beauty) at the e^+p collider HERA is studied in the kinematical range of photoproduction using the data collected with the H1

¹Since there is no quantized renormalizable theory of gravity in the standard model, the graviton has to be considered a hypothetical particle.

detector during the years 1999 and 2000. The experimentally measured value for the production rate can be compared with the next-to-leading order (NLO) quantum chromo-dynamic (QCD) calculation as a test for the prediction of the standard model. It is naively expected that the NLO calculation is more reliable for beauty production than for the production of charm because the larger mass of the beauty quark provides a harder scale than the charm quark. Consequently, the condition for a perturbative treatment of QCD is better fulfilled for beauty than for charm events. However, a large number of measurements of the charm production rate show quite a good agreement between the measured cross section and the perturbative calculation. On the other hand, the NLO calculation of the beauty cross section provides a value which is significantly lower than several older measurements, in particular for the kinematical region of photoproduction.

Motivated by this discrepancy, the present analysis uses a new method to measure the total cross section for charm and beauty production at HERA. The inclusive method of this analysis aims for a reconstruction of the secondary vertex of a decaying hadron with a heavy quark due to their long lifetime. Older measurements of the beauty cross section are mainly based on the signature of semi-leptonic decays of beauty hadrons.

The present thesis is organized in two parts. Part one reports the results of the data analysis while in part two a hardware upgrade project of the H1 detector is presented.

After a presentation of the HERA accelerator and the H1 detector in the first chapter, the next three chapters of the thesis are dedicated to the analysis of the heavy quark production. In chapter 2 the theoretical background for the production of heavy quarks and the prediction of the NLO calculation are provided. Chapter 3 starts with a motivation for the method of secondary vertices used in this analysis. Afterwards, two algorithms relevant for this analysis are presented: The longitudinal invariant k_T algorithm which is applied to identify jets and an adaptive vertex fitter used to find secondary vertices in an event. In the next chapter the selection of events with a secondary vertex is explained. First, tagged photoproduction events which have a two-jet signature with a sufficient hard scale are chosen. Then, the efficient implementation of a similar jet requirement for simulated event and the problem of jet pedestals are discussed. The first part of this thesis ends with chapter 5 in which the results of the measured cross section are presented. Systematic errors and the comparison with the results of other measurements are also discussed.

Today's experiments in high energy physics are impracticable without complex and large particle detectors. The maintenance and operation of such a detector is the basis for a successful data analysis. Many detector components are based on latest developments in technology and often have an impact to innovations in industry. For this reason, part two is dedicated to a hardware development for the upgrade of the H1 detector which was a major part of this work. In this part, the level two linking algorithm of the Fast Track Trigger (FTT) and the required hardware are described.

First, the luminosity upgrade of the HERA accelerator and the upgrade projects for the H1 detector are presented. In addition, an overview is given on the H1 trigger system and the Fast Track Trigger (FTT) which is an upgrade project of the existing trigger system. In the next chapter the actual hardware of the FTT is described. It focuses mainly on the hardware for level two of the FTT which was developed in collaboration with a private company. The last chapter of part two describes in detail the level two linking algorithm of FTT. This chapter starts with a general specification of the algorithm and ends with the description of the algorithm's implementation for a programmable logic device.

Chapter 1

The H1 experiment at HERA

The HERA¹ ring accelerator is situated at the research center DESY² in Hamburg. The configuration of colliding electron-proton beams is up to now unique in the world and allows studies of physical processes in a wide kinematical range. An outline of the experimental setup of the H1 experiment at the HERA storage ring is given in the subsequent chapter. The description corresponds to the status of the detector during the years 1999 and 2000 which is the relevant period for this analysis. Activities about the detector upgrade for the luminosity upgrade during the year 2001 are summarized in section 6.1.

1.1 The HERA ring accelerator

Protons and electrons³ are pre-accelerated in various older systems and are injected to the HERA ring where they are accelerated to their final energy. The HERA collider consists of the electron storage ring and the superconducting proton ring with a circumference of 6.3 km each.

The two particle beams are brought to collision at two interaction points where the two detectors of the H1 and the ZEUS experiments are located (see figure 1.1). This allows the analysis of proton-lepton scattering at a center-of-mass energy of $\sqrt{s} = 318$ GeV. Some additional characteristics of the HERA ring accelerator are given in table 1.1.

	<i>e</i> -beam	<i>p</i> -beam
Injection energy	12 GeV	40 GeV
Final beam energy	27.5 GeV	920 GeV
Magnetic bending field	0.165 T	4.68 T
Number of colliding bunches	174	174
Maximal beam current	50 mA	100 mA
Number of particles in bunch	$3.5 \cdot 10^{10}$	$7.3 \cdot 10^{10}$
Transverse beam dimensions	$192 \mu\text{m} \times 50 \mu\text{m}$	$189 \mu\text{m} \times 50 \mu\text{m}$
Beam collision rate	$10.4 \text{ MHz} = (96 \text{ ns})^{-1}$	
Luminosity	$1.69 \cdot 10^{31} \text{ cm}^{-2}\text{s}^{-1}$	
Center of mass energy	$\sqrt{s} = 318 \text{ GeV}$	

Table 1.1: Important design parameters of HERA.

In addition to the collider experiments there are two beam-target experiments which make use of only one particle beam. The HERMES experiment scatters the electron beam on a polarized

¹Hadron Elektron Ring Anlage

²Deutsches Elektronen Synchrotron

³The machine can run with either positrons or electrons. Since there is no need to distinguish the lepton charge in this analysis, the lepton beam is referred to as the electron beam from now on.

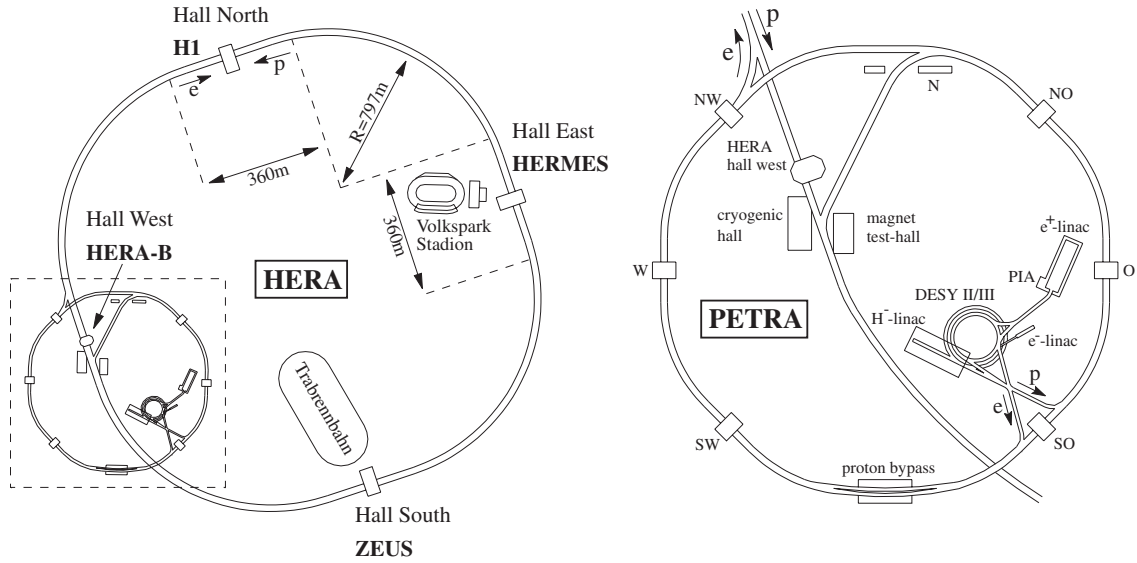


Figure 1.1: The HERA storage ring (left) and the pre-accelerators (right) at DESY.

gas target while the HERA-B experiment inserts a wire target into the proton beam.

1.2 The H1 detector

The H1 detector is a general purpose particle detector which surrounds almost completely the northern interaction region of HERA. The detector has a symmetric design with respect to the beam line but due to the different momenta of electron and proton the detector is substantially better instrumented in the direction of flight of the protons. A schematic view of the H1 detector is shown in figure 1.2.

The righthanded coordinate system used by H1 has its origin at the nominal interaction point and the z -axis is parallel to the direction of the proton beam. The azimuthal angle ϕ is defined with respect to the x -axis which is pointing to the center of the HERA ring, while the polar angle θ is defined with respect to z -axis.

The following subsections provide a short description of the detector components which were essential for this data analysis. The complete description of the H1 detector can be found in [8, 9].

The crucial component for data acquisition is the trigger system which allows to filter good events with high selectivity. More details on the H1 trigger system are given in section 6.2 on page 64.

1.2.1 Central tracking chambers

The central tracking system is concentrically arranged around the beam line and consists of a set of different detectors, their placement is shown in figure 1.3.

In the homogenous magnetic field of 1.14 T of the surrounding superconducting solenoid, tracks are bent according to their transverse momentum and charge. Of major importance for track reconstruction is the *central jet chamber* (CJC), designed to measure charged particles with high precision [10]. It consists of an inner (CJC1) and an outer (CJC2) chamber subdivided in the azimuthal direction by planes of cathode wires into 30 (60) cells with 24 (32) anode sense wires each. A charged particle passing through the chambers ionizes the Ar-CO₂-CH₄-gas along its track and the produced electron cloud drifts in the applied electrical field to the sense wires. By measuring these drift times for each sense wire the track of the particle can be reconstructed very precisely. Even a coarse measurement of the z -coordinate is possible by measuring the charge

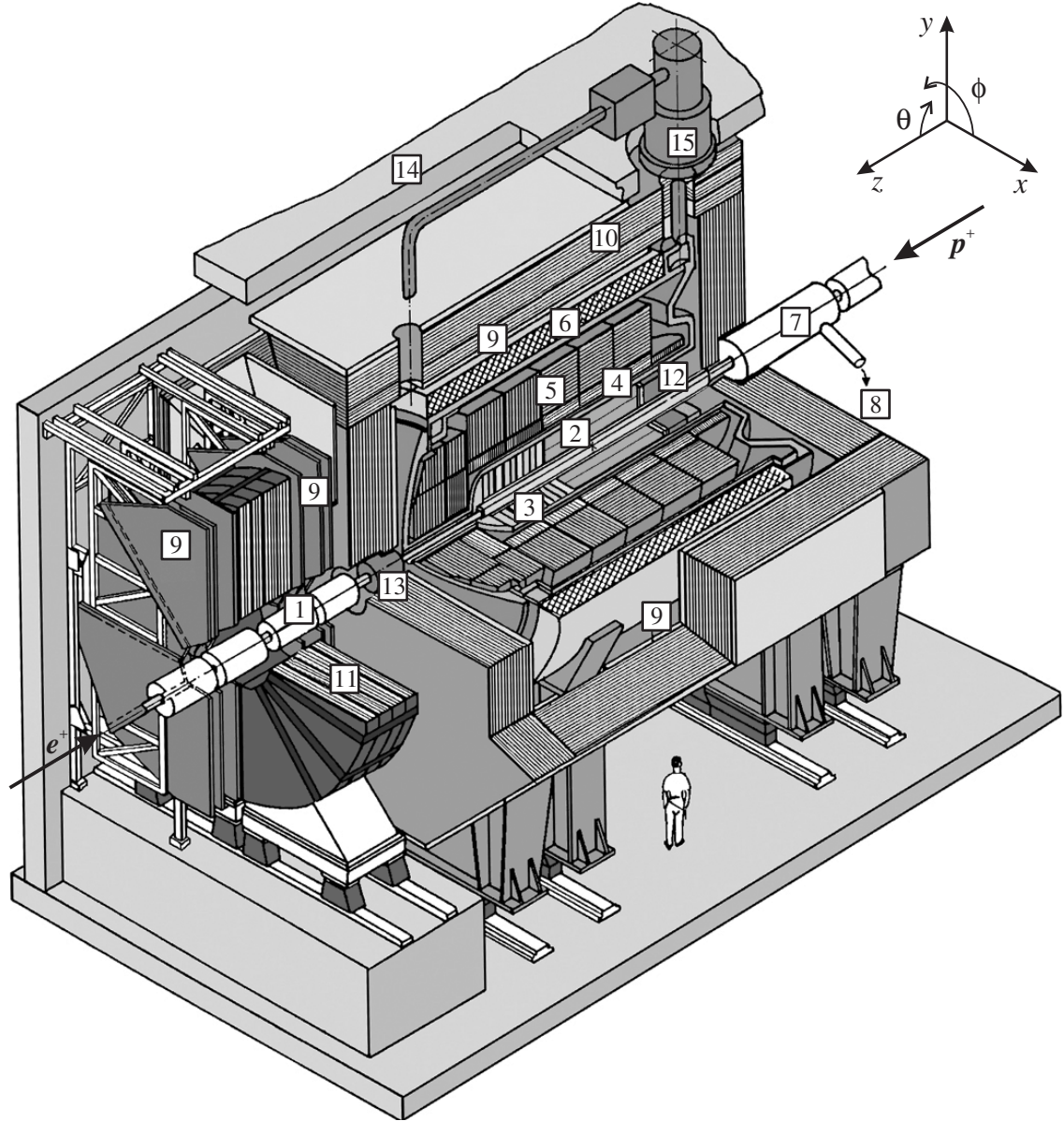


Figure 1.2: View of the H1 detector and the definition of the coordinate system. Legend:
 [1] Beam pipe and beam magnets, [2] Central tracking chambers, [3] Forward tracking and Transition radiators, [4] Electromagnetic Calorimeter, [5] Hadronic Calorimeter, [6] Superconducting coil, [7] Compensating magnet, [8] Helium cryogenics, [9] Muon chambers, [10] Instrumented Iron, [11] Muon toroid magnet, [12] Backward calorimeter, [13] Plug calorimeter, [14] Concrete shielding, [15] Liquid Argon cryostat

division at the end of a sense wire. The resolution in the $r\phi$ plane is $\sigma_{r\phi} = 0.17$ mm and in z direction $\sigma_z = 22$ mm.

The resolution in z is drastically improved by the *inner* (CIZ) and *outer* (COZ) z -chambers which have sense wires perpendicular to the beam axis [11].

Fast timing information is delivered by the *inner* (CIP) and *outer* (COP) *multiwire proportional chambers* [12]. This information is mainly used by the trigger level 1 and 2 to identify ep vertices in the nominal interaction region and to reject outlying background events.

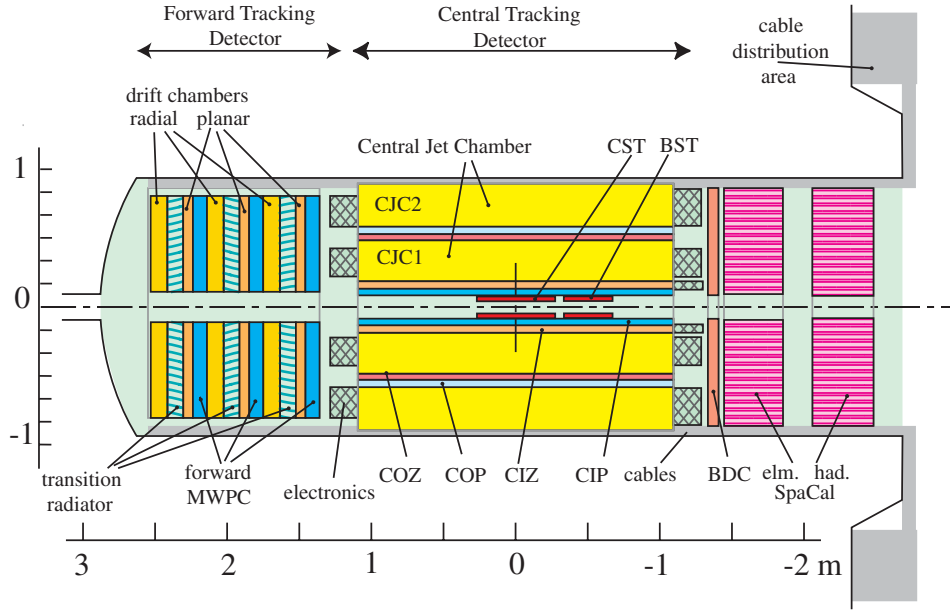


Figure 1.3: Side view of the H1 tracking system. The central tracking system is extended by multiwire proportional chambers (MWPC), transition radiators and drift chambers in forward direction as well as a backward silicon tracker (BST) and a backward drift chamber (BDC) in backward direction.

Silicon tracker

The detector component at closest radial distance to the nominal interaction point is the *central silicon tracker* (CST). It is made up of two layers of silicon strip detectors at radii of 57.5 mm and 97.5 mm, respectively [13]. A polar angle range of $30^\circ < \theta < 150^\circ$ is covered by the CST.

The double-sided silicon strip sensors allow in principle exact three-dimensional spatial information which is essential for precise determination of charged tracks close to the interaction point. This precision is indispensable for heavy flavour analysis – like this analysis – which identifies tracks from a secondary vertex with a separation to the primary vertex of some hundred micrometers. The intrinsic hit resolution of the CST in the $r\phi$ projection is $12 \mu\text{m}$ and in the z -direction minimal $22 \mu\text{m}$, depending on the polar angle of the track.

1.2.2 Calorimeter

The central tracking chambers are surrounded by the Liquid Argon (LAr) calorimeter [14] which is the other principal detector component apart from the CJC. The LAr calorimeter consists of the outer hadronic and the inner electromagnetic calorimeter and covers a polar angular range of $4^\circ < \theta < 154^\circ$. Lead plates are used as absorber material in the hadronic calorimeter which results in a total thickness of 4 to 8 nuclear interaction lengths λ , while in the electromagnetic part steel plates are used giving a thickness of 20 to 30 radiation lengths X_0 . Due to the fine segmentation of the calorimeter a good energy and also spatial resolution is achieved which is $\sigma_E/E = 12\%/\sqrt{E [\text{GeV}]} \oplus 1\%$ for the electromagnetic and $\sigma_E/E = 50\%/\sqrt{E [\text{GeV}]} \oplus 2\%$ for the hadronic part.

The acceptance of the LAr calorimeter is extended in the backward region by the Spaghetti Calorimeter (SpaCal) based on lead/scintillating-fibre technology [15]. As the LAr calorimeter, also the SpaCal consists of a electromagnetic and hadronic part. The SpaCal closes the gap of acceptance in the polar angle between $153^\circ < \theta < 177.8^\circ$.

1.2.3 Luminosity system

For the measurement of the luminosity the Bethe-Heitler bremsstrahlung process $e + p \rightarrow e + p + \gamma$ which has a well known cross section is used as a reference process [16]. The scattered electron and the photon are detected with the electron tagger⁴ (ET) and the photon tagger (PD), respectively. The ET is a 49 channel crystal Cherenkov calorimeter with a size of 154×154 mm located at $z = -33.4$ m along the beam pipe (see figure 1.4), while the PD consists of 25 channels with a size of 100×100 mm at $z = -103.1$ m. Both detectors have a depth of 20 cm which corresponds to 20 radiation lengths X_0 .

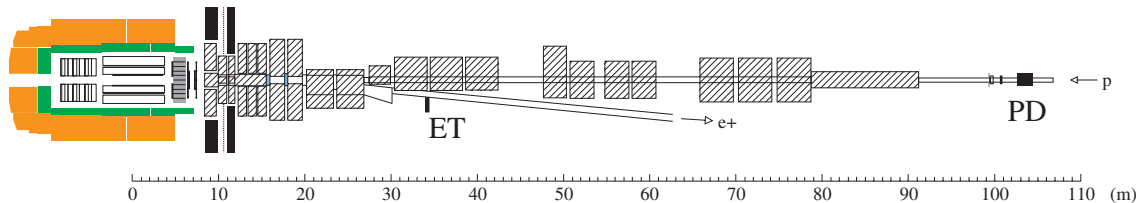


Figure 1.4: Top view on the H1 luminosity system with electron tagger (ET) and photon detector (PD).

Besides the luminosity measurement the electron tagger can be used to detect the scattered electron in photoproduction events with a squared momentum transfer $Q^2 < 10^{-4} \text{ GeV}$ as is applied in this analysis. In this case of "tagged photoproduction" the electron tagger covers – with variable acceptance – the kinematical region in inelasticity of $0.25 < y < 0.7$. The parametrization of this measured acceptance is shown in figure 4.1 on page 32. To extend the taggable y -range in both directions two additional detectors have been installed. A second electron tagger (6 channels) at $z = -43.2$ m with $0.05 < y < 0.2$ and a calorimeter (unused SpaCal elements) at $z = -8.0$ m with $0.8 < y < 0.95$.

1.3 Detector simulation

When comparing theory with data all detector effects must be considered. Besides these detector effects like limited acceptance or resolution also the non perturbative hadronization process must be included. This is done by comparing data to artificial events generated by a Monte Carlo (MC) event generator. The MC generator includes the calculation of the hard process and the phenomenological fragmentation.

The bulk of the detector response on events generated by Monte Carlo programs is simulated with the H1SIM simulation program. This package works within the GEANT framework which includes the fundamental interaction of particles with matter like multiple scattering, energy loss and secondary particle production. Since the detector is modified at times and due to the change of calibration parameters, the simulation is also a function of time.

After the simulation step the same reconstruction algorithms as for data are applied to the simulated events. Simulated and reconstructed events are used to study detector efficiencies and purity of data samples.

1.4 Parametrization of a track in the H1 coordinate system

Tracks of charged particles are bent in the homogenous magnetic field and can be described by a helix along the z -axis. Five track parameters are needed to define this helix. The following track parameters are used at H1 (see also figure 1.5):

⁴Until the year 1997 the coincidence of electron tagger *and* photon detector was required to measure the luminosity. Afterwards only the photon detector has been used due to its smaller systematic error.

- κ Curvature of a track. The sign of the curvature is negative for a positive charged particle and vice versa. The curvature is related to the transverse momentum p_T of a track by

$$p_T = 0.003 \cdot \frac{B_z \text{ GeV}}{\kappa \text{ T cm}}, \quad (1.1)$$

whereas $B_z = 1.14 \text{ T}$ denotes the homogenous magnetic field along the z -axis.

- ϕ_0 Azimuthal angle between a track at the d_{ca} -point and the positive x -axis. The range of the azimuthal angle is $-180^\circ < \phi < 180^\circ$.
- θ Polar angle of the track with reference to the z -axis. The range of the polar angle is $0^\circ < \phi < 180^\circ$. With this convention, a particle with a track parallel to the proton beam has a polar angle of $\theta = 0^\circ$ and the polar angle is $\theta = 180^\circ$ if the track is parallel to the electron beam.
- d_{ca} Distance of closest approach between a track and the H1 origin in the xy -plane. The sign is positive if the vector pointing from the origin to the d_{ca} -point, the momentum vector at the d_{ca} -point and the positive z -axis form a right-handed system and is negative for a left-handed system.
- z_0 The track's z -coordinate at the d_{ca} -point.

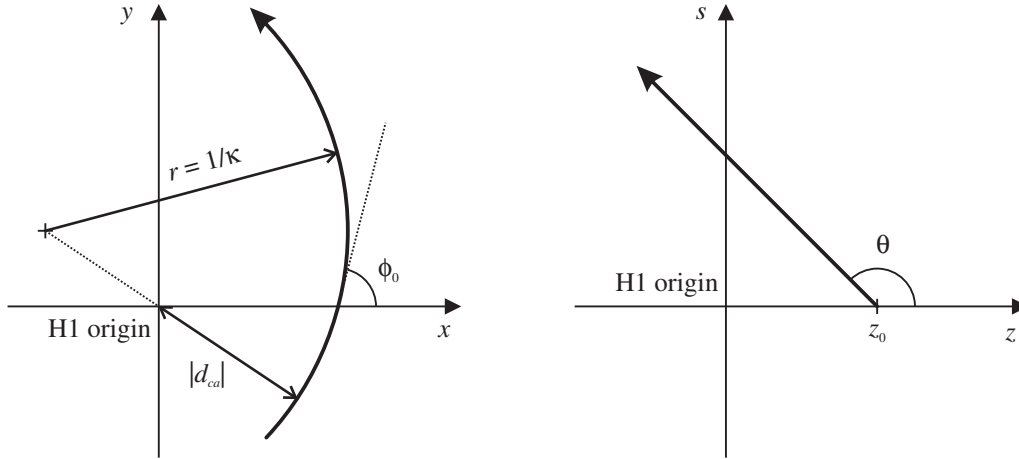


Figure 1.5: Definition of the track parameters κ , ϕ_0 , θ , d_{ca} and z_0 in the H1 coordinate system. The parametrization variable is s .

In principle, different sets of track parameters can be used. Among these sets of parameters the most appropriate set to parameterize tracks in the H1 environment was selected. With this set a track can be parameterized with the parametrization variable s as

$$\begin{aligned} x(s) &= + \left(d_{ca} - \frac{1}{\kappa} \right) \cdot \sin(\phi_0) + \frac{1}{\kappa} \cdot \sin(\phi_0 + \kappa \cdot s) \\ y(s) &= - \left(d_{ca} - \frac{1}{\kappa} \right) \cdot \cos(\phi_0) - \frac{1}{\kappa} \cdot \cos(\phi_0 + \kappa \cdot s) \\ z(s) &= z_0 + \frac{s}{\tan(\theta)}. \end{aligned} \quad (1.2)$$

Note that the parametrization (1.2) is equal to the d_{ca} point for $s = 0$.

Part I

Inclusive measurement of heavy quarks in tagged photoproduction

Chapter 2

Photoproduction at H1 (Theory)

In the standard model, the strong interaction is described by the theory of quantum chromodynamics (QCD), which describes the interaction between quarks by the exchange of gluons. This theory provides the fundamental laws for the description of the strong interaction on parton (quarks and gluons) level. With a particle detector only the hadronic final state of particle interactions can be measured. However, it is not possible to calculate the cross sections for such a final state from these first principles. Within its range of validity, perturbative QCD (pQCD) is one successful approach to calculate cross sections for processes which are detectable with a particle detector and allows to compare data to theory. In pQCD the strong coupling α_s is used as expansion parameter of the perturbation series. The convergence of this series is only ensured if α_s is small. Since the value of α_s is decreasing by increasing the hardness of an interaction, the presence of a hard scale is required in pQCD. A hard scale can be the mass of heavy quarks or the transverse momentum of an interaction. It is expected that pQCD is able to predict the production rate for heavy quarks. Therefore, the study of heavy quark production allows various tests of pQCD.

This chapter starts with the introduction of the kinematical variables used to describe the electron-positron scattering at HERA. Then a motivation for the necessity of QCD is given and the production rate of heavy quarks in photoproduction is formulated in the framework of pQCD. After this, hadronisation of heavy quarks to objects which can be observed by the detector is discussed. At the end of the chapter a description of the MC event generator used in this analysis is given.

2.1 Kinematical description of the ep scattering

At the HERA collider the scattering of electrons on a proton beam is used to probe the structure of the proton. In lowest order of perturbation theory the scattering is described by exchanging either a neutral electroweak boson (γ, Z^0) or the charged W^\pm boson. The scattering process with the exchange of an uncharged boson is called *neutral current* (NC) whereas the latter scattering process is referred to as *charged current* (CC). Feynman diagrams of these two processes are shown in figure 2.1. In these diagrams the abbreviation X_P stands for a not specified reaction product of the proton.

The four-momentum of the incoming electron k , the proton P and the outgoing electron or neutrino k' are used to define the square of the center-of-mass of the ep system

$$s = (P + k)^2, \quad (2.1)$$

as well as the virtuality of the exchanged boson

$$Q^2 = -q^2 = -(k - k')^2, \quad (2.2)$$

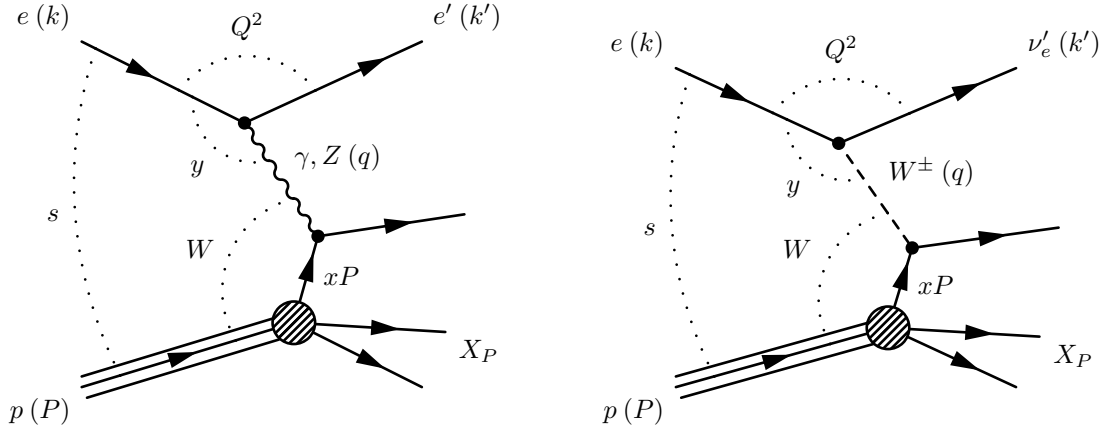


Figure 2.1: Neutral current (left) and charged current (right) process of ep scattering with annotation of the particle momentum and the basic kinematical variables.

which is equal to the negative squared momentum transfer from the lepton to the proton. In the quark-parton model the Bjorken variable

$$x = \frac{Q^2}{2P \cdot q}, \quad 0 \leq x \leq 1 \quad (2.3)$$

denotes the fraction of the proton's momentum carried by the struck quark, while the Bjorken variable

$$y = \frac{P \cdot q}{P \cdot k}, \quad 0 \leq y \leq 1 \quad (2.4)$$

describes the inelasticity. Furthermore, the center-of-mass of the boson-proton system W is defined as

$$W^2 = (P + q)^2. \quad (2.5)$$

Only three of these five lorentz invariant variables (s , Q^2 , x , y , W^2) are independent and as such sufficient to completely describe electron proton scattering. Neglecting the electron and proton masses they fulfill the following relations:

$$Q^2 = s \cdot y \cdot x, \quad (2.6)$$

$$W^2 = s \cdot y - Q^2. \quad (2.7)$$

Another important variable is the rapidity $\hat{\eta}$ of a particle defined as

$$\hat{\eta} = \frac{1}{2} \ln \left(\frac{E + p_z}{E - p_z} \right). \quad (2.8)$$

A property of the rapidity is that differences in rapidity $\Delta\hat{\eta} = |\hat{\eta}_1 - \hat{\eta}_2|$ are invariant under lorentz boosts along the z -axis. Neglecting the mass of the particle, the pseudo-rapidity η follows from equation (2.8) to

$$\eta = \frac{1}{2} \ln \left(\frac{p + p_z}{p - p_z} \right) = -\ln \left(\tan \left(\frac{\theta}{2} \right) \right). \quad (2.9)$$

The pseudo-rapidity is useful since usually the particle identity of a decay product is unknown and thus also the particle's mass is not known.

The virtuality Q^2 of the exchanged boson is used to classify ep scattering events. The regime of $Q^2 < 1 \text{ GeV}^2$ is called *photoproduction* and is the dominant scattering process due to the $1/Q^2$ dependence of the total cross section as can be seen in equation (2.10). Since the boson propagator

is proportional to $1/(Q^2 + M_B^2)$, the exchange of a massive Z^0 or W^\pm is strongly suppressed in comparison with the massless γ exchange at low Q^2 . As a consequence the γ exchange of neutral current events is the only contributing process in this regime.

The deep inelastic ep scattering (DIS) region with $Q^2 > 1 \text{ GeV}^2$ is divided in a regime *DIS at moderate* Q^2 with $1 \text{ GeV}^2 < Q^2 < 100 \text{ GeV}^2$ and a regime *DIS at high* Q^2 with $Q^2 > 100 \text{ GeV}^2$. In the first regime the cross section is still dominated by the γ exchange. Even though the cross section is smaller than in photoproduction, it is still reasonably large.

In the regime of DIS at high Q^2 the expected cross section from the standard model is small. At highest Q^2 the cross section for neutral and charged current attain the same magnitude.

2.2 From QED to QCD

Without knowing the structure of the proton the differential cross section for NC can be derived from QED [17]

$$\frac{d^2\sigma^{\text{NC}}}{dx dQ^2} = \frac{4\pi\alpha^2}{xQ^4} \cdot (y^2x \cdot F_1(x, Q^2) + (1-y) \cdot F_2(x, Q^2)), \quad (2.10)$$

where α is the electromagnetic coupling constant and $F_i(x, Q^2)$, $i = \{1, 2\}$ are the structure functions absorbing knowledge of the proton structure. In equation (2.10) the Z^0 exchange is ignored.

In the naïve quark parton model (QPM), the proton is composed of noninteracting point-like constituents with spin 1/2. Within this model the inelastic interaction of a photon with a proton can be reduced to a incoherent sum of elastic scatterings on point-like partons. Thus the structure functions $F_i(x, Q^2)$ are given in terms of the parton density functions $f_i^p(x, Q^2)$ of the proton. The parton density function (PDF) indicates the probability to find a (anti-)parton i (\bar{i}) with a momentum x at scale Q^2 in the proton and is related to the structure functions as follows:

$$F_1(x, Q^2) = \frac{1}{2} \cdot \sum_{\text{partons } i} e_i^2 \cdot (f_i^p(x, Q^2) + f_{\bar{i}}^p(x, Q^2)) \quad (2.11)$$

$$F_2(x, Q^2) = x \cdot \sum_{\text{partons } i} e_i^2 \cdot (f_i^p(x, Q^2) + f_{\bar{i}}^p(x, Q^2)) = 2 \cdot x \cdot F_1(x, Q^2). \quad (2.12)$$

Here e_i denotes the electric charge of parton i and the relation between the structure function F_2 and F_1 in equation (2.12) is called *Callan-Gross* relation.

If the strong force between quarks is neglected, the structure functions are independent of the scale Q^2 and only depend on x , thus are *scale invariant*. However, experiments showed that there is a logarithmic dependence of the structure function on Q^2 (scaling violation). Furthermore, the sum of all momenta carried by the valence partons should be equal to 1 while the measurements add up to about half of this value. These two failings are drawbacks of the QPM and are overcome in the theory of Quantum Chromodynamics (QCD).

In analogy to QED, the strong force of QCD is mediated by gauge bosons called gluons. They couple to the color which is the charge of the strong interaction. But in contrast to QED, the gluons carry color and thus can couple to each other. This is a consequence of the fact that QCD is a non-Abelian gauge theory.

To calculate the cross section in perturbative QCD, the effect of the strong force is expanded in power series of the strong coupling constant α_s . The process with lowest order in this expansion is referred to as the *leading order* (LO) process whereas *next-to leading order* (NLO) denotes processes from second order.

One of the problems when calculating cross sections are ultraviolet divergences which arise in gluon and quark loops which allow an unlimited internal momentum. Ultraviolet divergences can be absorbed by a renormalization process which leads to a running strong coupling constant. For this an arbitrary renormalization scale μ_R is introduced. In the one-loop approximation of the

renormalization group equation the following solution is provided:

$$\alpha_s(\mu_R) = \frac{12\pi}{(33 - 2n_f) \cdot \ln\left(\frac{\mu_R^2}{\Lambda_{\text{QCD}}^2}\right)}, \quad (2.13)$$

where n_f is the number of quark flavours considered in the virtual loops and Λ_{QCD} is a scale parameter in the order of 200 MeV.

Besides the ultraviolet divergences, infrared divergences arise in QCD because of its long-distance behavior. By introducing a cut-off scale μ_F processes are separated into hard interactions with a hard scale $\mu > \mu_F$ and soft processes. Hard interactions with a short distance have a small value for α_s and thus can be treated with pQCD, while the long distance interactions are absorbed in the PDFs. The consequence is a running of the renormalized PDFs $f_i^p(x, \mu_F^2)$.

Factorization allows the separation of long and short range interactions and the absorption of the large scale interactions in the PDFs. Therefore the total cross section from equation (2.10) can be written as

$$d\sigma(ep \rightarrow e'X) = \sum_{\text{partons } i} \int dx \cdot f_i^p(x, \mu_F^2) \cdot d\hat{\sigma}_i(\hat{s}, \alpha_s(\mu_R), \mu_R, \mu_F). \quad (2.14)$$

In this equation $\hat{\sigma}_i$ denotes the partonic cross section which describes the scattering of the lepton on a parton i inside the proton. The cross section depends on the center of mass energy of the photon-parton system $\hat{s} = (xP + q)^2$ and the two scales μ_R and μ_F .

Also the renormalized PDFs must fulfill the renormalization group equations. The resulting DGLAP¹ evolution equations [18, 19, 20] can be used to extrapolate the PDFs into other regions of Q^2 .

2.3 Photoproduction

In case of photoproduction with $Q^2 \rightarrow 0$ the exchanged photon is quasi-real. The description of the cross section can be simplified by factorizing the photon emission of the electron from the interaction of the photon with the parton. The probability of emitting a photon from the electron is described by the flux factor $f_\gamma^e(y)$ which can be calculated in the modified Weizsäcker-Williams approximation [21] according to

$$f_\gamma^e(y) = \frac{\alpha}{2\pi} \left[\frac{1 + (1-y)^2}{y} \cdot \ln \frac{Q_{\text{max}}^2(y)}{Q_{\text{min}}^2(y)} - \frac{2(1-y)}{y} \cdot \left(1 - \frac{Q_{\text{min}}^2(y)}{Q_{\text{max}}^2(y)} \right) \right]. \quad (2.15)$$

In this expression the spectrum of the photon is integrated over the whole Q^2 range. For small scattering angles of the electron, the photon virtuality Q^2 varies in the range between

$$Q_{\text{min}}^2(y) = \frac{y^2 m_e^2}{1-y} \quad (2.16)$$

and

$$Q_{\text{max}}^2(y) = Q_{\text{min}}^2(y) + E_e^2 \cdot (1-y) \cdot \theta_{\text{max}}^2. \quad (2.17)$$

In this equation θ_{max} is the upper limit of the detectable angle of the scattered electron with energy E_e . For the electron tagger at $z = -33.4$ m this angle is $\theta_{\text{max}} = 5$ mrad, corresponding to $Q^2 = 0.01 \text{ GeV}^2$.

With the flux factor from equation (2.15), the ep scattering cross section for heavy quark (Q) production can be calculated now from the photon-proton cross section $\sigma(\gamma p \rightarrow Q\bar{Q}X)$ using

$$\sigma(ep \rightarrow Q\bar{Q}X) = \int f_\gamma^e(y) \cdot \sigma(\gamma p \rightarrow Q\bar{Q}X) dy. \quad (2.18)$$

¹Dokshitzer, Gribov, Lipatov, Altarelli and Parisi

2.3.1 Resolved processes

In the picture of QED the photon can – before interacting with the parton – also fluctuate into a quark-antiquark pair which again can emit gluons.

In *direct photoproduction* the photon from the electron interacts directly with the parton from the proton. Since no particles are emitted from the photon, the total energy emitted from the electron is available for the interaction with the parton.

In *resolved processes*, only a fraction x_γ of the energy emitted by the electron is involved in the interaction with the parton. Two different cases can be distinguished. In the anomalous case the photon fluctuates into a quark-antiquark pair without forming a bound state. In the second case the quark-antiquark pair forms a vector meson, e.g. a ρ , ϕ , or ω meson. This case can be described by a non-pQCD vector dominance model (VDM) [22]. An example of a direct and a

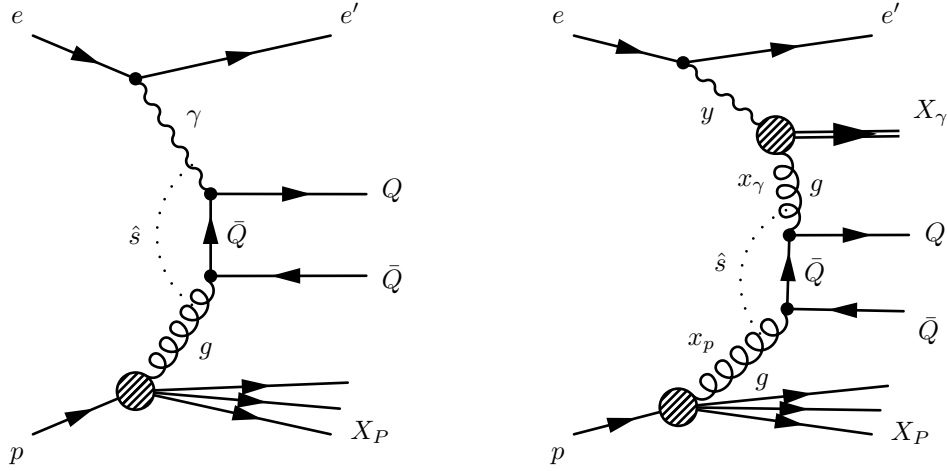


Figure 2.2: Feynman diagram for a direct (left) and a resolved (right) process.

resolved process is shown in figure 2.2.

In analogy to the proton, the hadronic structure of the photon is characterized by a PDF $f_j^\gamma(x_\gamma, \mu_\gamma^2)$ which describes the probability to find a quark j in the photon carrying a momentum fraction x_γ of the photon. For sufficient high transverse momenta of the quark pair the process can be calculated in QED to

$$f_j^\gamma(x_\gamma, \mu_\gamma^2) = e_j^2 \frac{\alpha}{2\pi} \left(x_\gamma^2 + (1-x_\gamma)^2 \right) \cdot \ln \left(\frac{\mu_\gamma^2 (1-x_\gamma)}{m_j^2 x_\gamma} \right). \quad (2.19)$$

This PDF again depends on a factorization scale μ_γ . QCD corrections to this result have been calculated [23] and can be evolved using the DGLAP equations.

Using the PDF of the photon and the photon flux the total cross section for heavy quark (Q) production in ep scattering can be written for photoproduction as

$$\begin{aligned} \sigma^{\gamma p}(ep \rightarrow e' Q \bar{Q} X) = & \sum_{\text{partons } i} \iint dy dx_i f_\gamma^e(y) f_i^p(x_i, \mu_F^2) \hat{\sigma}_{\gamma i}(\hat{s}, \alpha_s(\mu_R), \mu_R, \mu_F, \mu_\gamma) + \\ & \sum_{\text{partons } i, j} \iiint dy dx_\gamma dx_i f_\gamma^e(y) f_j^\gamma(x_\gamma, \mu_\gamma^2) f_i^p(x_i, \mu_F^2) \hat{\sigma}_{ji}(\hat{s}, \alpha_s(\mu_R), \mu_R, \mu_F, \mu_\gamma), \end{aligned} \quad (2.20)$$

where the first term describes direct photoproduction while the second term represents the resolved processes [24]. Equation (2.20) is only valid by the presence of a hard scale $\mu \gtrsim 1$ GeV which can be the mass of a heavy quark or the transverse momentum p_T . The cross section of the hard interaction $\hat{\sigma}_{ij}$ depends on the squared center-of-mass energy of the hard subprocess $\hat{s} = x_i x_\gamma y s$ and the normalization scales. The factorization of the cross section for resolved photoproduction is illustrated in figure 2.3.

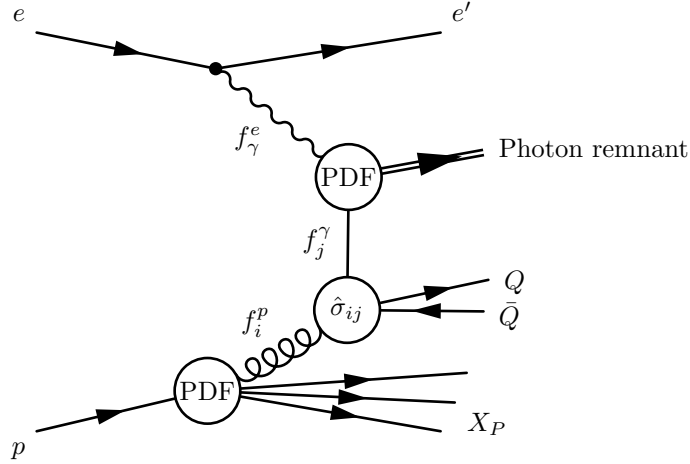


Figure 2.3: Factorization of heavy quark production for resolved photoproduction.

2.4 Production of heavy quarks

From the heavy quarks c , b , t only charm and beauty quarks can be produced at HERA. Since the top quark has a mass of (178.0 ± 4.3) GeV [25], the center of mass energy of the ep collision is not sufficient to create a pair of $t\bar{t}$ quarks. Although the production of a single real top is not excluded in the standard model, this process is highly suppressed.

The main production of heavy quarks at HERA is the boson-gluon fusion (BGF) process as shown in the Feynman diagrams of figure 2.2. In NLO an experimental separation between direct and resolved processes is not possible.

The complete calculation of the cross section of the hard interaction $\hat{\sigma}_{ij}$ in NLO is given in [26] and a review of the theoretical status is given in [24].

Table 2.1 shows the calculated total cross section according to [26]. The values are calculated²

		direct [nb]	resolved [nb]	Sum [nb]
Total cross section	charm	706.9	245.9	952.8
$\sqrt{s} = 318$ GeV	beauty	5.35	1.56	6.91
with kinematical cut	charm	57.6	28.6	86.2
$Q^2 < 0.01$ GeV ² , $0.28 < y < 0.65$	beauty	0.74	0.29	1.03
additional jet cut	charm	0.3760	0.0097	0.3857
$E_T^{\text{Jet}1} > 9$ GeV, $E_T^{\text{Jet}2} > 7$ GeV, $ \eta_{\text{Jet}1,2} < 1$	beauty	0.0540	0.0024	0.0564

Table 2.1: Calculated cross section in NLO for charm and beauty production in ep -scattering using the FMNR program. The cuts for jets are applied on generator level.

using the FMNR program³ in NLO. For this calculation, the proton structure function CTEQ5D [27] and the structure function GRV-HO [28] for the photon are used. The large systematic errors in these calculations are of the order of 30%, dominated by uncertainties in quark masses and scales.

For this calculation the reorganization and factorization scales are set to

$$\mu_r = \mu_f = 2 \cdot \mu = 2 \cdot \sqrt{m_c^2 + p_T^2} \quad (2.21)$$

²Ch. Grab, private communication

³Based on the publication from Frixione, Mangano, Nason and Ridolfi

for charm quarks and the charm mass was varied in the range of 1.3 GeV to 1.7 GeV due to its uncertainty. For beauty quarks the scales are

$$\mu_r = \mu_f = \mu = \sqrt{m_b^2 + p_T^2} \quad (2.22)$$

and the mass m_b for a beauty quark was supposed to be between 4.5 GeV and 5.0 GeV.

2.5 Fragmentation and hadronization

Fragmentation describes the transition of colored quarks of the hard interaction to color neutral hadrons which can be observed in the detector. The colored partons from the hard interaction evolve by radiating off further partons, which then form color-less hadrons. This typically appears as bunches of roughly collinear particles called *jets*. Since the forming of hadrons occurs on large distances where α_s is strongly rising, pQCD fails to describe fragmentation. Therefore, only phenomenological models exist to describe this process.

2.5.1 Lund model of string fragmentation

Due to the confinement, the strong force between two quarks moving apart increases with larger distance. In the Lund model of string fragmentation [29], the energy of a color flux tube (string) between these two quarks is modelled by

$$E(r) = \kappa \cdot r \quad (2.23)$$

with the string constant $\kappa \approx 1 \text{ GeV/fm}$. At distances of $\sim 1 \text{ fm}$ it is energetically favorable if the string breaks up and two color singlets are formed. This procedure is repeated iteratively until the energy of individual strings between partons is too small for further separation.

In the Lund Model also gluons are included. They are supposed to produce kinks on the strings.

2.5.2 Peterson fragmentation

The Peterson fragmentation [30] is an independent fragmentation model in the sense that each parton is allowed to fragment independently of the other. It is mainly used to describe the hadronization of a heavy quark Q . In this model a new hadron $H = (Q\bar{q})$ is formed by attaching a light anti-quark of a created $q\bar{q}$ pair from the vacuum. The probability that a momentum fraction z is transferred from the initial quark Q to the final hadron is parameterized as

$$D_Q^H(z) \propto \frac{1}{z} \left(1 - \frac{1}{z} - \frac{\epsilon_Q}{1-z} \right)^{-2}. \quad (2.24)$$

The Peterson parameter ϵ_Q in equation (2.24) describes the hardness of the fragmentation and is estimated by $\epsilon_Q = (m_q/m_Q)^2$. Due to the difficulty to define quark masses, the Peterson parameter is determined experimentally.

2.6 Monte Carlo Event Generator

The MC event generator PYTHIA 6.1 [31] was used in this analysis. This generator is able to generate various processes using leading order pQCD with additional QCD radiation. Furthermore, it can be operated in an *all-inclusive* mode for photoproduction to generate all contributing direct or resolved processes simultaneously. For the calculation of the hard interaction all quark flavours – also heavy quarks – are treated as massless partons in this mode. Beauty events are selected by requiring at least one beauty quark in the list of outgoing hard partons while charm events are selected with at least one charm and no beauty quark.

The MC events were generated using the CTEQ 5L [27] PDF of the proton with $\Lambda_{\text{QCD}} = 192 \text{ MeV}$ and the GRV-G LO [28] PDF of the photon with $\Lambda_{\text{QCD}} = 200 \text{ MeV}$. Both PDFs are based on a leading order calculation in order to have a consistent combination with the PYTHIA generator.

In PYTHIA, the fragmentation of heavy quarks into hadrons is modelled by the independent Peterson fragmentation. For this fragmentation the Peterson parameters

ϵ_c	0.058
ϵ_b	0.0069

from [32] are used. The hadronization of light quarks and gluons is described by the LUND string fragmentation.

The MC event generator is also able to describe multiple interactions between the proton and the resolved photon. In PYTHIA, multiple interactions are dealt by adding additional interactions between spectator partons within the same event. Besides this, also initial state and finale state radiation effects are modelled. The former contributions are based on phenomenological assumptions whereas the latter are based on approximations from pQCD.

The MC sets used for this analysis consist of an overall inclusive set with about the same luminosity as in data and a high luminosity set for charm and beauty as listed in table 2.2. For all

Quark flavour in hard interaction	Luminosity	Events	Generator	H1SIM version
All flavours ($uds / c / b$)	56.94 pb^{-1}	7'999'916	PYTHIA 6.1	Row 21
Charm (c)	112.11 pb^{-1}	2'999'970	PYTHIA 6.1	Row 21
Beauty (b)	458.85 pb^{-1}	599'940	PYTHIA 6.1	Row 21

Table 2.2: Sets of MC events used in this analysis.

sets the kinematical cuts $Q^2 < 0.1 \text{ GeV}^2$ and $0.25 < y < 0.7$ are applied. Two jets on generator level with $E_T^{\text{Jet}1} > 4 \text{ GeV}$, $E_T^{\text{Jet}2} > 3 \text{ GeV}$, $|\eta_{\text{Jet}1,2}| < 2.5$ are also requested. More details on the jet cut is given in section 4.3.2.

For the hadronization part of the MC event generator, the mass and lifetime for heavy hadrons are modified according to table 2.3. The numbers for the fragmentation fraction are from [33] for charm, respectively [34] for beauty. Lifetime and mass numbers are from [7]. Additionally, the

c -Hadron	Fraction	Mass [MeV]	$c\tau$ [μm]	b -Hadron	Fraction	Mass [GeV]	$c\tau$ [μm]
D^+ cd	23.2%	1869.4	311.8	B^0 db	39.7%	5.2790	460
D^0 cd	54.9%	1864.5	123.0	B^+ ub	39.7%	5.2794	501
D_s^+ $c\bar{s}$	10.1%	1969.3	147.0	B_s^0 sb	10.7%	5.3696	438
Λ_c^+ duc	7.6%	2284.9	59.9	B_c^+ cb		6.4	138
Ξ_c^+ usc		2466.3	132	Λ_b^0 udb		5.624	368
Ξ_c^0 dsc		2471.8	33.6	Ξ_b^0 usb			420
Ω_c^0 ssc		2697.5	21	Ξ_b^+ dsb			420

Table 2.3: Lifetime, mass and fragmentation fraction of charm and beauty hadrons. Unspecified fragmentation fractions are small and still unmeasured.

charged track multiplicity for beauty hadrons are adapted to the multiplicities measured at LEP [34].

Finally a smaller MC set without jet restriction with 100'000 events was used to study the effect of different jet cuts.

Chapter 3

Analysis Method

In this chapter the analysis method is presented. After a general motivation, it starts with the description of reconstructing the kinematics of an event. Then, the algorithm for finding jets is outlined since the selection of events is primarily based on jet topologies. Finally, the algorithm for finding secondary vertices is described in detail.

3.1 General introduction to this analysis

There are several methods to measure the production of events with heavy quarks.

Exclusive method In this method specific decay channels of heavy quarks are reconstructed. Although the fragmentation of heavy quarks offers a wide spectrum of decay channels only few of them are accessible. Several factors are restricting the number of reconstructable decay channels such as limited detector acceptance or resolution. Besides this, decay channels with a high decay multiplicity or neutral decay products are inappropriate. If there is a neutral or undetected particle in the decay spectrum of a hadron then the kinematics of this hadron cannot be reconstructed with sufficient precision and it is not possible to discriminate the signal from the background.

Often, most restricting is the small branching ratio in combination with the track efficiency of a specific decay channel. For example, charmed jets are often tagged by the decay of a D^{*+} since the π^+ from the D^{*+} decay has a small phase space and therefore offers a signal with good resolution. This allows a successful fight against the combinatorial background. But the overall branching ratio for this decay chain is only 0.6%:

$$c \xrightarrow{23.5\%} D^{*+} \xrightarrow{67.7\%} D^0 \pi^+ \xrightarrow{3.8\%} K^- \pi^+ \pi^+$$

In a recent analysis several decay channels for charmed hadrons are measured and compared [35].

The situation looks even worse for beauty decays. In most of the cases a beauty hadron decays into a charmed hadron. To reconstruct a beauty decay also the charmed hadron must be reconstructed. Consequently there is a large number of possible decay channels which results in a small event yield per decay channel.

Inclusive method In contrast to the exclusive method, a dedicated decay channel is not reconstructed with an inclusive method. The method is based on measurable variables which have different distributions for different quark flavours. Typical variables used for inclusive measurements are the momentum of tracks relative to the jet axis for b decays or variables describing the separation of a secondary vertex from the primary interaction point. The shape of kinematical variables of each quark flavour is generated by MC and can be used to extract the flavour fraction from data.

The advantage of the inclusive method is that many channels are considered at the same time and thus small branching ratios are irrelevant. On the other hand hard cuts often have to

be applied to get distinguishable shapes. This again reduces the statistical gain of an inclusive method.

In the present analysis the approach of an inclusive method was chosen. An additional advantage of an inclusive method is that charm and beauty fractions are measured at the same time.

3.1.1 Lifetime of hadrons with heavy quarks

The charm or beauty quark decays into a light quark by emitting a virtual W^\pm boson. The typical time scale of weak decays is of the order 10^{-12} s which is much longer than in strong decays. This leads to resolvable mean lifetimes for hadrons with heavy quarks. The decay width of a heavy hadron is

$$\Gamma = 1/\tau \propto m_Q^5 \cdot |V_{Qq}|^2. \quad (3.1)$$

Even if the mass of a b quark is three times larger than for the c quark, the lifetime of a beauty hadron is longer due to the small value V_{cb} of the Cabibbo-Kobayashi-Maskawa matrix. For beauty decays the square of the matrix element is $|V_{cb}|^2 \approx 0.0017$ and for charm decays $|V_{cs}|^2 \approx 0.992$. It is remarkable that the lifetime of a D^+ is about a factor 2.5 longer than for the other charmed hadrons. This can be explained by an interference effect in the $D^+ \rightarrow \bar{K}^0 \pi^+$ decay [36].

The observable decay length l of a hadron with momentum p and mass m is related to the lifetime τ by

$$l = \beta \cdot \gamma \cdot c \cdot \tau = \frac{p}{m} \cdot c \cdot \tau, \quad (3.2)$$

where $\frac{p}{m} = \beta \cdot \gamma$ denotes the boost of the particle. For HERA kinematics, the difference in decay length of charm and beauty hadrons is smaller than expected from lifetime since charm hadrons are produced with a higher boost than beauty hadrons. As shown in figure 3.1, the decay lengths in the laboratory system for beauty and charm hadrons are very similar distributions.

The remarkable property of charm or beauty hadrons is that their finite decay length is in the order of 0.1 mm. "Up" and "down" quarks fragment into hadrons with a prompt decay or a decay length of several meters (π^\pm , n). In case of hadrons with strangeness the decay length of several cm (K_S^0 , Λ , Ξ^\pm , Ω^\pm) is still two orders of magnitude longer than for heavy quarks.

This feature can be used to tag heavy quarks by an explicit reconstruction of a secondary vertex from the decaying hadron. The separation of the secondary vertex from the primary has to be searched in the range from several mm down to the scale of the track resolution. Due to the exponential form of the decay law the method is limited by the lower bound of the vertex separation.

A precise determination of tracks is indispensable for finding a secondary vertex in a close neighbourhood of the primary vertex. Only tracks measured by the CST attain the required precision. The errors of the track parameters are the crucial values when determining the separation from the primary to the secondary vertex. Instead of the decay length l it is more appropriate to use the *decay length significance* S_l defined as the decay length l divided by its error σ_l to describe the separation.

3.1.2 Analysis method

The finite lifetime of heavy quarks motivates the method for this analysis which includes the following steps:

- From all positron-proton events collected by the H1 detector during the years 1999 and 2000, all tagged photoproduction events are selected. The explicit detection of the scattered positron ensures a clean data sample.
- In this data sample, jets are reconstructed and a sufficient hard scale for these jets is required. It is supposed that the jets originate from the primary hard interaction and that most of the hadrons from the hadronization process are collected by these jets.

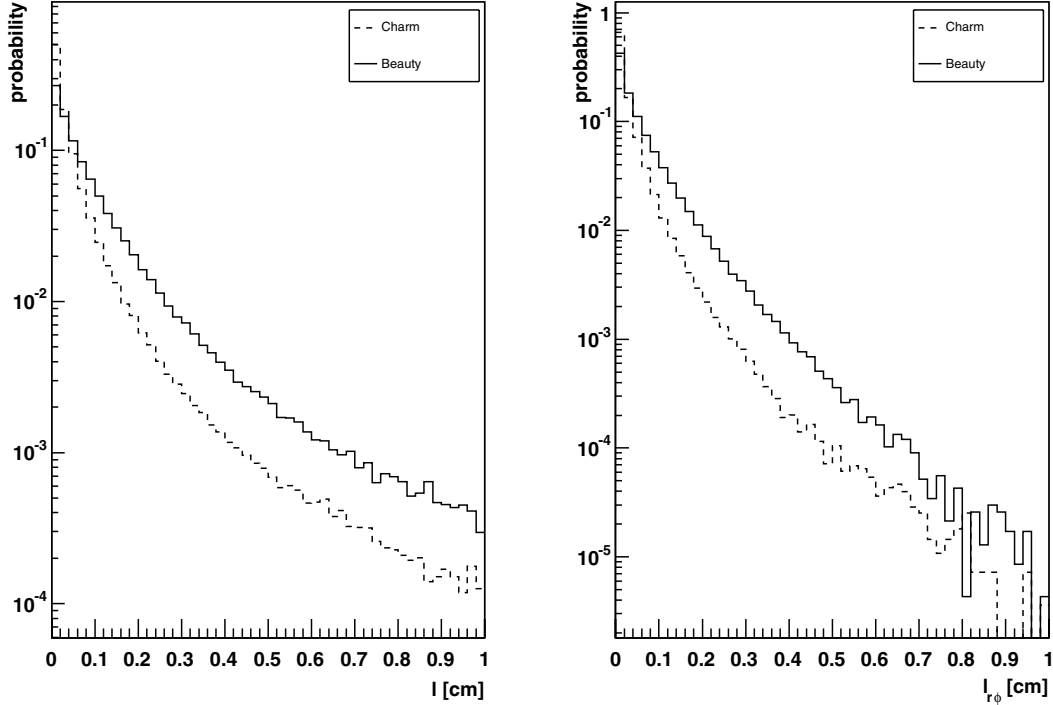


Figure 3.1: Decay length distribution for charm and beauty hadrons in the kinematical region used for this analysis. The 3-dimensional decay length (left) and the projection of the decay length to the $r\phi$ -plane (right) are shown. The distributions are calculated using the PYTHIA MC event generator.

- A secondary vertex is searched within the two most energetic jets by an explicit reconstruction using all tracks from the jet.
- The fraction for charm and beauty is extracted from the distribution of the decay length significance.

The fitted flavour fraction of data is finally used to calculate the cross section for charm and beauty.

3.2 Kinematical variables

The basic objects measured by the H1 detector are tracks reconstructed from the tracking chambers and energy clusters measured by the calorimeter. To reconstruct the hadronic energy distribution in the detector the cluster information from the calorimeter must be used. The calorimeter covers a large angular range and is able to detect hadrons in their final state.

However, the energy measurement of the calorimeter is incomplete due to low-energy particles. For example a charged pion with a momentum of 500 MeV has only a probability of 50% to deposit an energy above the noise threshold and thus be recorded. In addition, tracks with a transverse momentum below 200 MeV even do not reach the calorimeter due to their strong bending in the magnetic field.

The energy loss can be partially compensated by considering also tracks in addition to the calorimeter clusters. When combining tracks and clusters special care must be taken to avoid

double counting of energy. The *hadronic final state* (HFS) software package was used to cope with this problem. This software package handles also a lot of technical details like calibration and noise reduction of the calorimeter.

Tracks are combined with calibrated and noise-suppressed clusters. If the track energy is greater than the energy within an extrapolated cylinder on the calorimeter front all clusters in the cylinder are masked. If the track energy is smaller, those clusters with the smallest distance of closest approach to the extrapolated track are masked in such a way that the total energy of the masked clusters is approximately equal to the track energy. Since the relative error of the momentum measurement in the tracking chamber is proportional to the particle momentum ($\sigma_p/p \propto p$), there is an upper cut-off for the transverse momentum p_T of a track. Tracks having $p_T > 2 \text{ GeV}$ are rescaled to have $p_T = 2 \text{ GeV}$.

The resulting combined HFS objects are required to reconstruct kinematical variables and are also used as input to the jet algorithm.

In case of tagged photoproduction the reconstruction of the event kinematics is rather simple since the scattered electron is detected with good energy resolution ($\sigma_{E_{e'}}/E_{e'} = 20\%/\sqrt{E_{e'}/\text{GeV}}$) and small probability of misidentification.

By neglecting the electron mass, the negative momentum transfer squared Q^2 can be expressed by the angle of the scattered electron $\theta_{e'}$

$$Q^2 = 4 E_e E_{e'} \cos^2 \left(\frac{\theta_{e'}}{2} \right) \quad (3.3)$$

and with equation (2.6) the inelasticity y becomes

$$y = y_{\text{ET}} = 1 - \frac{E_{e'}}{E_e} \sin^2 \left(\frac{\theta_{e'}}{2} \right). \quad (3.4)$$

Using equations (3.3) and (3.4) to determine the event kinematics is often called *electron-method* since it is based on a precise measurement of the electron. In case of photoproduction with ($\theta \approx 180^\circ$) equation (3.4) simplifies to

$$y = \frac{E_e - E_{e'}}{E_e}. \quad (3.5)$$

If the scattered electron of a photoproduction event is detected by the electron tagger, Q^2 cannot be measured using equation (3.3) since the trajectory of the scattered electron is influenced by the beam optics. The correlation of the scattered angle $\theta_{e'}$ and the measured impact of the electron in the electron tagger depends on many factors and is not simulated. In addition, the z -position of the vertex has a major influence on the trajectory of the electron. Events measured by the electron tagger have a squared momentum transfer of

$$3 \cdot 10^{-8} \text{ GeV}^2 < Q^2 < 0.01 \text{ GeV}^2. \quad (3.6)$$

The lower limit is determined from equation (2.16) and the upper limit is calculated with the maximal scattering angle of the electron which is deduced from the beam optics.

The event kinematics can also be reconstructed from the hadronic final state. This method according to *Jacquet-Blondel* [37] is used if the electron is poorly or not detected. The method must be applied in charged current events with no outgoing electron. Using the transverse momentum $p_{T,i}$ of each HFS object i , the negative momentum transfer is now

$$Q_{\text{JB}}^2 = \frac{1}{1 - y_{\text{JB}}} \sum_i p_{T,i}^2 \quad (3.7)$$

with

$$y_{\text{JB}} = \frac{1}{2 E_e} \sum_i (E_i - p_{z,i}). \quad (3.8)$$

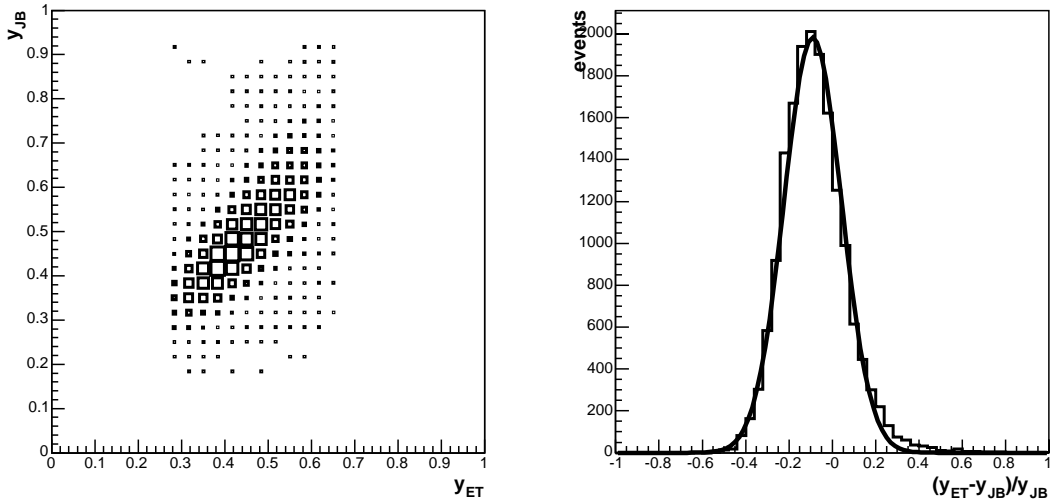


Figure 3.2: Correlation of y_{ET} and y_{JB} (left) and the relative difference (right).

In case of tagged photoproduction y_{ET} and y_{JB} are determined independently and thus can be used as a cross-check. The correlation and relative difference between y_{ET} and y_{JB} is shown in figure 3.2. The resolution of y determined with the Jacquet-Blondel method is not as good as the y reconstructed from the electron tagger. A reason for this is that y_{JB} is calculated from the sum of all measured energies within the detector and therefore is sensitive to energy calibrations.

3.3 Jet reconstruction

The reconstruction of jet variables gives access to the underlying dynamics of the hard interaction since the reconstructed final state is related to the kinematics of the outgoing partons from the hard interaction. Even if a qualitative definition of jets is rather intuitive – a large amount of hadronic energy in a small solid angle – a quantitative definition must be applied to make it comparable with theory and other experiments. For this, a distance measure in phase space and a recombination rule for detected energies is needed. This task is performed by a jet algorithm.

A jet algorithm must satisfy several criteria. The most important are to be

- insensitive to soft and collinear radiation, i.e. infrared and collinear safe,
- applicable on parton, hadron and detector level.

Actually there are more than two different classes of jet algorithms in use. Cone-type algorithms based on the early ideas of Serman-Weinberg [38] and cluster algorithms originally introduced by the JADE collaboration [39].

In this analysis the longitudinal invariant k_T cluster algorithm is applied which has become standard in jet analyses at HERA [40] and is also implemented for the H1 environment. The input for the algorithms is based in general on HFS objects but it can also operate on any objects described by a set of kinematic variables $(\eta_i, \phi_i, p_{T,i})$. For each jet found, the algorithm provides at least the direction of the jet axis (η_{jet}, ϕ_{jet}) and the corresponding transverse jet energy E_T .

3.3.1 The longitudinal invariant k_T jet algorithm

Instead of globally finding the jet axis, this algorithm defines jets by successively recombining objects nearby in phase space into jets. The longitudinal invariant k_T algorithm [41, 42] is based

on the k_T algorithm [43] which uses the relative transverse momentum of two particles as a separation measure. The modification of the original k_T algorithm incorporates the longitudinally invariant variables (E_T , η and ϕ) which are necessary in the boosted hadron collider environment.

The longitudinal invariant k_T jet algorithm starts with a list of massless¹ *protojets* $i = 1, \dots, N$ which can be partons, hadrons or HFS objects. The algorithm comprises the following four steps which are iteratively repeated:

1. For each protojet a separation to the beam axis

$$d_i = E_{T,i}^2 \quad (3.9)$$

and for each pair of protojets a separation to each other

$$d_{ij} = \min(d_i, d_j) \frac{(\eta_i - \eta_j)^2 + (\phi_i - \phi_j)^2}{R^2} = \min(d_i, d_j) \frac{\Delta R_{ij}^2}{R^2} \quad (3.10)$$

is defined. R_{ij} is the distance between two protojets i and j in the η - ϕ plane. The parameter R is an adjustable parameter of the algorithm which plays the role of a jet radius in this plane. In this analysis the parameter is set to $R = 1$ which is also the theoretically preferred value [41].

2. The smallest distance d_{\min} of a single or a pair of protojets is searched

$$d_{\min} = \min(d_i, d_{ij}). \quad (3.11)$$

3. If d_{\min} is a pair distance d_{ij} then the two protojets i and j are merged to form a new protojet k and are removed from the list according to

$$E_{T,k} = E_{T,i} + E_{T,j} \quad (3.12)$$

$$\phi_k = w_{ij}^i \cdot \phi_i + w_{ij}^j \cdot \phi_j \quad (3.13)$$

$$\eta_k = w_{ij}^i \cdot \eta_i + w_{ij}^j \cdot \eta_j. \quad (3.14)$$

The weight factor w_{ij}^l is $w_{ij}^l = \frac{E_{T,l}}{E_{T,i} + E_{T,j}}$ in the p_T weighted scheme or $w_{ij}^l = \frac{E_{T,l}^2}{E_{T,i}^2 + E_{T,j}^2}$ in the p_T^2 weighted scheme. In this analysis the p_T weighted scheme was used. In a simpler E recombination scheme the momenta are simply added $\vec{p}_k = \vec{p}_i + \vec{p}_j$.

4. If d_{\min} is a single distance d_i then the appropriate protojet cannot be merged anymore. The protojet is removed from the list of protojets and is added to the list of jets.

The procedure is repeated until the list of protojets is empty and all protojets have been assigned to the list of jets with increasing values of $E_{T,i}^2 (= d_i)$. Since in each iteration step one protojet is merged or removed, the number of iterations is equal to the number of initial protojets.

Finally, an E_T cut is imposed on the list of jets which sets the scale to distinguish hard and soft processes. As shown in [44], the jet cuts should be chosen asymmetric. This means that the transverse energy cut $E_T^{(1)\text{cut}}$ for the highest E_T jet should be greater than for the second jet $E_T^{(2)\text{cut}} < E_T^{(1)\text{cut}}$. If a symmetric cut is applied $E_T^{(1)\text{cut}} = E_T^{(2)\text{cut}}$ the cross section becomes sensitive to infrared divergencies in theoretical calculations.

3.3.2 Resolved contribution and jets

The momentum fraction x_γ can be reconstructed from the kinematics of jets. Under the assumption that the product of the hard process is collected in jets, the fraction x_γ can be expressed

¹Hence $E_{T,i} = |\vec{p}_{T,i}|$

as

$$\begin{aligned}
 x_\gamma &= \frac{[E - p_z]_{\text{Hard}}}{[E - p_z]_{\text{All}}} = \frac{\sum_{j \in \text{Jet}} E_j - p_{z,j}}{\sum_{i \in \text{HFS}} E_i - p_{z,i}} = \frac{\sum_{j \in \text{Jet}} \frac{E_{T,j}}{\sin(\theta_j)} - \frac{E_{T,j}}{\tan(\theta_j)}}{2 E_e y} \\
 &= \frac{\sum_{j \in \text{Jet}} E_{T,j} \tan\left(\frac{\theta_j}{2}\right)}{2 E_e y} = \frac{1}{2 E_e y} \sum_{j \in \text{Jet}} E_{T,j} e^{-\eta_j}.
 \end{aligned} \tag{3.15}$$

To obtain this result, equation (3.8) was used. In a similar way the momentum fraction on the proton side x_p can be reconstructed

$$x_p = \frac{1}{2 E_p} \sum_i E_{T,i} e^{-\eta_i}. \tag{3.16}$$

The correlation of generated and reconstructed x_γ is shown in figure 3.3. The reconstructed x_γ^{rec}

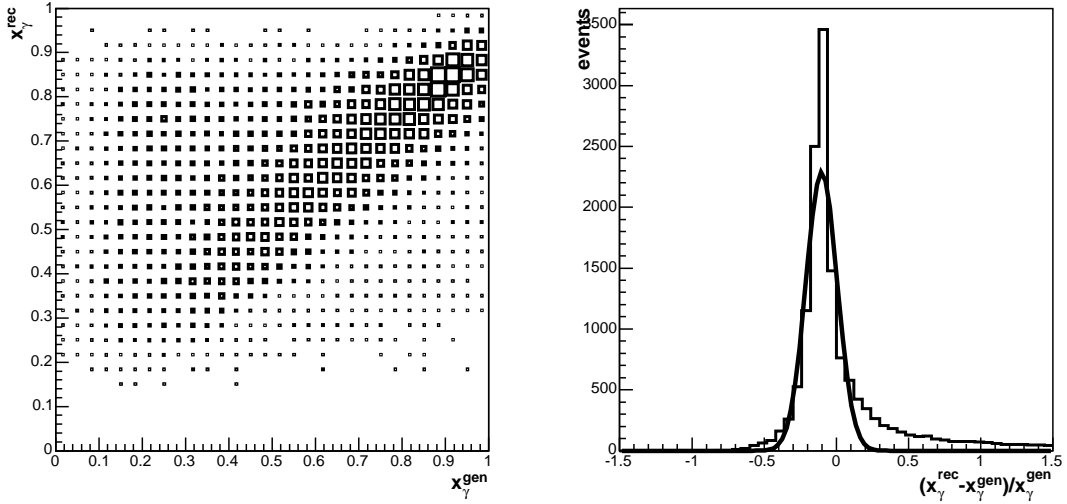


Figure 3.3: Correlation and the relative difference of generated x_γ^{gen} and reconstructed x_γ^{rec} for MC events.

is on average about 10% lower than the generated x_γ^{gen} since the energy from the hard interaction is not completely collected by the jet algorithm. On the other hand the reconstructed x_γ^{rec} value is smeared out to larger values especially for small x_γ . The reason for this is that additional energy from soft underlying events is collected by the jet algorithm.

The contribution of resolved processes is strongly suppressed by the requirement of hard jets as can be seen in figure 3.4 for two-jet events. Due to the smaller transverse momentum of resolved processes, they can additionally be suppressed by requiring the jets in the central detector region ($|\eta_{\text{Jet}} < 1.5|$).

In addition, the fraction of events with heavy flavours is increased by the requirement of hard jets in the central detector region which enhance the boson-gluon fusion versus soft physics. For the jet cuts used in this analysis such as $E_T > 9(7)$ GeV for the leading (second) jet and $|\eta_{\text{jet}}| < 1$, the contributions of heavy quarks from direct and resolved processes are of the same order as can be seen in figure 3.5.

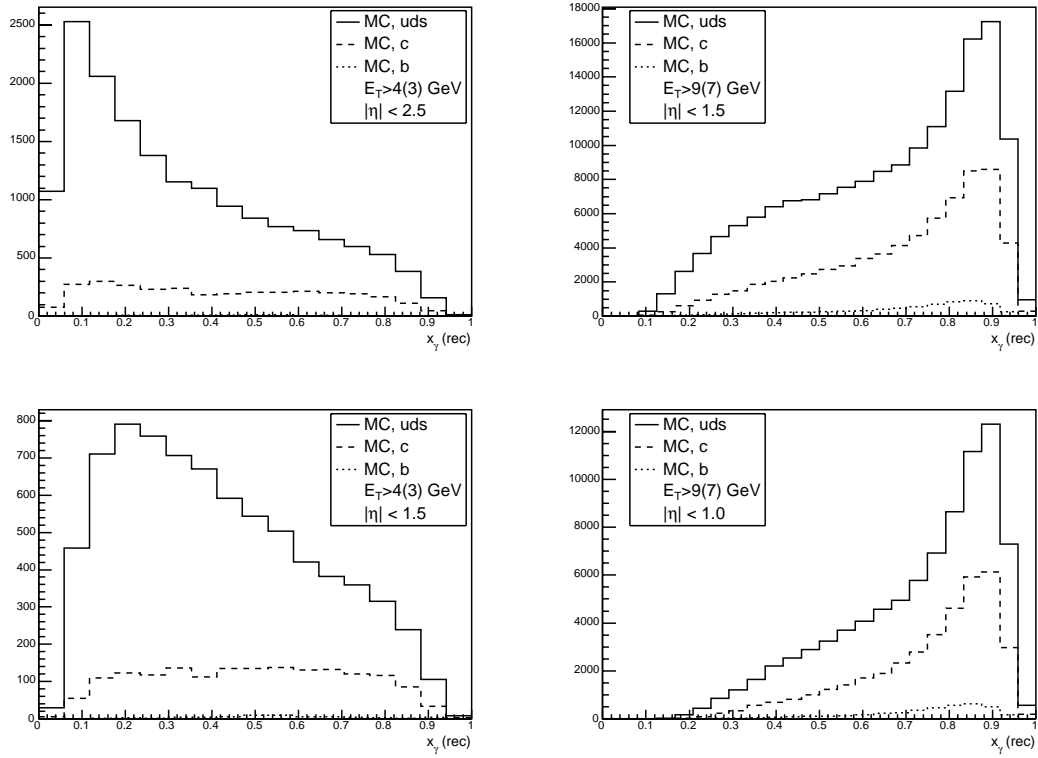


Figure 3.4: Reconstructed x_γ distribution of two-jet MC events for different cuts on transverse energy E_T of the leading (second) jet and on jet rapidity η . Stronger jet cuts enrich direct processes ($x_\gamma \approx 1$) and also the fraction of contributions from events with heavy flavour. The cuts applied to produce the lower right distribution correspond to the cuts used in this analysis. Two different MC sets are used to produce these distributions.

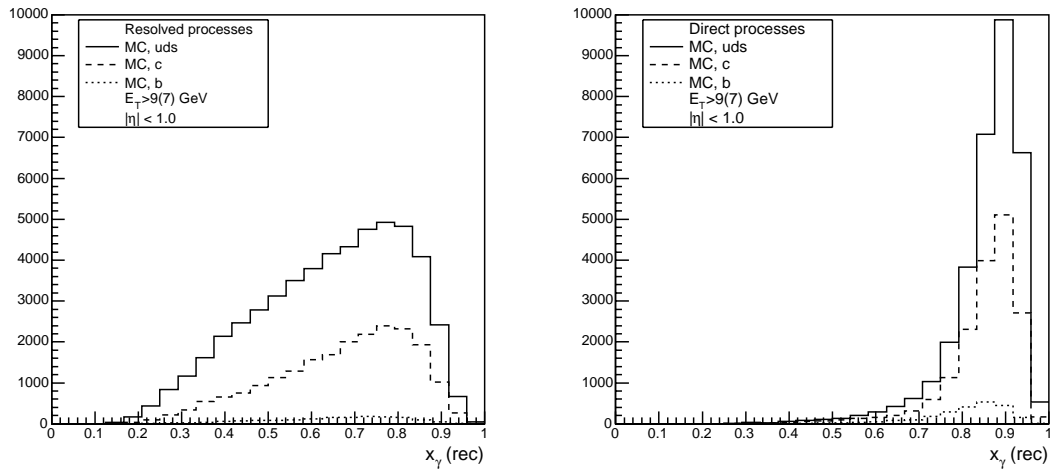


Figure 3.5: Reconstructed x_γ of MC events for resolved (left) and direct (right) processes. The events are selected with the same jet requirement as used in this analysis.

3.4 Secondary vertex finder

As shown in section 3.1 heavy quarks can be identified by secondary vertices with a separation to the primary vertex in a certain range based on S_l , the separation significance. When searching for secondary vertices also the track multiplicity of this vertex has to be considered. For charmed hadrons, the average multiplicity of tracks which are taggable with the CST is clearly below 2, whereas the multiplicity for beauty hadrons is higher as shown in figure 3.6.

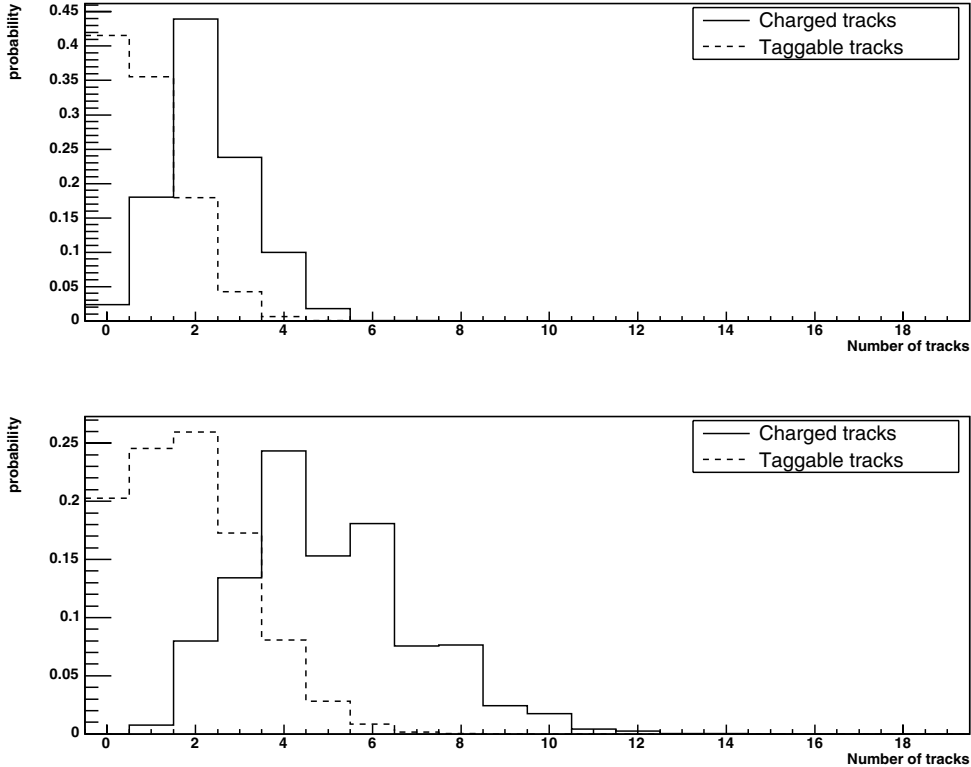


Figure 3.6: Charged track multiplicity for charm (*top*) and beauty (*bottom*) hadron decays in MC events. The solid line shows the distribution for all charged tracks while the dotted line shows only tracks detectable by the CST ($p_T > 500$ MeV, $|\eta| < 1.5$).

There exist several methods to find secondary vertices. Methods with an explicit vertex reconstruction try to fit 2 or more tracks to a common secondary vertex. Other techniques like the multi-impactparameter [45] method do not apply an explicit reconstruction of a vertex and are based on tracks that are not compatible with a primary vertex.

In this analysis the approach of a variable multiplicity vertex fitter was selected. With this method the vertex is constructed explicitly but with variable track multiplicities. The track multiplicity of a secondary vertex is considered as an additional degree of freedom and is determined during the fit procedure. The use of a variable number of tracks for fitting a secondary vertex is accommodated to the different track multiplicity of charm and beauty hadron decays. The assignment of tracks to a secondary vertex is based on a technique known as deterministic annealing.

3.4.1 Deterministic annealing

Deterministic annealing (DA) is an optimization technique which has an analogy in statistical mechanics as the name implies. In general, an optimization algorithm must be able to find the

minimum of a cost function for a given problem. Many of the standard optimization methods have the difficulty that they are attracted by a local minimum instead of the global minimum of the cost function. The annealing process in physical chemistry motivated the use of similar techniques to avoid local minima. There, a system is brought to the lowest energy state by slowly decreasing the temperature.

The Metropolis algorithm implements such a model with a cost function parameterized by the temperature. In this iterative algorithm a random move of the current state is performed and is randomly accepted with a probability depending on the cost function of this new state. During these iterations the temperature is lowered according to an annealing scheme. It is proven that a global minimum can always be obtained if the temperature is lowered with $T \propto 1/\log n$ in the n th iteration step [46]. However such a temperature schedule is not realistic for most applications.

In the DA method, the advantage of the Metropolis algorithm is combined with a standard optimization algorithm. The DA algorithm is deterministic which means that a new state is found by an optimization algorithm instead of randomly generated states as in the Metropolis algorithm. On the other hand the algorithm is still an annealing method with the aim to find the global minima.

Besides finding the global minima, the DA approach has also the advantage that it can optimize cost functions with an almost everywhere vanishing gradient. Furthermore, the algorithm is applicable to various problems. A detailed review on DA can be found in [47].

3.4.2 Adaptive vertex fitter

The fitting procedure is performed in the $r\phi$ -plane by ignoring the z information of tracks because the CJC resolution in $r\phi$ is an order of magnitude better than in z which complicates the linking of CJC track segments with a hit on the z -side of the CST. In addition, the signal over noise on the z -side of the CST is worse than on the r side. As a consequence the z -side is occupied by more noise hits. Linking a noise hit to a track segment from the CJC leads to tails in the resolution.

For fitting tracks to a vertex, a two-dimensional unconstrained (2du) fitter is used [48]. The fitter is slightly modified to handle weighted tracks.

The important parameters used to describe secondary vertices are shown in figure 3.7. Similar

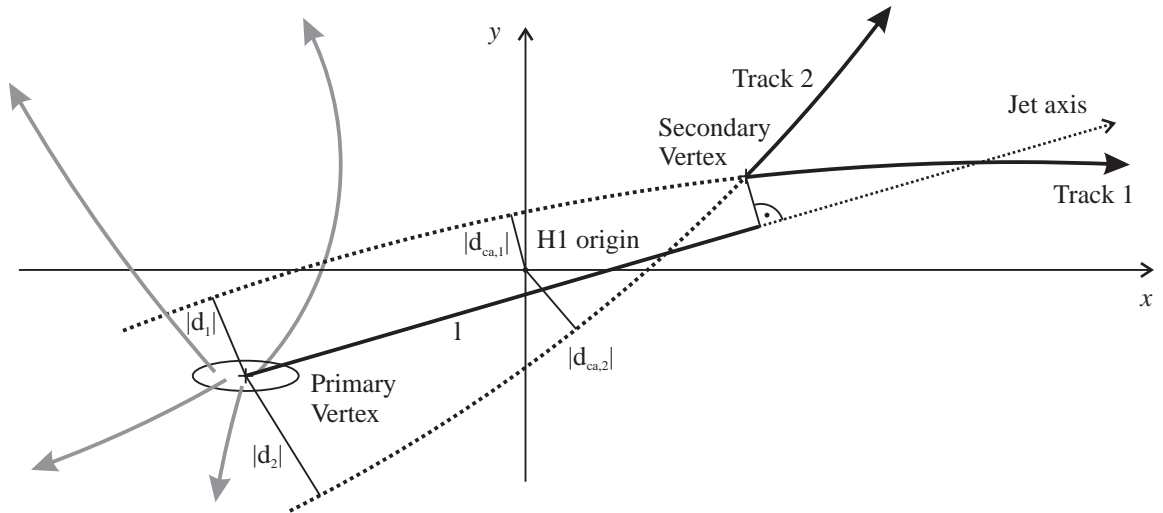
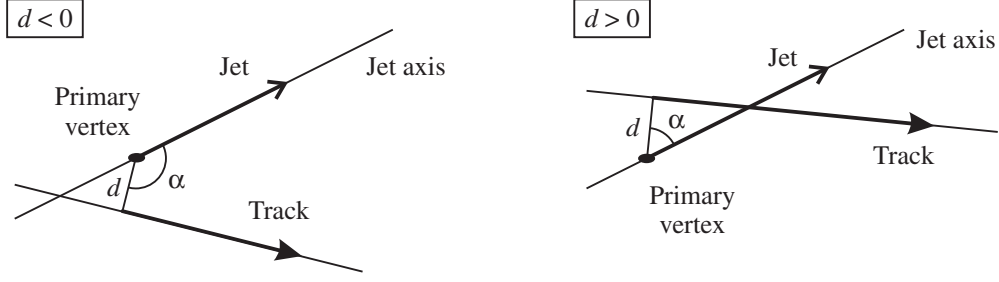


Figure 3.7: Definition of vertexing parameters.

to the d_{ca} , the *impact parameter* d of a track describes the closest approach of a track in the $r\phi$ -plane but now with respect to the primary vertex. The sign of the impact parameter is defined in relation to the jet axis. If the angle α between the jet axis and the impact parameter is smaller than 90° the sign is positive otherwise the sign is negative (see also figure 3.8).

Figure 3.8: Definition of the sign of the impact parameter d .

The other important variable is the *decay length* l which is the projection of the vertex separation vector ($\vec{v}_{\text{secondary}} - \vec{v}_{\text{primary}}$) to the jet axis in the r - ϕ plane. The sign of the decay length is positive if the decay length points in the jet direction and is negative in the other case.

Because the error of the reconstructed decay length, σ_l , has a large variation it is more appropriate to use the *decay length significance*

$$S_l = \frac{l}{\sigma_l}. \quad (3.17)$$

to quantify the separation of the primary vertex.

A showcase event with a secondary vertex found by the adaptive vertex fitter is shown in figure 3.9. In this example the track multiplicity of the secondary vertex is four and the invariant mass of these tracks with a m_π hypothesis is larger than 3 GeV. Thus the decaying particle is very likely a decaying beauty hadron.

The algorithm for an adaptive vertex fitting

The main difference of an adaptive vertex fitter compared to a standard fitter is the soft assignment of tracks to the primary and secondary vertex. A track can contribute to both vertices with a certain weight. Only well measured tracks within a cone around the jet axis are selected for a secondary vertex fit.

For each well measured track i in a jet, a weight in relation to vertex j is defined as

$$w_{ij}(T) = \frac{e^{-\frac{d_{ij}^2}{2T}}}{\sum_{j'} e^{-\frac{d_{ij'}^2}{2T}} + e^{-\frac{\mu^2}{2T}}}. \quad (3.18)$$

$d_{ij} = d/\sigma_d$ is the significance of the impact parameter of track i with respect to vertex j and the sum j' runs over all vertices, in our case over the primary and the secondary vertex. μ is an upper cut-off parameter because w_{ij} goes to 0 for d_{ij} greater than μ [49]. In this analysis the cut-off parameter is set to $\mu = 2$.

It is obvious that weights are positive and smaller than 1. Weights are small if the corresponding track i is incompatible with the vertex j . On the other hand $w_{ij}(T)$ is approximately 1 for an unambiguous assignment to a vertex. The sum $\sum_j w_{ij}(T)$ is approximately 1 if the track i is compatible with one of the vertices. If the track i is not assigned to any vertex, the sum $\sum_j w_{ij}(T)$ is approximately 0. The weights w_{ij} depend on a parameter T which can be identified in terms of DA as the temperature. During the iterative fitting process the temperature is steadily reduced. The fitting algorithm includes the following steps:

1. The algorithm starts with all well measured tracks ($\eta_{\text{track}}, \phi_{\text{track}}$) in a cone around the jet axis ($\eta_{\text{jet}}, \phi_{\text{jet}}$) which fulfill

$$R = \sqrt{(\phi_{\text{jet}} - \phi_{\text{track}})^2 + (\eta_{\text{jet}} - \eta_{\text{track}})^2} \leq 1. \quad (3.19)$$

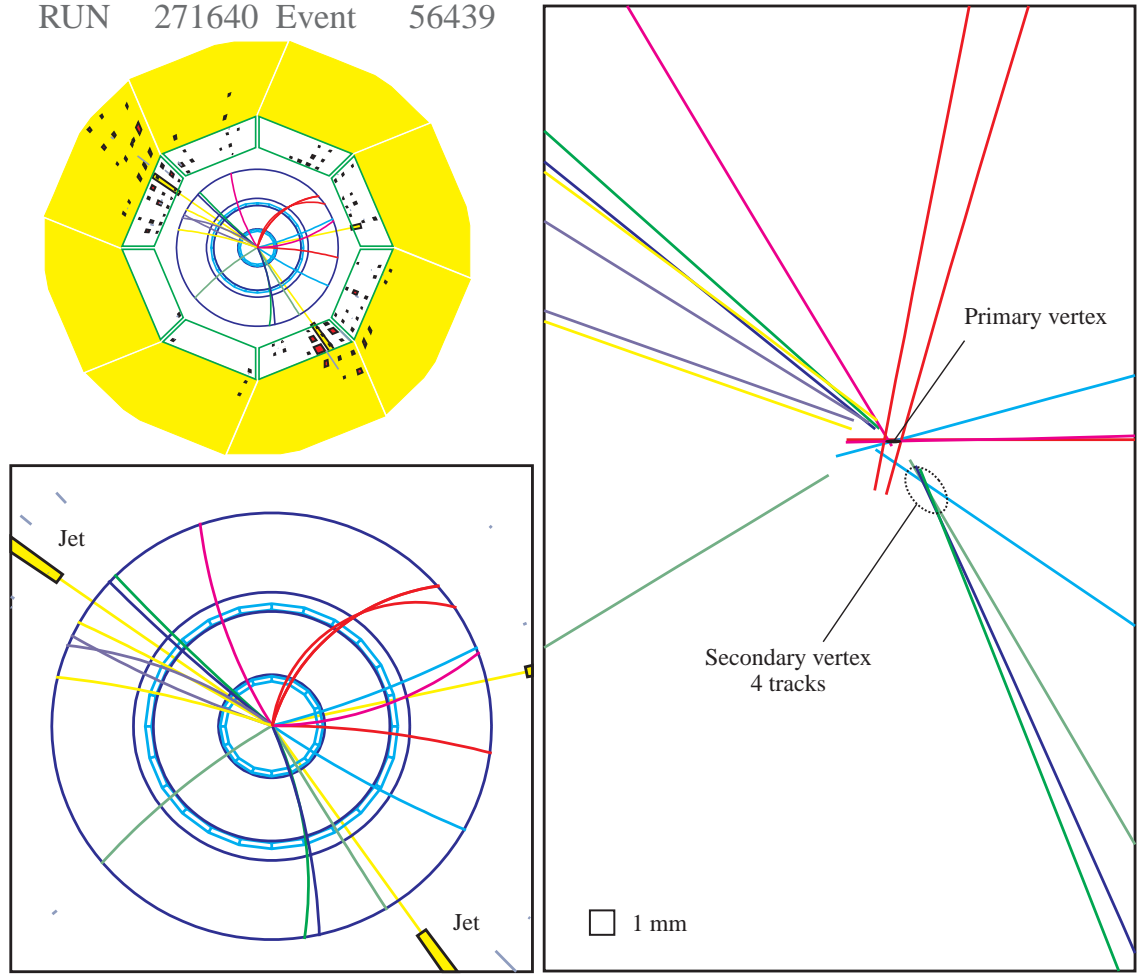


Figure 3.9: Example of an event with a secondary vertex in the radial view (r - ϕ plane) of the H1 detector. The calorimeter is shown in the upper left, the tracking chambers in the lower left and the region around the primary vertex with non-vertex fitted particle tracks in right figure. The secondary vertex of the event has a vertex multiplicity of 4 tracks. The decay length is $l = 2.2$ mm with a decay-length significance of $l/\sigma_l = 13.6$. The transverse energy of the corresponding jet is $E_T = 20.3$ GeV.

2. Start values for the primary vertex and for a secondary vertex are chosen. For the primary vertex the position of the default vertex or the run vertex is used whereas the secondary vertex is selected along the jet axis outside the beam envelope with a minimal separation to the primary vertex of $l_{\text{sep}} \geq E_{T,\text{jet}} \cdot 0.003 \frac{\text{cm}}{\text{GeV}}$ where the secondary vertex is supposed to be.
3. The start temperature is set to an experimentally optimized value of $T = 36$.
4. Weights w_{ij} for the selected tracks are calculated according to equation (3.18).
5. The primary and secondary vertex are refitted with all tracks taking into account the weights calculated in step 4. For the primary vertex fits, all tracks with weaker selection criteria are considered.
6. The temperature is decreased in iteration steps. It turned out to be useful to decrease the temperature according to the following scheme $T = \{25, 16, 9, 4, 2, 1, 1\}$. The fit procedure is repeated from point 4 on. The algorithm stops if the last temperature is reached.

After the fit procedure, the decay-length is calculated with the actual primary and secondary vertex. The vertex multiplicity is determined by tracks contributing significantly to the secondary vertex. In this analysis tracks with a weight $w_{ij}(1) \geq 0.8$ are considered.

3.4.3 Extraction of the heavy quark fraction

The measured distribution of decay-length significance is expected to have at least two components. One component originates from decaying hadrons producing a secondary vertex with positive decay length with respect to the jet axis. This component has an exponentially falling contribution to the positive decay-length significance. The other component consists of events with one or several tracks with large errors faking a secondary vertex. Since this is not related to the production of a real secondary vertex, this component has a symmetrical, gaussian-like contribution to the signal centered at zero. The second component is a consequence of the limited resolution of track reconstruction.

Fraction fitter The measured S_i distribution is fitted under the hypothesis that it consists of beauty, charm and light quark (uds) components. The different shapes of the expected contributions are taken from MC simulation and are kept fixed. The relative normalizations are left free and are fitted to the measured data. Also contributions from light quarks are considered since they can contribute to the signal either by hadrons with strangeness or by tracks faking a secondary vertex.

The fitter used for the fit procedure is based on a maximum likelihood technique and is described in [50]. This fitter was developed to fit shapes from different MC sources to a binned data distribution. The advantage of this fit procedure is that it takes into account statistical fluctuations of finite MC samples. In addition, the fitter is able to consider weighted MC samples. It can also handle bins with only few entries since the errors for each data and MC bin are assumed to be Poisson distributed. Finally, the fitter is also designed for a correct treatment of bins with no event from a MC source.

Chapter 4

Event selection

In this chapter the selection of events from this data set is described. It starts with the description of the trigger used for this analysis. After this the selection criteria for jets are given and properties of jets are compared with MC events. Finally, the secondary vertex fitter is applied to this subset of data and relevant variables for the vertex fit are again compared with the MC predictions.

The data set used for this analysis comprises the events from e^+p collisions of the years 1999 and 2000. During this period the detector and the collider were operating with high performance and stable conditions.

4.1 Tagged photoproduction

This analysis is restricted to tagged photoproduction. In photoproduction the interacting electron is scattered by a small angle and cannot be detected by the main detector. Tagged photoproduction means that the electron is explicitly detected and measured by the luminosity system. In this analysis only the electron tagger (ET33) at $z = -33.4$ m is used, which has a large and well studied acceptance. The other electron taggers at $z = -43.2$ m and $z = -8.0$ m are ignored because they have a smaller statistical contribution.

4.1.1 Acceptance of electron tagger

The acceptance of the ET33 is sensitive to the tilt of the e -beam and also depends on the inelasticity y . The dependence on y is determined from data by iteratively tuning MC events to data (see also [51]). The measured acceptance is parameterized for different run periods and written to the H1 database. There are 6 parameterizations for the 1999 e^+ data and 8 for the 2000 data as shown in figure 4.1.

To avoid energy losses at the border of the 15.4 cm wide detector, only electrons with an impact position within the central region of 13 cm are selected. This ensures that the electron has deposited the complete energy in the detector. This cut is also considered in the determination of the ET33 acceptance.

Only the kinematical region with inelasticity of

$$0.28 < y < 0.65 \tag{4.1}$$

is considered in this analysis. To avoid regions with small acceptance, this cut ensures that the acceptance of the electron tagger is greater than approximately 10% for each event.

The response of the ET33 is not simulated by H1SIM due to the strong dependence on the beam optics which is not simulated. When comparing MC events to data the acceptance of the electron tagger must be included. In principle the acceptance can be corrected in data or MC events. In this analysis the latter possibility is applied since the fraction fitter requires unweighted data as input.

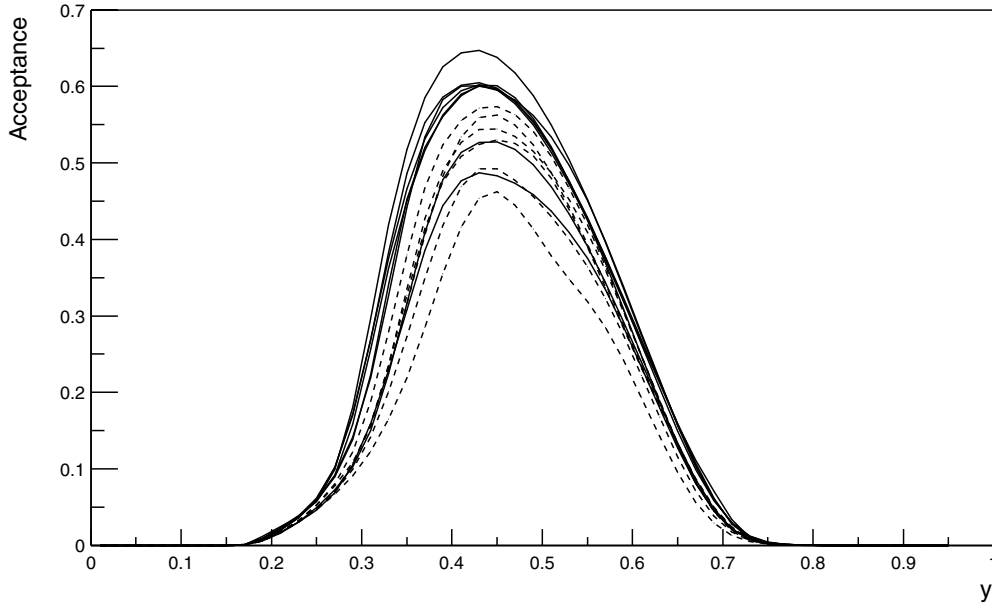


Figure 4.1: Acceptance of the electron tagger as obtained from the H1 database. There are different parameterizations for the 1999 e^+p data (*dotted lines*) and for the 2000 data (*solid lines*) depending on run periods.

4.1.2 Level 1 Trigger

To select tagged photoproduction events, the level 1 subtrigger 83 is used. Besides the trigger element from the ET33, this subtrigger is composed of several additional trigger elements which mainly suppress beam-gas and soft events. The exact definition of the subtrigger 83 and the trigger elements for the analyzed data sample is given in section A.1 of the appendix. The main requirements for the subtrigger 83 are:

- An electron is detected with the ET33 and no photon is detected by the photon detector (LU_ET&&!LU_PD_low). The latter requirement suppresses Bethe-Heitler processes.
- At least three tracks with a transverse momentum $p_T > 400$ MeV are found by the DCr ϕ trigger.
- Tracks found by the proportional chambers have to point to the nominal event vertex.
- Interactions from protons with rest gas in the backward region are excluded by accepting events with hits in the most backward quarter of the CIP only in conjunction with energy deposition in the electromagnetic part of the SpaCal.
- Several timing information of sub detectors (CIP/COP, ToF, VLQToF) are used to suppress background events. The timing information of these components is compared with the nominal timing window of ep -collisions. Events outside that window are rejected.

Since the requirements of the subtrigger 83 are satisfied quite often, the trigger rate of this subtrigger is reduced by applying prescale factors. This is necessary to avoid an excess of the fixed output bandwidth. In this case, events triggered by the subtrigger 83 are rejected at random by a probability related to a run-dependent prescale factor. The effect of prescale factors are taken into account in the calculation of the integrated luminosity.

Trigger efficiency

Besides the efficiency of the electron tagger, the efficiency of the remaining trigger elements of the subtrigger 83 can be measured with help of a reference trigger. The subtrigger 69 is well suited for this since this subtrigger is only composed of the trigger element from the electron tagger. Due to the high trigger rate of the electron tagger the subtrigger 69 has a large prescale factor of about 150.

The efficiency of the subtrigger 83 without the trigger element from the electron tagger can be calculated according to

$$\epsilon_{\text{ST83}\setminus\text{ET}} = \frac{N_{\text{ST83}} \cap N_{\text{ST69}}}{N_{\text{ST69}}}. \quad (4.2)$$

In this equation $N_{\text{ST}i}$ denotes the number of recorded events by subtrigger i and \cap means coincidence of two subtriggers. The results are shown in table 4.2. Since the prescale factor of the

Trigger Element (TE)		Data [%]	MC simulation		
			uds [%]	charm [%]	beauty [%]
$E_T^{\text{Jet1}} > 6 \text{ GeV}, E_T^{\text{Jet2}} > 6 \text{ GeV}, \eta_{\text{Jet}} < 1.5$					
DCRPh_Tc	TE 19	98.84 ± 0.33	98.01 ± 0.03	98.40 ± 0.02	98.58 ± 0.04
zVtx_sig:2>1	TE 31	93.32 ± 0.78	96.21 ± 0.03	97.32 ± 0.03	98.10 ± 0.05
!CIPB_noSPCLE.T_E1	TE 74	96.81 ± 0.55	(100.00)	(100.00)	(100.00)
!SPCLE.AToF.E_1	TE190	99.81 ± 0.14	(100.00)	(100.00)	(100.00)
ST83 \ (LU_ET&&!LU_PD_low)		89.45 ± 0.96	94.43 ± 0.04	95.81 ± 0.03	96.72 ± 0.06
$E_T^{\text{Jet1}} > 9 \text{ GeV}, E_T^{\text{Jet2}} > 7 \text{ GeV}, \eta_{\text{Jet}} < 1.0$					
DCRPh_Tc	TE 19	99.25 ± 0.53	98.01 ± 0.03	98.65 ± 0.04	98.65 ± 0.07
zVtx_sig:2>1	TE 31	93.26 ± 1.53	96.21 ± 0.03	98.00 ± 0.05	98.59 ± 0.08
!CIPB_noSPCLE.T_E1	TE 74	97.38 ± 0.98	(100.000)	(100.00)	(100.00)
!SPCLE.AToF.E_1	TE190	99.63 ± 0.37	(100.00)	(100.00)	(100.00)
ST83 \ (LU_ET&&!LU_PD_low)		91.01 ± 1.75	94.43 ± 0.04	96.70 ± 0.06	97.26 ± 0.10
$E_T^{\text{Jet1}} > 9 \text{ GeV}, E_T^{\text{Jet2}} > 7 \text{ GeV}, \eta_{\text{Jet}} < 1.0, \text{secondary vertex found}$					
DCRPh_Tc	TE 19	(100.00)	98.66 ± 0.11	98.85 ± 0.07	98.73 ± 0.10
zVtx_sig:2>1	TE 31	98.39 ± 1.60	98.32 ± 0.13	98.92 ± 0.07	99.24 ± 0.08
!CIPB_noSPCLE.T_E1	TE 74	96.77 ± 2.24	(100.00)	(100.00)	(100.00)
!SPCLE.AToF.E_1	TE190	(100.00)	(100.00)	(100.00)	(100.00)
ST83 \ (LU_ET&&!LU_PD_low)		95.16 ± 2.73	97.04 ± 0.17	97.78 ± 0.10	97.98 ± 0.12

Table 4.1: Efficiency of dedicated trigger elements of the subtrigger 83 for different kinematical requirements.

subtrigger 69 is large, the statistics is limited and thus the errors on the efficiency are large. The trigger elements of the $DCr\phi$ and $zVtx$ trigger are also included in the MC simulation and show good agreement especially in the kinematical region used in this analysis. In addition, the MC simulation shows a slight dependence on the quark flavour.

Since the detector response of the ET33 is not simulated in MC events, the simulation of the subtrigger 83 is not complete. The subtrigger's effect is incorporated in MC events by the following corrections:

- MC events are weighted according to the parameterized acceptance of the ET33.
- For the remaining trigger elements, the simulation of the detector response is used. The difference between the measurement and the values from MC of about 2.5% is considered as systematic error.

4.1.3 Luminosity calculation

The luminosity is measured through the Bethe-Heitler scattering process $ep \rightarrow ep\gamma$ which has a well-known cross section. The main background contributing to the cross section measurement is the additional bremsstrahlung process of an electron with the rest gas in the beam pipe $eA \rightarrow eA\gamma$. This rate is determined by electron pilot bunches and is subtracted from the luminosity measurement. The relative error of the luminosity measurement is 1.5% [52].

Data events are only accepted if the detector components relevant for this analysis were switched on and their readout chain was operational. These relevant detector components are the CJC and CST for track reconstruction, the LAr and SpaCal for the measurement of the total energy, the luminosity including the electron tagger to detect the scattered electron and the CIP/COP, TOF and VETO systems for event triggering. When calculating the integrated luminosity, only runs fulfilling these requirements are counted. In addition, the general classification *medium* and *good* run quality is demanded.

Table 4.2 shows the integrated luminosity \mathcal{L} for the 1999 (positron) and 2000 data. The run

Integrated luminosity	1999	2000	1999/2000
Selected run range	246159-259461	262204-278690 278070-279215	
Accepted runs	2528	4622	7150
Average prescale factor	1.054	1.212	1.171
Satellite bunch correction	0.961	0.956	0.957
\mathcal{L} after all corrections	13.73 pb ⁻¹	39.08 pb ⁻¹	52.81 pb ⁻¹

Table 4.2: Integrated luminosity of the analyzed data set

period during the year 2000 with a shifted vertex is excluded because it constitutes a completely different detector setup.

Two additional corrections are applied to the calculated integrated luminosity. First, the prescale factor of the subtrigger 83 is taken into account. The second correction is the consideration of satellite bunches. These bunches consist of protons that are lost in regular proton bunches and accumulate on meta stable trajectories between two proton bunches. Since the timing resolution of the luminosity system is not good enough to exclude contributions from satellite bunches, a correction factor is applied.

4.1.4 Level 4 trigger

For events triggered by the ET33, only the trigger levels 1 and 4 of the H1 trigger system described in section 6.2 are relevant since level 2 is transparent for the subtrigger 83 and the level 3 trigger was not active until the year 2000.

At level 4, events are classified by final state finders into predefined physical classes which mainly are based on hard scales. An additional prescale factor called *event weight* is applied to events that are not found by any final state saver. Events which are classified by a final state saver are not weighted. The event weight depends on the measured Q^2 and is larger than 20 for $Q^2 \rightarrow 0$. Like the level 1 prescale factor, the level 4 weight is run-dependent.

There are two alternative ways to handle event weights. Either the analysis is restricted to one physical class of level 4 and the efficiency of this class is determined or events are counted according to their event weight.

Here the latter method has been chosen since the events in the final selection are distributed over several event classes and most of the events are unweighted. In figure 4.2 the classification of triggered events fulfilling the required jet criteria is shown. The dominant classes are the open heavy flavour class (15), the high E_T jet class (7) and the high Q^2 class (4). The latter class is unexpected for photoproduction events but this classification is a consequence of the 2-jet signature. To exclude possible overlaying high- Q^2 events it was checked that no scattered electron

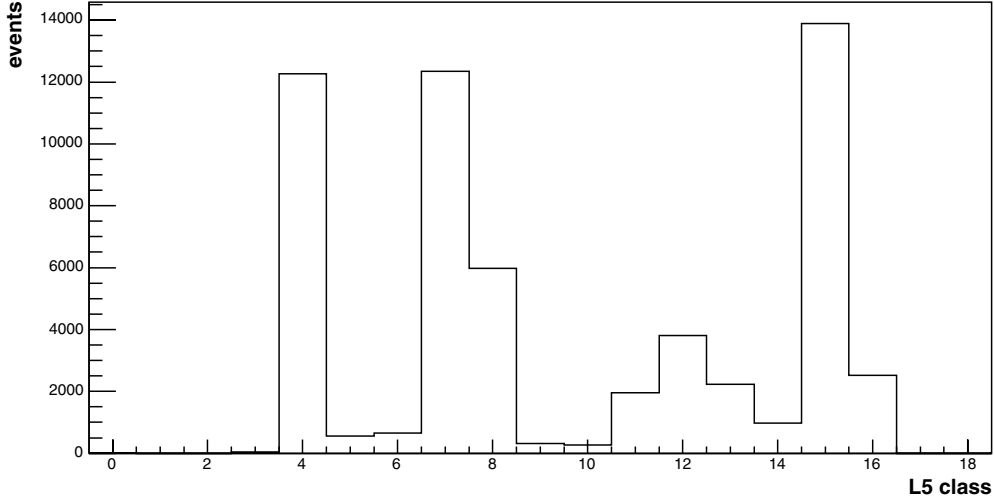


Figure 4.2: L4 classification of selected events. The important classes are: Open heavy flavour (15), High E_T jet (7) and High Q^2 (4). Soft events with an event weight are in class 3.

(electromagnetic cluster in the calorimeter) was found in the main detector. The small fraction of events from class (3) are not found by any final state saver and are weighted with an event weight.

A major problem when working with weighted events is that they have large contribution to the statistical error. In the final selection it is shown that the contribution of weighted events is marginal.

4.2 Non ep background suppression

A number of standard cuts and finders were applied to reject background events which were not produced in the primary ep interaction. Since the detection of the scattered electron already offers a data sample with high purity, only a marginal number of events are rejected.

- The background finder QBGFMAR [53], which mainly identifies cosmic muons, was applied to the data set. Since the coincidence of a tagged photoproduction event with a cosmic muon is rather unlikely, only few events in the photoproduction sample were identified as cosmic overlays.
- Cosmic overlaying event can often be identified by missing transverse momentum p_T^{miss} . In this analysis $p_T^{\text{miss}} < 20 \text{ GeV}$ was required.
- Events with a vertex outside the nominal interaction region $-35 \text{ cm} < z_{\text{vtx}} < 35 \text{ cm}$ are rejected. The distribution of the z -vertex is shown in figure 4.3.
- Events are rejected if the timing information from the CJC is not compatible with the timing window from the bunch crossing.
- Non- ep background is also identified by the longitudinal hadronic energy $E - p_z = \sum_i E_i - p_{z,i}$. In this analysis the cut $10 \text{ GeV} < E - p_z < 50 \text{ GeV}$ was applied.

About 1% of the selected data events are rejected by these cuts. The same cuts reject only 0.2% of the simulated MC events, independent of their quark flavour.

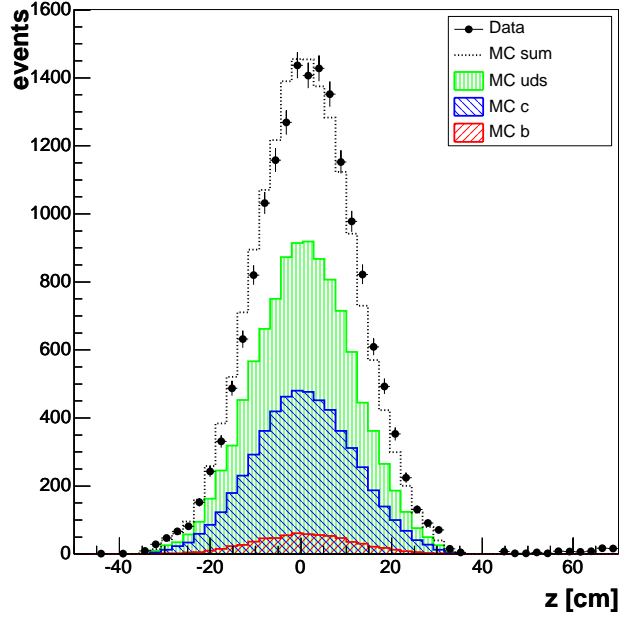


Figure 4.3: Distribution of the z vertex for MC events and data.

4.3 Jet selection

Jets are reconstructed using the longitudinal invariant k_T jet algorithm described in section 3.3.1. Due to the invariance under Lorentz transformations along the z -axis, the jet algorithm can be applied in the laboratory frame for photoproduction. A first cut on the transverse energy of $E_{T,j} = 6$ GeV was applied to the list all jets found by the jet algorithm.

The required transverse jet energy for the most energetic jet $E_{T,1} > 9$ GeV and $E_{T,2} > 7$ GeV for the second jet is chosen asymmetric. Events are only selected if the first and second jet are within the rapidity range of $|\eta_{\text{jet},1}| < 1$ and $|\eta_{\text{jet},2}| < 1$.

The main reason for the narrow cut in rapidity of the jets is the limited acceptance of the CST. Tracks originating from the H1 origin can be detected by the CST if their rapidity $|\eta_{\text{track}}| < 1.5$. Since tracks to build a secondary vertex are selected within a cone of 1 around the jet axis, this axis should be smaller in rapidity than $\eta_{\text{track}}^{\text{max}}$. Increasing the rapidity cut for jets $\eta_{\text{jet},i}$ from 1 to 1.5 increases the number of reconstructed secondary vertices by 30%. Another reason for the rapidity cut for the jets is that the correction of jet pedestals can be avoided (see next section).

The final jet cuts are summarized in table 4.3. Only the two most energetic jets are considered

Number of jets	$n_{\text{jet}} \geq 2$
Transverse energy of most energetic jet	$E_{T,1} > 9$ GeV
Transverse energy of second jet	$E_{T,2} > 7$ GeV
Transverse energy for additional jets	$E_{T,j} > 6$ GeV
Pseudo-rapidity of first jet	$-1 < \eta_{\text{jet},1} < 1$
Pseudo-rapidity of second jet	$-1 < \eta_{\text{jet},2} < 1$

Table 4.3: Definition of Jet phase space.

for the determination of secondary vertices. Events with an additional third jet are not rejected.

4.3.1 Jet pedestal

In the picture of the LO BGF the complete energy of the hard interaction is found in the reconstructed jets. Due to QCD emission, multiple interactions and fragmentation effects of the proton remnant an additional energy flow is created which is almost independent of the direction of the initial parton from the hard process. The result of these effects is an energy flow flat in η - ϕ inside as also outside the jet cone and is called *jet pedestal*.

The transverse energy of a jet reconstructed by the jet algorithm always includes this pedestal. Since the selection of events for the search of secondary vertices is mainly based on the jet energy, it is crucial that the steeply falling spectra of the transverse energy flow is correctly normalized in data as in MC.

Multiple interactions based on phenomenological models are included in the PYTHIA MC event generator and were tuned to describe data [54]. The quality of the description of jet pedestals in MC events is checked in the following.

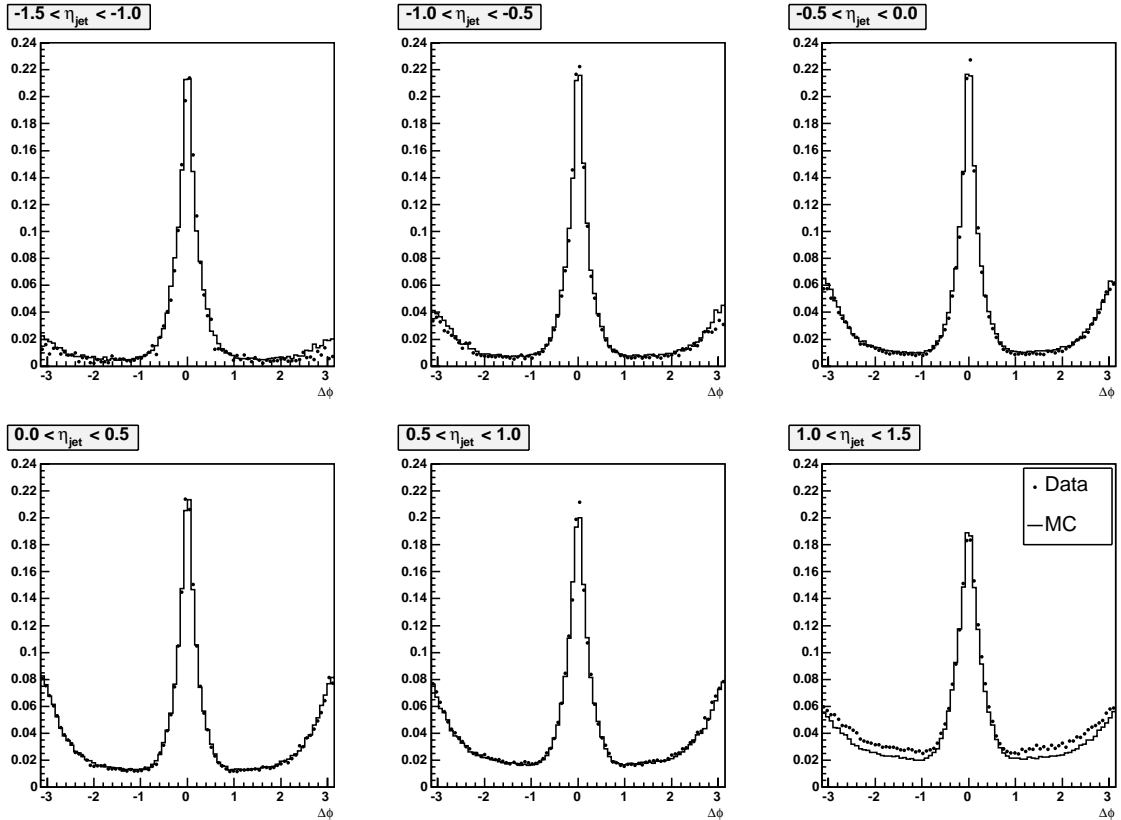


Figure 4.4: Jet profiles for several bins in jet rapidity in arbitrary units. To compare MC events and data, the distributions are normalized to the jet cone of size $\Delta\phi = \pm 0.5$.

In figure 4.4 so-called jet profiles are shown for different bins in η of the jet. A jet profile shows the azimuthal energy distribution around a jet axis for several events. Each HFS object within a rapidity slice of 2 with respect to the jet axis is considered. For the jet profiles 2 or more jet events with at least 6 GeV are selected. The second jet is visible as an increase in energy flow at $\pm\pi$. The energy flow outside the jet cone is well described by the PYTHIA MC with exception of the rapidity range $1 < \eta_{\text{jet}} < 1.5$ due to the proton remnant.

The jet pedestals can be measured by summing up the energy from all HFS objects in the area between $-2 < \Delta\phi < -1$ and $1 < \Delta\phi < 2$ in a rapidity slice around the jet axis (see figure 4.5). The measured energy E_{ped} of the jet pedestal per unit in the η - ϕ plane is shown in figure 4.6 for all

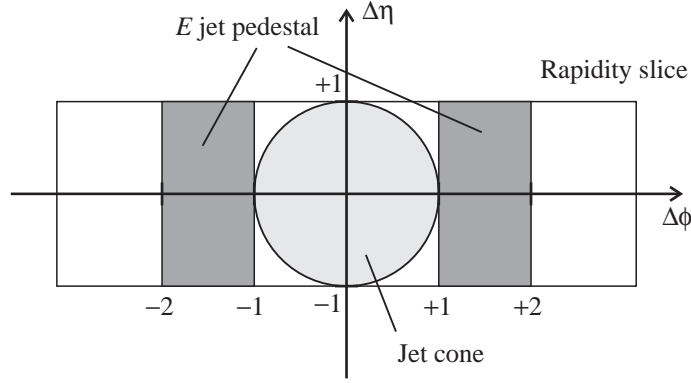


Figure 4.5: Rapidity slice with a jet cone. The shaded area is used to measure the energy of the jet pedestal.

events and events with a $x_\gamma > 0.65$ cut. The jet cuts (9 GeV for the leading jet and 7 GeV for the

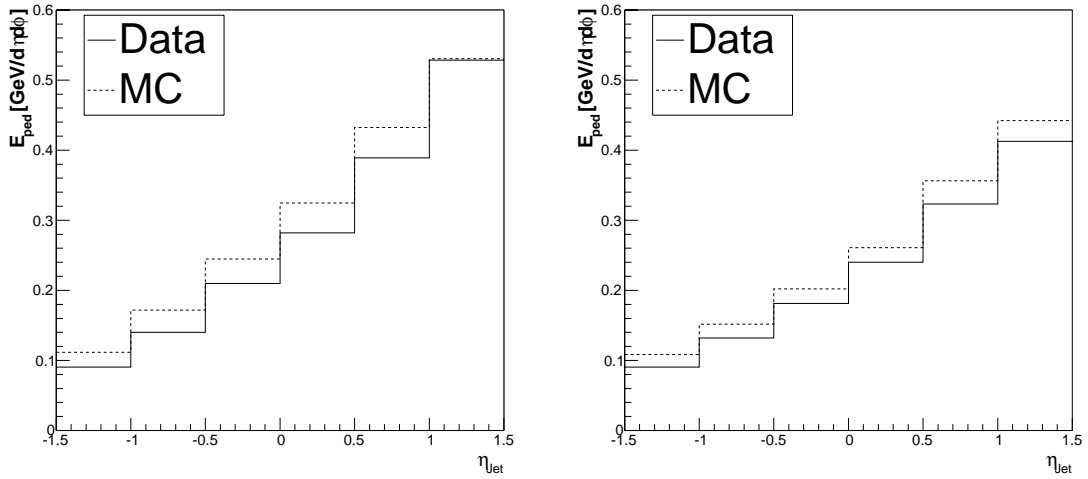


Figure 4.6: Energy of jet pedestal as function of the jet rapidity for all events (left) and for events with cut on $x_\gamma > 0.65$ (right).

second jet) applied to these events correspond to the jet cuts used in this analysis. As expected from figure 4.4 the difference between data and the PYTHIA MC is small. It is noticeable that due to the higher jet cut the difference in the last bin ($1 < \eta_{\text{jet}} < 1.5$) between data and MC events is smaller than in figure 4.4. An explanation for this effect is that resolved processes with larger contributions to jet pedestals are stronger suppressed by a higher jet cut than direct processes. The measured values for the jet pedestals are of similar size as in another analysis [55].

Influence of jet pedestals Even though jet pedestals are quite well described by the MC simulation in the kinematical region relevant for this analysis, the absolute values of these pedestals have an important influence in particular when comparing with other experiments or with QCD predictions. If data events are selected by a jet cut, this cut includes the bare jet energy plus the underlying pedestal energy. On the other hand if a jet cut is applied in the NLO calculation, no jet pedestals are included and the jet cut is based on the bare jet energy. As a consequence the effective jet cut is lower in data than in the NLO calculation. In the following, the effect of this inconsistency is examined.

Principally the effect of missing jet pedestals can be compensated in the NLO calculation. To quantify this statement the rapidity-dependent pedestal energy is extracted from figure 4.6 and the jet cut in the NLO calculation is lowered by

$$\Delta E_T = E_{\text{ped}}(\eta_{\text{jet}}) \cdot A_{\text{cone}}. \quad (4.3)$$

In this equation, A_{cone} is the area of the jet cone in the η - ϕ plane. This procedure is only well-defined for the cone jet algorithm. In this case the cone area of the jet is $A_{\text{cone}} = \pi$.

For the longitudinal invariant k_T jet algorithm, the cone area is no longer a circle in the η - ϕ plane with a fixed size. To estimate the radius of such a cone, the variable R_x is introduced. It describes the minimal radius of a cone around the jet axis containing HFS objects with at least $x\%$ of the total transverse jet energy. The distribution for R_{60} and R_{95} are shown in figure 4.7. It is remarkable that in the R_{60} distribution the maxima for beauty jets is significantly higher

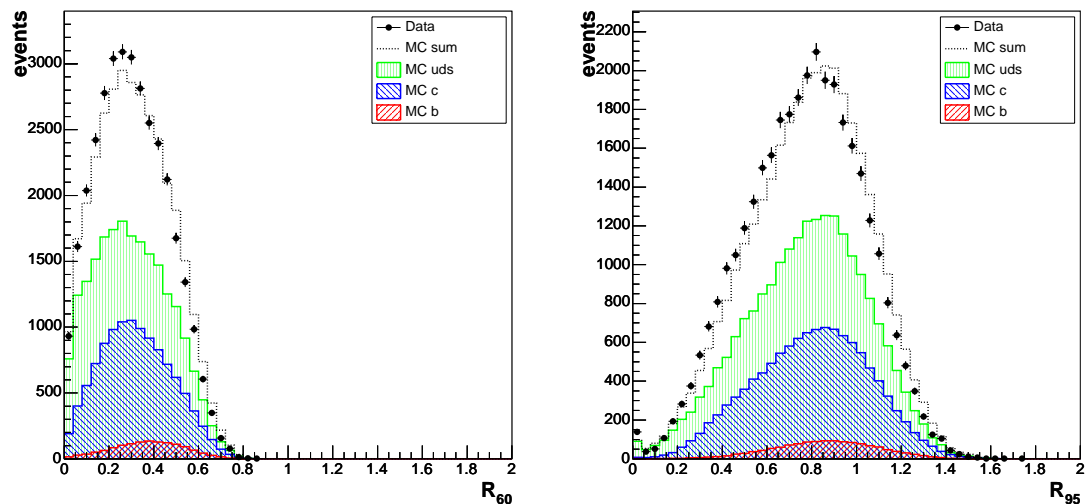


Figure 4.7: Minimal radius of a cone around the jet axis containing HFS objects with at least 60% (left) and 95% (right) of the total transverse jet energy.

than for charm and uds jets. This denotes that the energy flow in uds and charm jets is stronger collimated around the jet axis than for beauty jets. On the other hand, the maximal size of a jet is almost flavour independent as can be seen in the distribution of R_{95} . But the variation of the jet cone is large and in the measurement of the pedestal energy some HFS objects belonging to a jet are also counted as pedestal. In addition to the fuzzy cone size, the cone area is perforated. As a consequence it is not possible to find a well-defined size of the cone area.

Under the assumption that $A_{\text{cone}} = \pi$, the cross section from the NLO calculation (section 2.4) is increased by 26% for beauty and 43% for charm. If the pedestal energy is calculated with $A_{\text{cone}} = \pi/2$ the NLO cross section is 20% higher for beauty and 26% higher for charm. This shows that jet pedestals can have a large impact. On the other hand it is not clear how jet pedestals are correctly calculated and corrected in the framework of the k_T jet algorithm. This shows that a measured cross section should be compared with caution to calculations. However, jet pedestals are only relevant if measured results are compared with predictions of the calculation (see chapter 5) and therefore have no relevance for the following steps in the analysis .

Energy flow inside the jet Jet pedestals are mainly used to compare the energy flow outside the jet cone between MC events and data. The quality of the description inside the jet can be

verified with help of the first radial momentum M_r^1 which is defined for each jet as

$$M_r^1 = \frac{\sum_i E_{T,i} R_{i,\text{jet}}}{\sum_i E_{T,i}}, \quad (4.4)$$

where i runs over all HFS objects with transverse energy $E_{T,i}$ within the considered jet. $R_{i,\text{jet}}$ is the separation in the η - ϕ plane of this HFS object to the jet axis. The comparison of the first radial momentum between MC events and data is shown in figure 4.8 and shows good agreement. Again it is remarkable that jets from events with beauty have significantly higher values for the

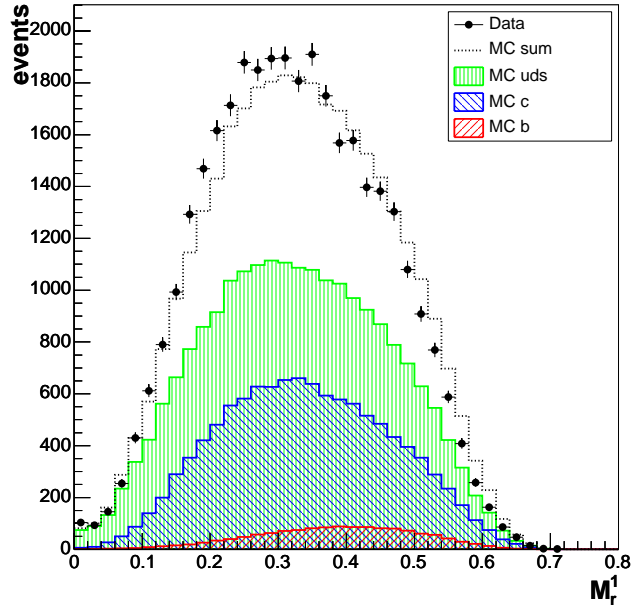


Figure 4.8: Distribution of the first radial moment M_r^1 .

first radial momentum than the events with charm or *uds* quarks. This demonstrates the fact that jets from beauty events are wider on average.

Figure 4.9 shows the distribution of the jet mass which is defined as

$$m_{\text{jet}} = \sqrt{\left(\sum_j p_j \right)^2}, \quad (4.5)$$

with p_j denoting the four momentum of each HFS object in the jet.

Both distributions show that the MC simulation is describing well the inner structure of jets.

4.3.2 Jet cut on generator level

Usually, the generation of a MC sample proceeds in two steps. First, the MC event generator is used to generate four-vectors of a simulated process. This step is rather fast and requires much less than 1 second CPU time per event. The second step is the complete detector simulation and reconstruction of the event by H1SIM which takes about 10-30 seconds of CPU time per event – depending on the track multiplicity of the event.

When jet cuts are applied in this analysis, most events from an all-inclusive MC set are rejected. The fraction of events kept after the jet requirement is shown in figure 4.10.

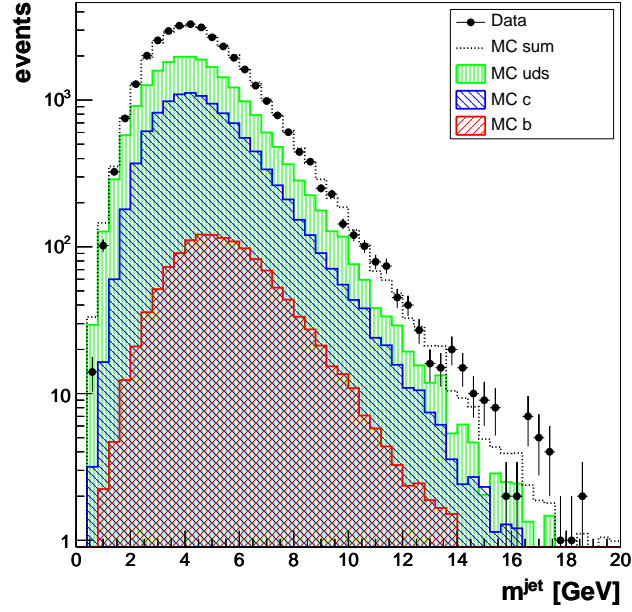
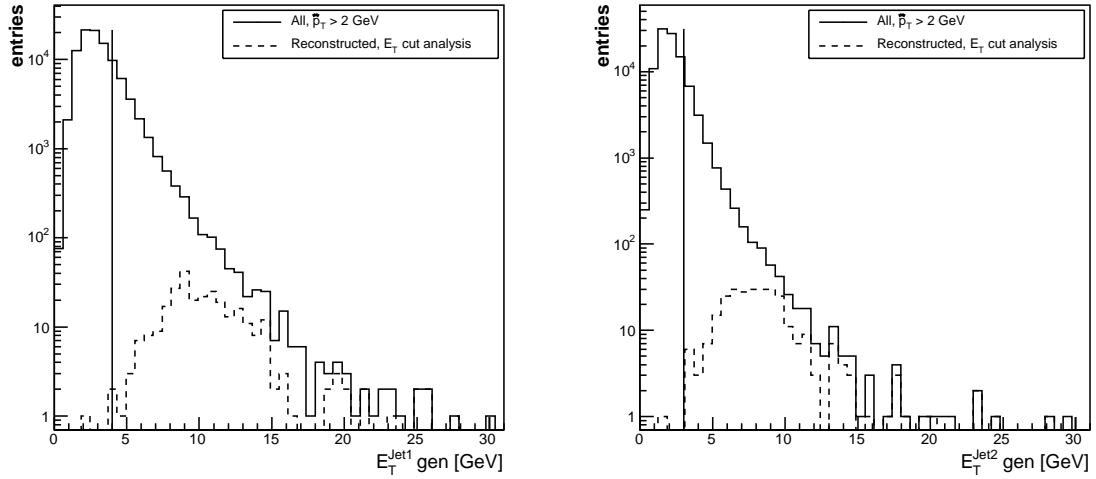
Figure 4.9: Distribution of the jet mass m_{jet} .

Figure 4.10: Jet E_T spectra measured at the generator level for the leading (*left*) and second (*right*) jet. The solid line shows the distribution of all jet events with a minimal $\hat{p}_T > 2$ GeV cut. A cut of $E_T^{\text{jet}1} > 9$ GeV and $E_T^{\text{jet}2} > 7$ GeV was applied on the jets after simulation and reconstruction. These distributions are shown as dotted lines. The vertical line indicates the jet cut applied on generator level for MC production.

Rejection with a \hat{p}_T -cut The common way to reject events with low jet E_T during MC event generation is to cut on the transverse momentum \hat{p}_T of the hard interaction. The correlation between \hat{p}_T and the jet energy is shown in figure 4.11. Since this distribution is wide, a rather low cut on \hat{p}_T is necessary to generate a MC sample with no or small losses by this cut.

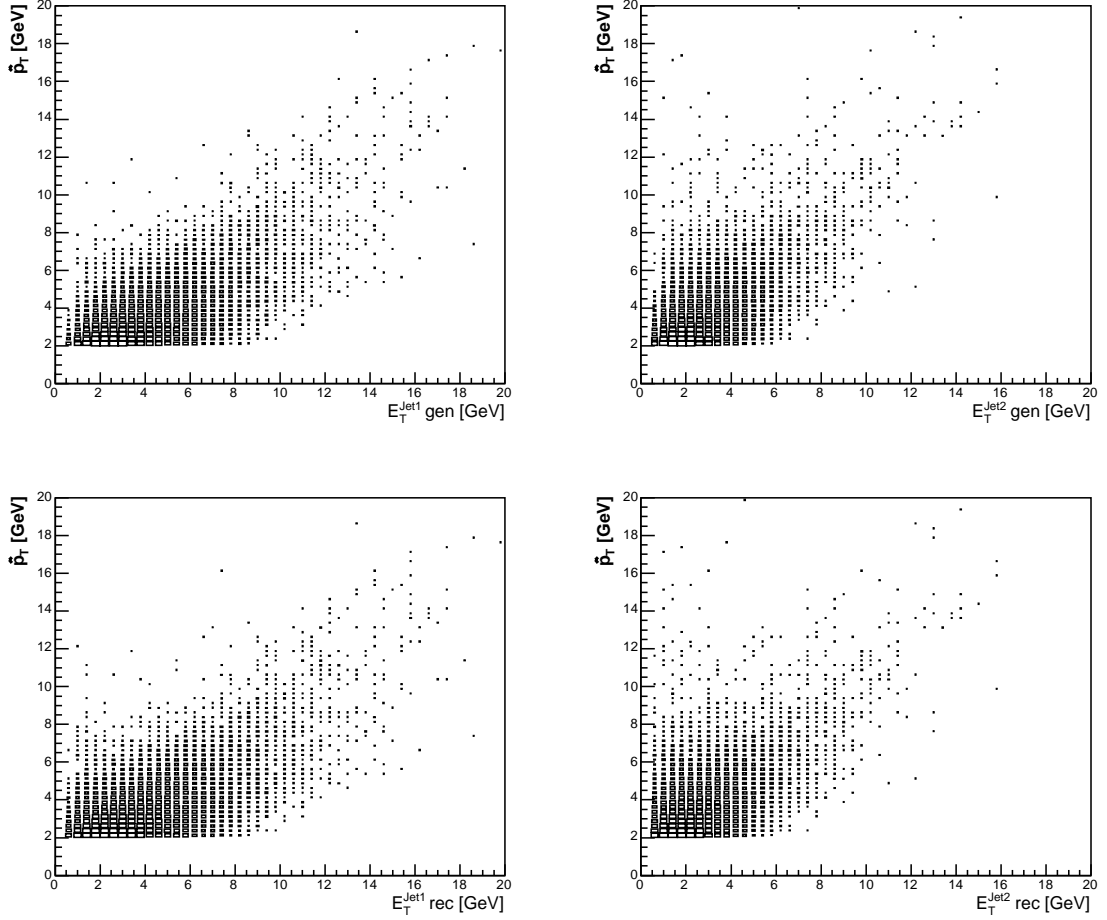


Figure 4.11: Correlation between \hat{p}_T and the generated jet energy. The left (right) column shows the correlation for the leading (second) jet. The upper (lower) row shows the jet energy measured on generator level (after reconstruction).

Rejection with a jet cut on generator level In order to generate a MC sample more efficiently, the cut on the transverse jet energy is applied in an appropriate way on generated events before the H1SIM step. Because the jet algorithm can also be applied to objects at generator level it is consequential to implement a similar jet cut to reject low- p_T events.

The correlation of transverse jet energies on generator level and after reconstruction was thoroughly studied in order to reject events with high efficiency but minimal loss of signal. As can be seen in figure 4.12 the standard deviation of the difference is about $\sigma_{\text{jet}}^{\text{gen/rec}} \approx 1 \text{ GeV}$ and is getting slightly smaller for higher transverse jet energies. Due to the broad resolution and also motivated by figure 4.10, the cuts shown in table 4.4 were applied to jets on generator level. The

Number of generator jets	$n_{\text{jet}}^{\text{gen}} \geq 2$
Transverse energy of most energetic generator jet	$E_{T,1}^{\text{gen}} > 4 \text{ GeV}$
Transverse energy of second generator jet	$E_{T,2}^{\text{gen}} > 3 \text{ GeV}$
Pseudo-rapidity of first generator jet	$-2.5 < \eta_{\text{jet},1}^{\text{gen}} < 2.5$
Pseudo-rapidity of second generator jet	$-2.5 < \eta_{\text{jet},2}^{\text{gen}} < 2.5$

Table 4.4: Jet cuts applied on generator level before simulation and reconstruction.

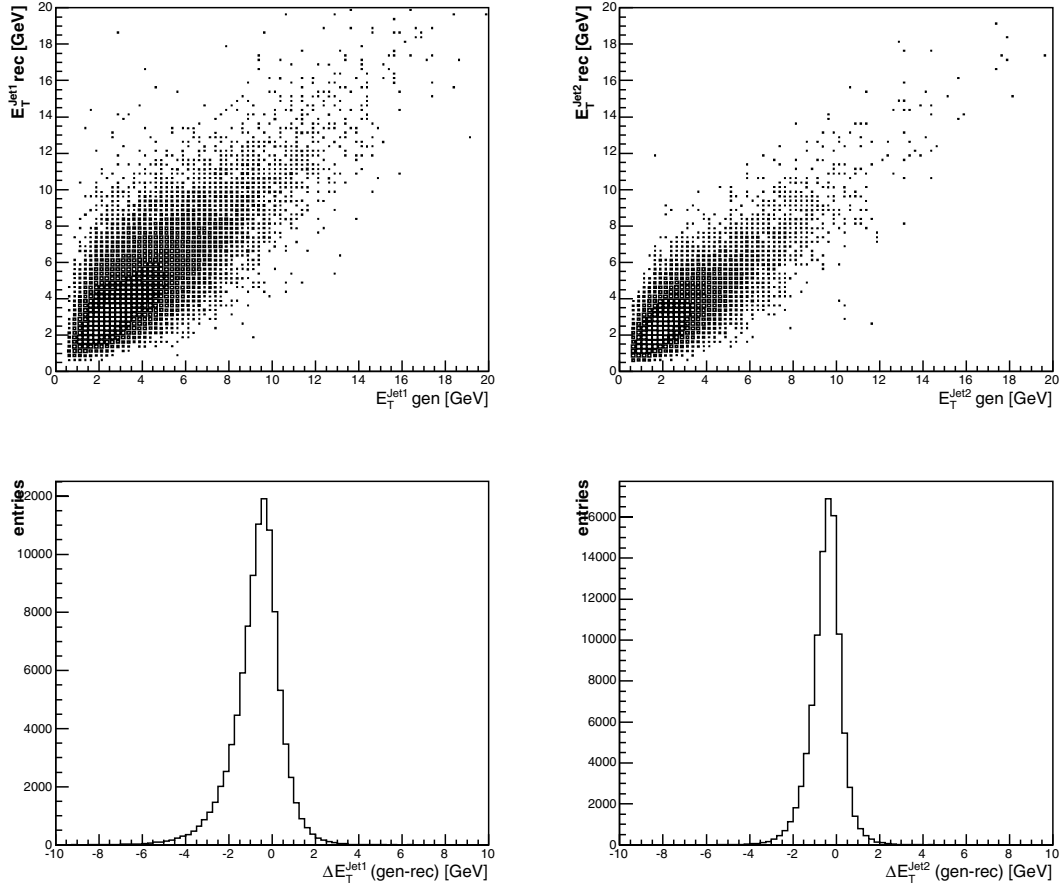


Figure 4.12: Correlation between E_T of jets on generator level and after H1SIM for the leading (left column) and second (right column) jet. Generated versus reconstructed jet energy is shown in the upper row and the difference is plotted in the lower row.

loss of MC events by this jet cut before simulation and reconstruction is less than 1% compared to the final jet cut. Therefore no correction was applied to the MC sample.

4.4 Comparison of data and MC events for base selection

In the following section, the kinematical and jet variables of the MC simulation are compared with data. In this analysis only the PYTHIA MC is considered. For a comparison with the HERWIG MC simulation see [56].

Since the absolute prediction of the all-inclusive PYTHIA MC is 15% above data, the MC sample is normalized to the data for the following figures as follows:

- The charm and beauty contributions of MC events are scaled by the fractions fitted from the decay-length significance distribution. The *uds* contribution is kept unscaled.
- The sum of the unscaled *uds* and the scaled charm and beauty contribution is normalized to data

In figure 4.13 the distribution for y and $\sum_i(E_i - p_{z,i}) = E - p_z = 2E_e y_{JB}$ is shown. In the

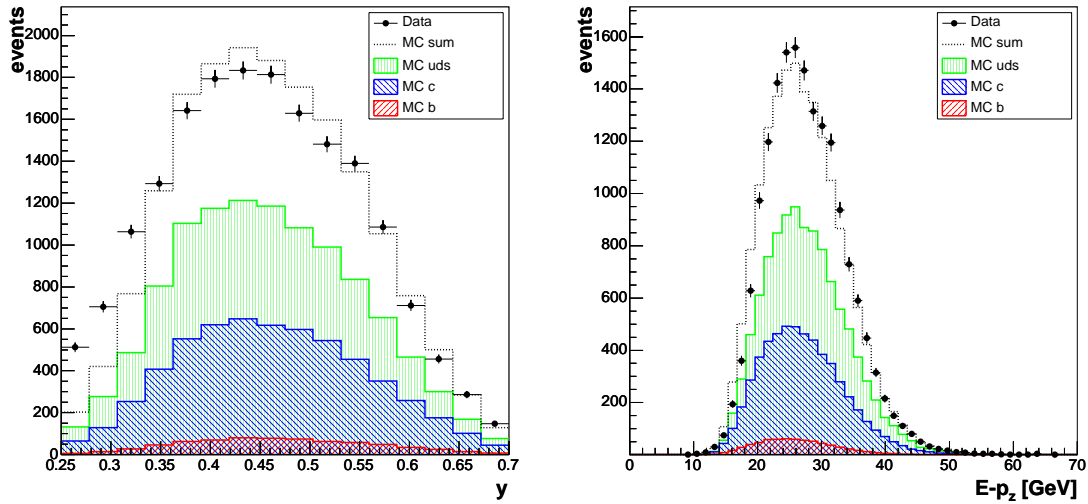


Figure 4.13: Distribution of inelasticity y (*left*) and longitudinal hadronic energy $E - p_z$ (*right*).

distribution of y , the MC simulation is below data for $y < 0.35$. A possible explanation for this deviation is that for MC events the generated value for y is plotted whereas for data the measured value from the electron tagger including the detector resolution is used. On the other hand the MC simulation is describing well the $E - p_z$ distribution.

In figure 4.14 the jet energy E_T and the jet rapidity η is plotted separately for the leading and the second jet. The E_T jet spectra are quite well described by the MC simulation for the leading as for the second jet.

On the other hand the rapidity distributions $\eta_{\text{jet}1,2}$ of the jet axis for the leading and the second jet show a clear discrepancy between MC and data. The fact that the sum of both rapidity distributions match better gives a hint for this behavior. The resolution of the jet energy is limited and as a consequence the list of jets ordered by jet energy can get mixed. Since the rapidity of jets is measured with higher precision the assignment of the jets ordered in rapidity is less ambiguous. This is shown in figure 4.15 for the forward and the backward jet.

4.4.1 Resolved contributions from MC events

Figure 4.16 shows the distribution of x_γ , calculated according to equation (3.15). Data is not well described by the MC events over the complete x_γ range. For the regime of direct processes with

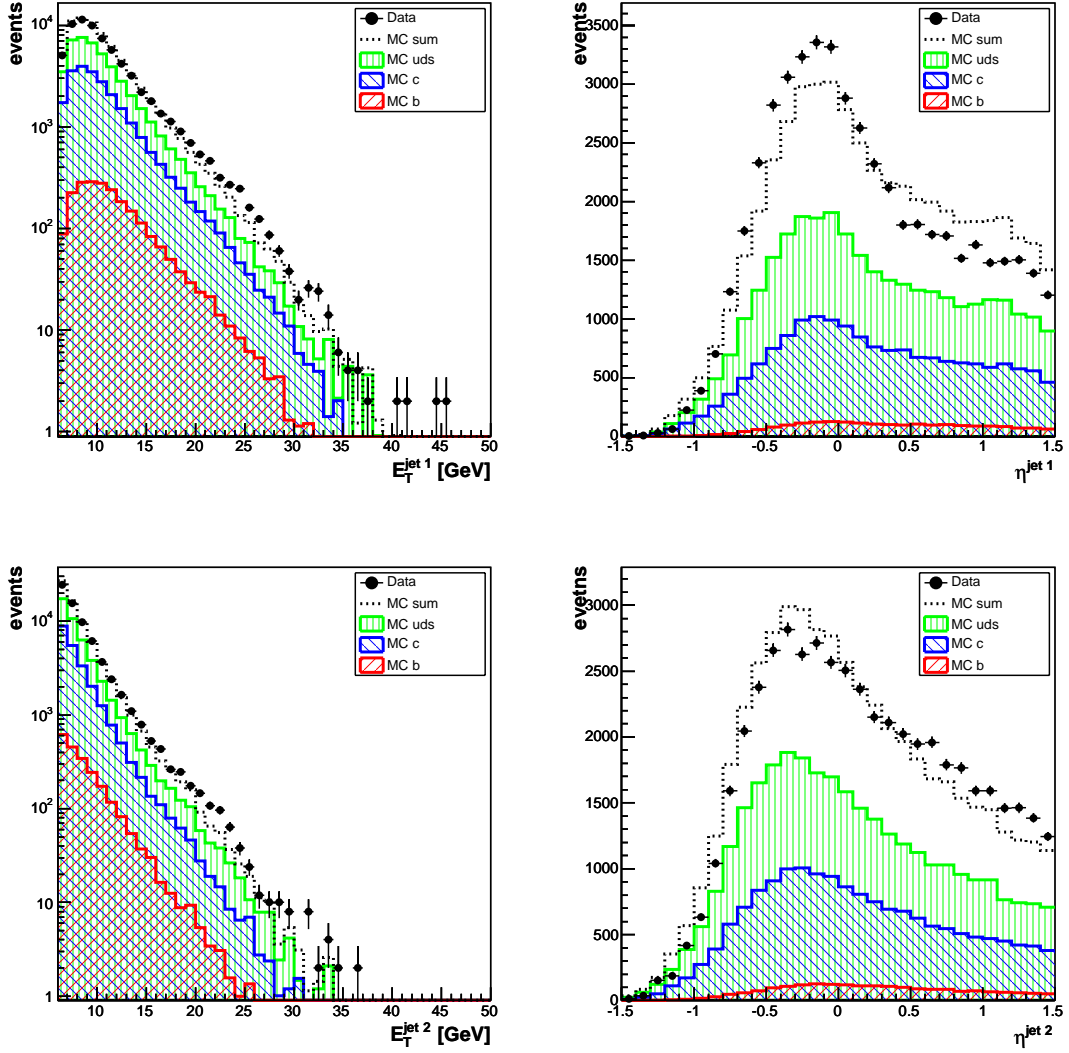


Figure 4.14: Distribution of the transverse jet energy E_T (left) and the jet rapidity η (right) for the leading (top) and the second jet (bottom).

$x_\gamma > 0.8$ data is underestimated by the MC simulation. On the other hand, the MC prediction overestimates the data in the range of $0.5 < x_\gamma < 0.8$ which is dominated by resolved processes.

The agreement between data and MC prediction is better if the resolved fraction of MC events is downscaled by 25%. The resulting distribution for x_γ is shown in figure 4.17. In this plot the number of simulated MC events is again normalized to data. A side-effect of this downscaling is that the predicted number of events from the MC simulation is in agreement with data. These two facts indicate that direct processes are reliably implemented in the MC simulation whereas for resolved processes at least the normalization seems not correct. This problem is suppressed by the cut on jet E_T which suppresses a large part of the resolved processes.

There are two consequences from these observations. First, a cut $x_\gamma > 0.65$ is applied to the reconstructed x_γ for data and MC simulation to be less sensitive to resolved contributions. Second, the discrepancy between the unscaled MC and data is considered as a systematic uncertainty.

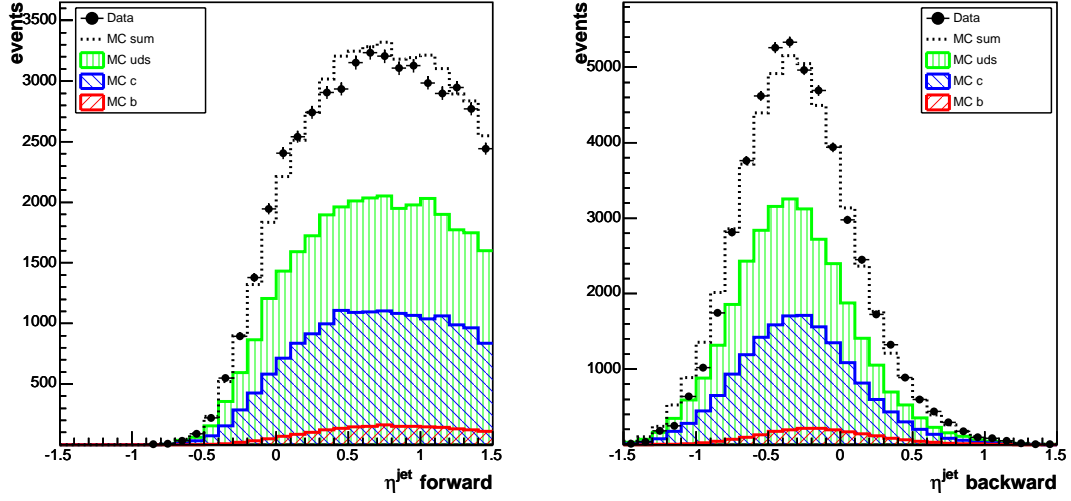


Figure 4.15: Distribution of the jet rapidity η for the forward (left) and the backward (right) jet.

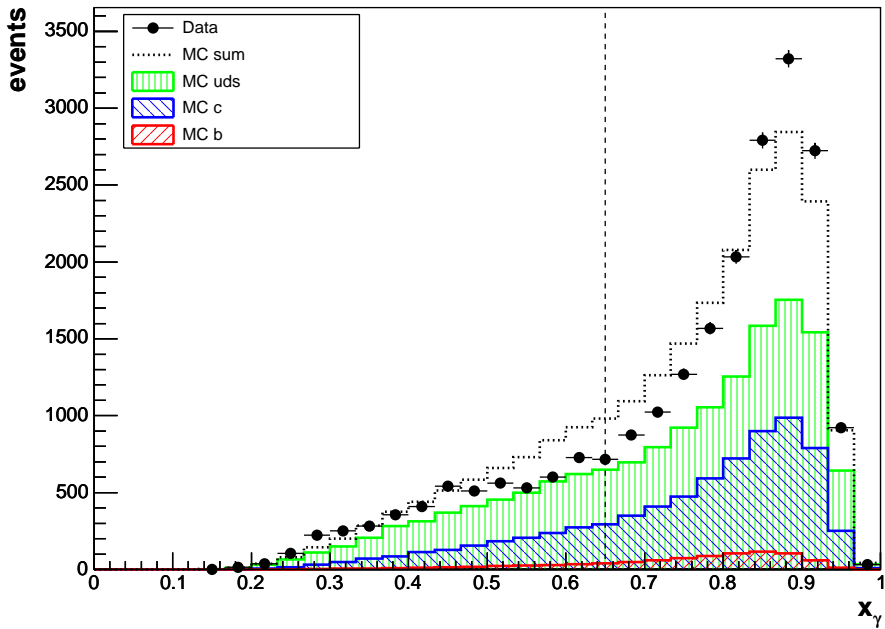


Figure 4.16: Distribution of x_γ for the selected kinematical region. The dotted line indicates the applied cut on x_γ .

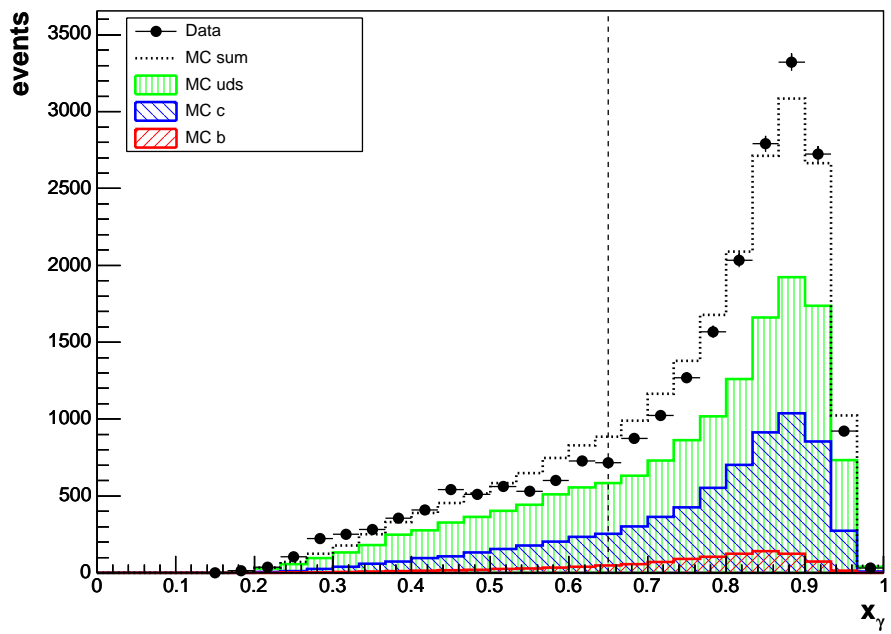


Figure 4.17: Distribution of x_γ after downscaling resolved MC events by 25%. The dotted line indicates the applied cut on x_γ .

4.5 Secondary vertex

For the reconstruction of secondary vertices it is crucial that tracks can be extrapolated to the interaction region with high precision. Multiple scattering and wrong linking of track hits destroy the good intrinsic detector resolution. For tracks with low momenta, multiple scattering is the main contribution to the track error and can be controlled by avoiding low- p_T tracks. Also wrong linking of hits is related to the p_T scale since a high p_T track segment can be extrapolated with higher precision to the next track fragment.

The selection cuts for tracks used for the reconstruction of a primary and secondary vertices are given in table 4.5. In order to minimize the error on the track extrapolation to the vertex,

Criteria	Primary vertex	Secondary vertex
p_T	> 400 MeV (in CJC)	> 500 MeV
d_{ca}	< 1.5 cm	-
d'_{ca}	-	< 0.2 cm
$ \eta $	-	< 1.5
l_{CJC}	> 22 cm	> 25 cm
r_{Start}	< 35 cm	< 45 cm
$n_{\text{CST}}^{\text{hits}}$	≥ 1	≥ 2
$p_{\text{CJC-CST}}$	> 0.1	> 0.1

Table 4.5: Track selection cuts for vertexing. The cuts applied on tracks for the secondary vertex fit are different and in general stronger than for the primary vertex fit.

a minimal reconstructed track length l_{CJC} in the CJC is required. In addition, the start radius r_{Start} of the reconstructed track must lie in CJC1. For primary (secondary) tracks 1 (2) hits in the CST on the p -side (r - ϕ plane) are required. Hits on the z side of the CST are ignored. The link probability $p_{\text{CJC-CST}}$ between the track reconstructed in the CJC and the CST hit must be > 0.1 .

The rapidity cut $|\eta| < 1.5$ for secondary tracks is mainly motivated by the geometrical acceptance of the CST. This requirement gives a clear cut-off also for tracks with a vertex shifted along the z -axis.

For primary (secondary) tracks a d_{ca} (d'_{ca}) cut is also applied to reject tracks which obviously do not point to the primary (secondary) vertex. This cut mainly intends to suppress decays from long-lived hadrons with strangeness.

4.5.1 Strangeness suppression

For an additional suppression of decaying hadrons with strangeness in the jet, a more elaborated cut than a simple d'_{ca} cut is applied. In general, tracks of strangeness decays in a jet have a small momentum p_T^{rel} relative to the jet axis. Consequently, they also have a small d'_{ca} .

The cut for strangeness suppression is based on an upper cut-off l_c for the decay length of a possible strangeness decay. The distance l between the crossing of a track with the jet axis and the primary vertex is (see also figure 4.18)

$$l = \frac{|d'_{ca}|}{|\sin(\phi_{\text{Track}} - \phi_{\text{Jet}})|}. \quad (4.6)$$

All tracks with $l > l_c$ are rejected. In the current analysis the cut-off parameter is set to $l_c = 0.4$ cm.

4.5.2 Comparison of MC with data for vertexing

The adaptive vertex fitter is applied to the leading and the second jet found by the jet algorithm. In 47% of the selected events the adaptive fitter cannot be executed successfully since there are

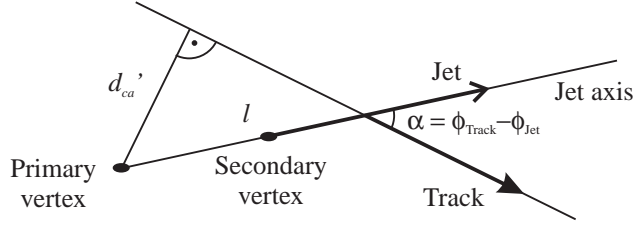


Figure 4.18: Relation of the d'_{ca} point of a track and the angle between the jet axis.

not enough tracks with the requested quality or the unconstrained fitter is not converging. In 41% the adaptive fitter has found a secondary vertex but finally didn't assign any track to the secondary vertex. One track is assigned in 11% and in about 1% a vertex with two tracks is found. A secondary vertex with 3 or more tracks is found in less than 0.2% of all selected two-jet events.

It is possible to find a vertex with one or more tracks in both jets of the same event (*double tagging*). Compared with events with single tagging, 15% of the events have a double tag. In most cases an event with a double tag consists of two vertices with a track multiplicity of one. To avoid problems with event counting, only one vertex per event is considered also for events with double tagging. In this case the vertex is selected according to the higher track multiplicity and – in second priority – to the higher decay length significance S_l .

Track multiplicity Since the adaptive vertex fitter is sensitive to the number of tracks, it is important that the number of tracks within the jet cone is described well by MC events. Figure 4.19 shows the number of all tracks in the jet cone and of all tracks which fulfil the required

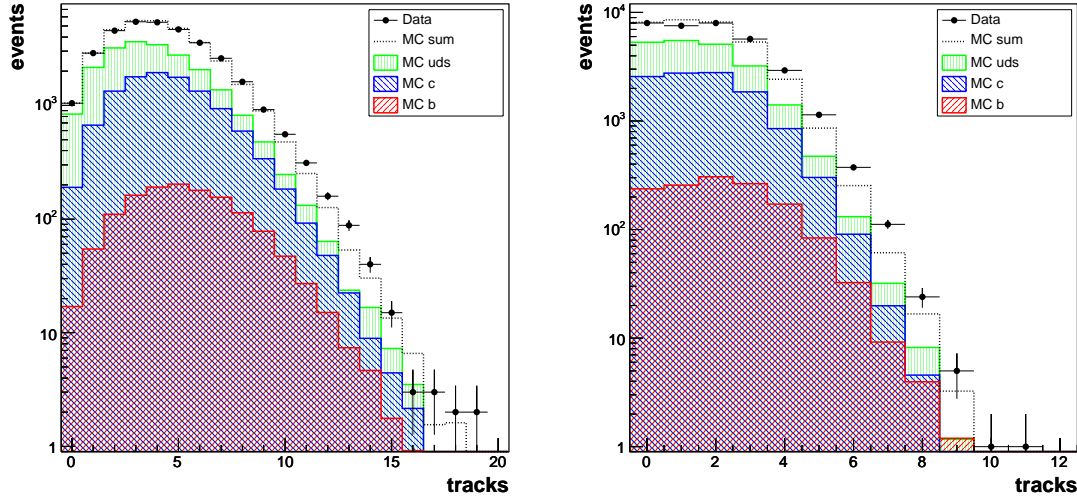


Figure 4.19: Number of tracks in the jet (*left*) and number of well measured tracks in the jet (*right*).

track quality. The track multiplicity found by the adaptive vertex fitter is shown in figure 4.20. The track multiplicities of the secondary vertex are excellently described by the MC simulation. Vertices with a multiplicity of 3 tracks are dominated by beauty events. For a multiplicity of 4 or more tracks only beauty events are found in the MC simulation.

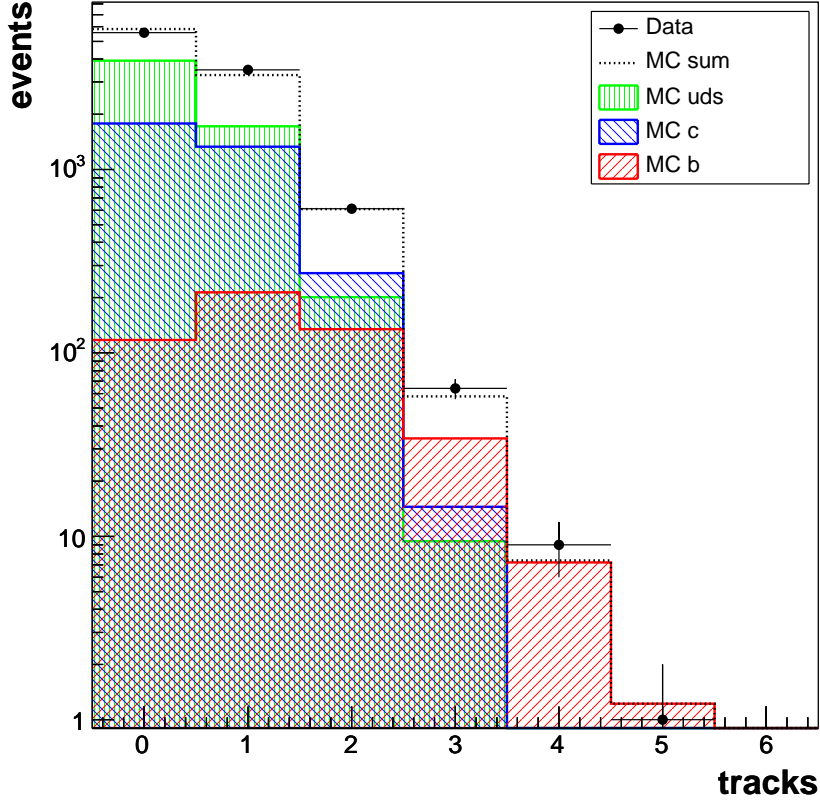


Figure 4.20: Track multiplicity of secondary vertices found by the adaptive vertex fitter.

Decay length The decay length l , the error on the decay length σ_l and the decay length significance S_l are shown in figure 4.21 for all vertices with a track multiplicity of at least one track.

The decay length l , the error on the decay length σ_l and the decay length significance S_l are plotted separately for each track multiplicity of the secondary vertex and are shown in figure 4.22. In this figure also vertices with no assigned tracks are shown. As expected, the error on these vertices are large and consequently their significance is small.

Invariant mass For vertices with a track multiplicity of 2 or more the invariant mass m_{2vx} of the vertex can be calculated. For each track assigned to the secondary vertex, a mass hypothesis of a pion with m_π is assumed. The distribution of the invariant mass is shown separately in figure 4.23 for vertices with a track multiplicity of 2 and 3 or more tracks. Simulated events show that events with an invariant mass larger than 1.8 GeV are dominated by beauty. This is consistent with the mass of the D^\pm and D^0 hadrons which are the main contributions to charmed events.

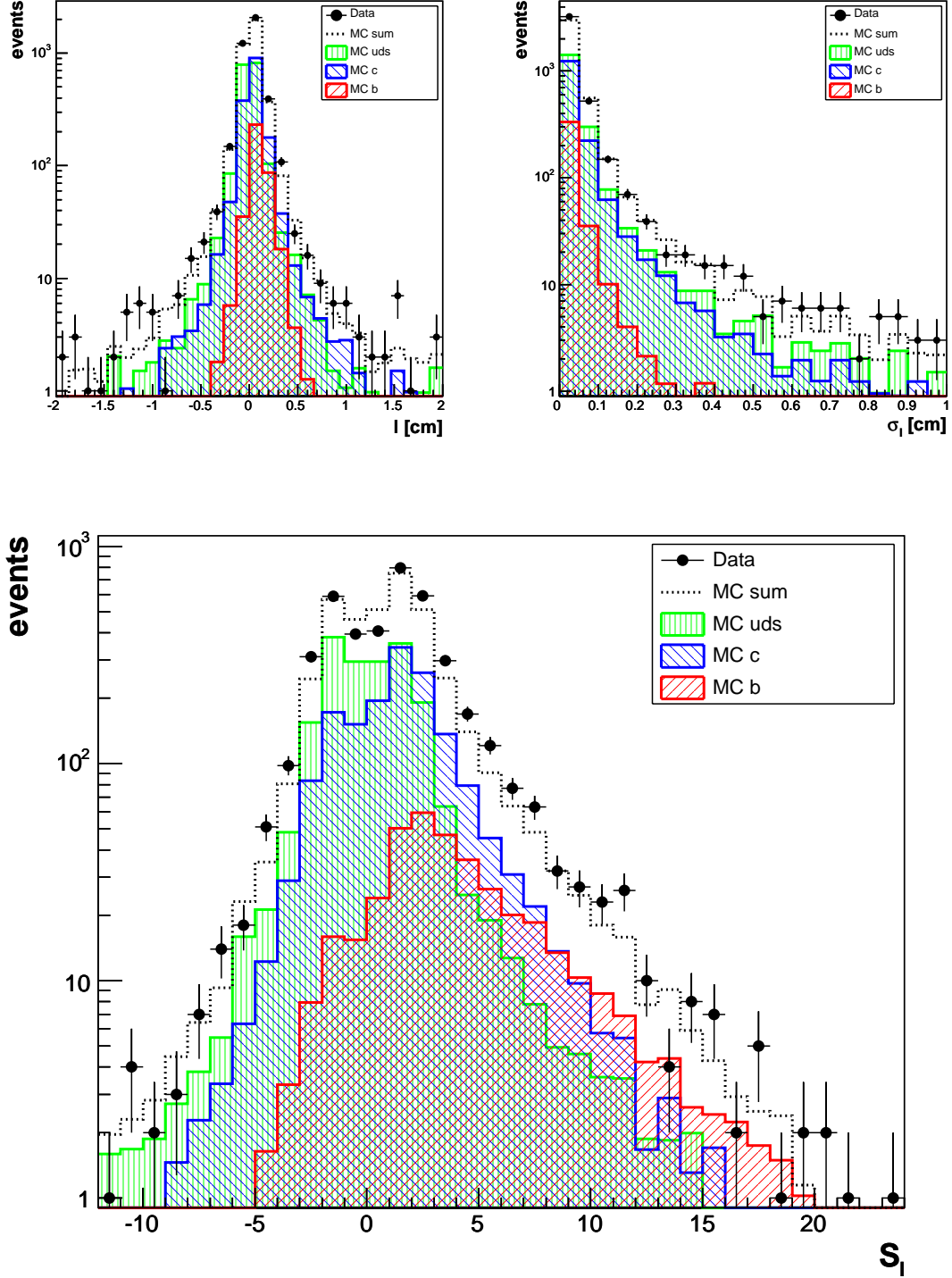


Figure 4.21: Distributions of l , σ_l and S_l of all secondary vertices with a track multiplicity of at least one track.

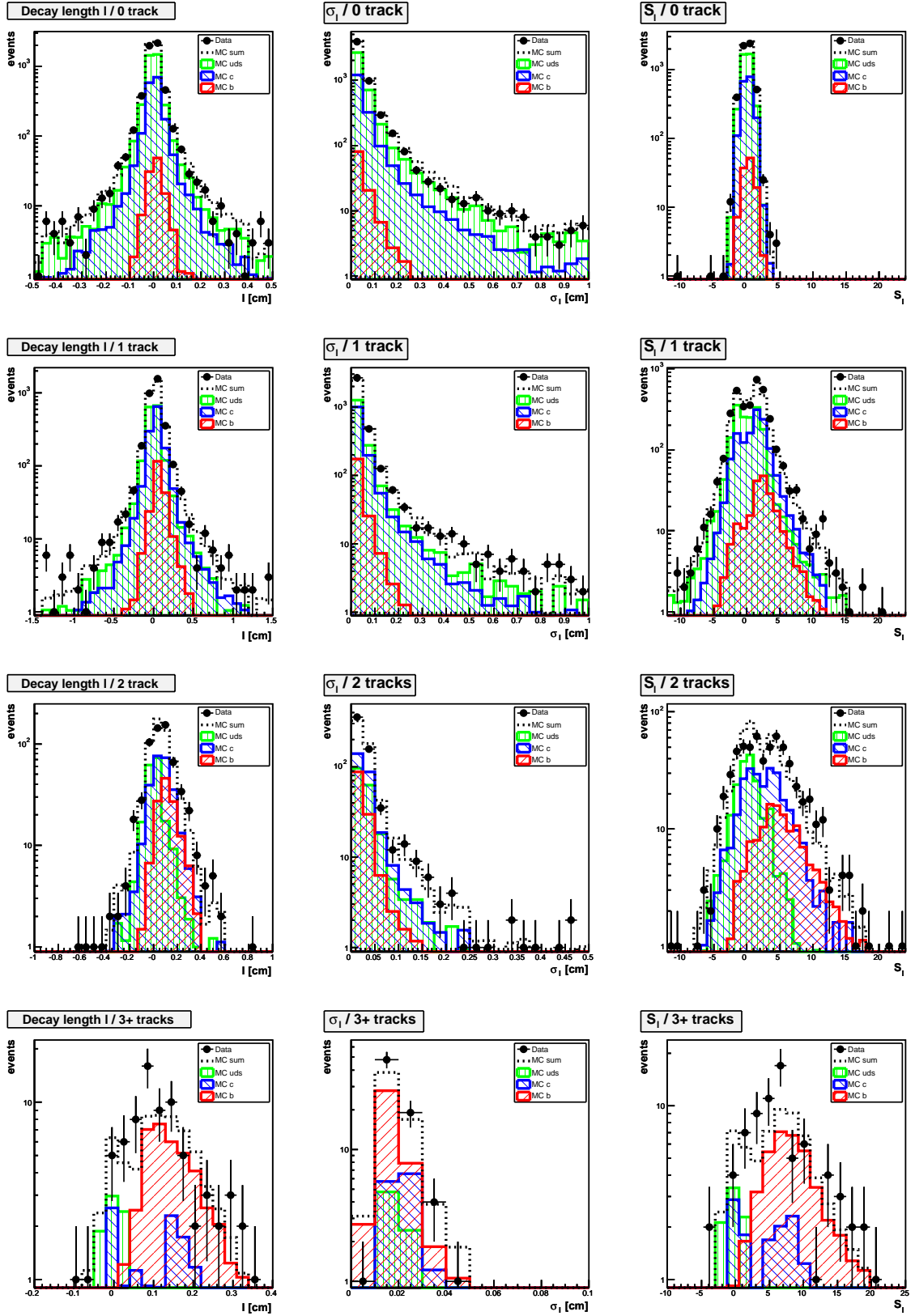


Figure 4.22: Distributions of the decay length l (left), the error of the decay length σ_l (middle) and the decay length significance S_l (right) for vertices with a multiplicity of 0, 1, 2 and 3 or more tracks (from top to bottom).

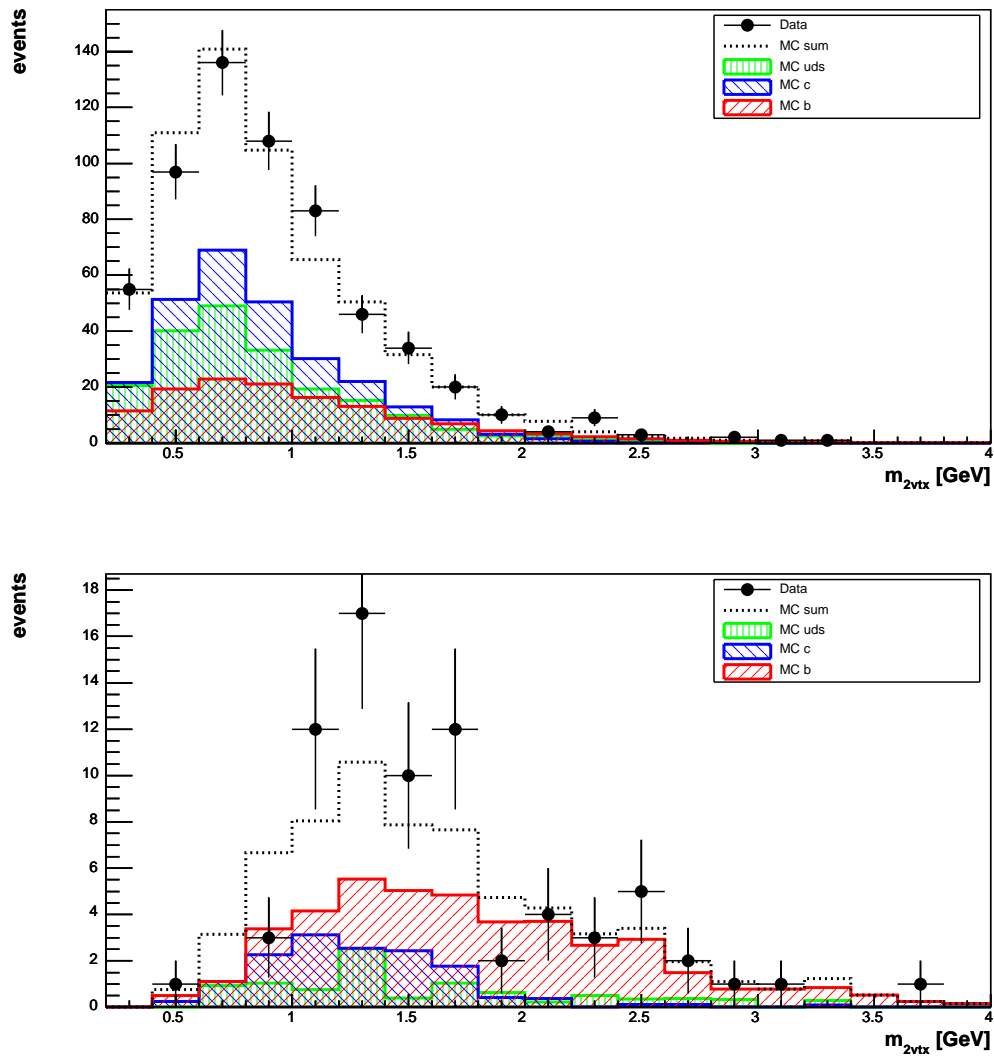


Figure 4.23: Invariant mass distribution for vertices with a track multiplicity of 2 tracks (*upper*) and 3 or more tracks (*lower*).

4.5.3 Extraction of the flavour fractions

For the extraction of the flavour fractions, three different methods are considered. For each method the distribution for uds , charm and beauty events is taken from MC simulation and is fixed. The absolute normalization of the simulated template distribution is left free and is determined in a fit (section 3.4.3) to the data distribution. With the three different methods the following distributions are considered:

Global With this method the shape of MC events for uds , charm and beauty is fitted to the S_l distribution shown in figure 4.21.

Simul23 Only vertices with a track multiplicity of 2 or more tracks are considered with this method. The decay length significance of vertices with 2 tracks is plotted in a different histogram than for vertices with 3 or more tracks. MC shapes are fitted simultaneously to both distributions.

Simul123 Similar as for the Simul23 method, the decay length significance is plotted separately depending on the track multiplicity. But in this method also vertices with one track are included in an additional histogram. Apart from the separated histograms the same data set as with method Global is used.

Investigations on stability showed that the method Simul123 is least sensitive to systematic uncertainties and also has smaller statistical errors. On this account the method Simul123 was selected to extract the flavour fractions and finally to determine also the cross section.

In figure 4.24 the result of the fit for the Simul123 method is shown on a logarithmic and a linear scale for each track multiplicity. The χ^2/ndf of the fit is 64.6/35 which corresponds to a fit probability of only 0.2%. The largest contribution to the χ^2 comes from the two bins between $0 < S_l < 5$ in the S_l distribution for vertices with a track multiplicity of 2. If these two bins are skipped, the χ^2/ndf is 49.8/33 which already corresponds to a fit probability of 3.1%. However, the information about the heavy quark contribution is mainly contained in the tails of the S_l distributions which are quite well described by the fitted MC simulation.

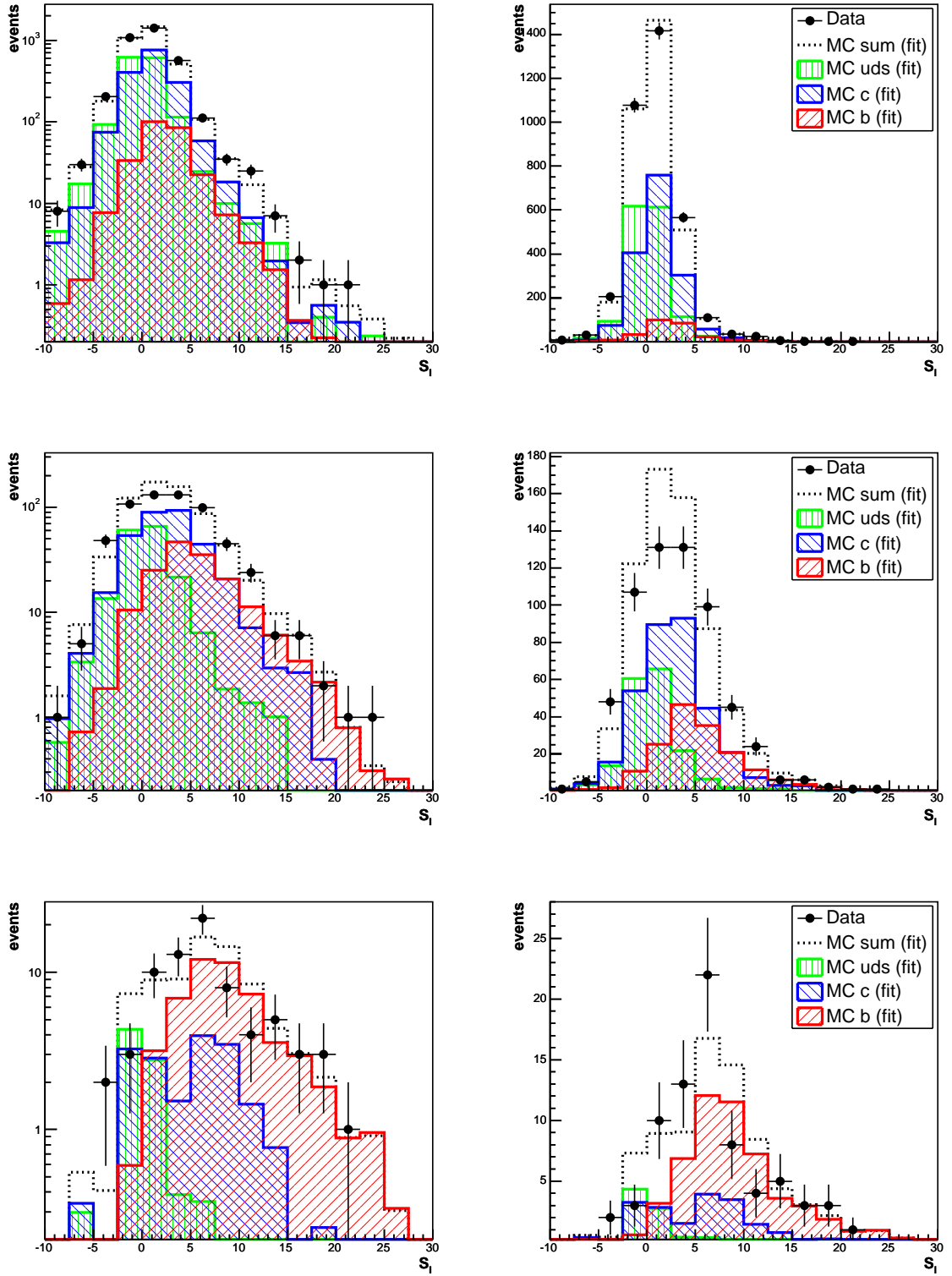


Figure 4.24: Simultaneous fit (Simul123) of vertices with a multiplicity of 1 (*top*), 2 (*middle*) and 3 or more (*bottom*) tracks on a logarithmic (*left*) and linear (*right*) scale.

Chapter 5

Results

In this chapter the measured values for the cross section are given. After a discussion of the systematic uncertainties and additional cross checks, the results are compared with the theoretical predictions and other measurements. The chapter ends with a summary and an outlook of the first part of this thesis.

5.1 Cross section for the acceptance region

The cross section for the acceptance region is extracted from the separate distributions of the decay-length significance S_l for secondary vertices with a track multiplicity of one, two and three or more charged tracks (method Simul123). The visible kinematical region of the cross section for

Virtuality	$Q^2 < 0.01 \text{ GeV}^2$
Inelasticity	$0.28 < y < 0.65$
Leading jet	$E_T > 9 \text{ GeV}, \eta_{\text{jet}} < 1$
Second jet	$E_T > 7 \text{ GeV}, \eta_{\text{jet}} < 1$

Table 5.1: Definition of the visible kinematical region for the cross section

the production of heavy quarks is defined in table 5.1 and is calculated according to

$$\sigma^{\text{vis}}(ep \rightarrow e'Q\bar{Q}X \rightarrow e'j_1j_2X') = \frac{N_Q^{\text{data}}}{\mathcal{L} \cdot \epsilon^Q}. \quad (5.1)$$

In this equation, N_Q^{data} denotes the measured number of data events with a heavy quark Q candidate and is calculated with help of the fitted fraction f_Q from the number of all measured data N^{data} events in the S_l distributions to

$$N_Q^{\text{data}} = f_Q \cdot N^{\text{data}}. \quad (5.2)$$

The efficiency and acceptance of the L1 subtrigger as well as the efficiency for finding a secondary vertex of a heavy quark Q by the vertex algorithm are absorbed in ϵ^Q .

The overall efficiency ϵ^Q for detecting a heavy quark Q is determined from the MC simulation folded with the parameterized acceptance of the electron tagger $A(y)$ according to

$$\epsilon^Q = A(y) \otimes \frac{N_Q^{\text{rec}}(Q^2, y, \text{jets}^{\text{rec}}, \text{secondary vertex, trigger elements})}{N_Q^{\text{gen}}(Q^2, y, \text{jets}^{\text{gen}})}. \quad (5.3)$$

In this equation N_Q^{gen} denotes the number of events from the MC event generator in the specified kinematical region. To apply the jet criteria to these events, jets are reconstructed on generator level based on generated stable particles. On the other hand, N_Q^{rec} denotes the number of MC

events after the simulation and reconstruction step in the same kinematical region but with a reconstructed secondary vertex. For these events also the remaining trigger elements of the subtrigger 83 are demanded in order to take into account the complete efficiency of the subtrigger 83. The average contribution of the electron tagger's acceptance to ϵ^Q is about 39%.

With this, the cross section in the visible acceptance region for charm is

$$\sigma^{\text{vis}}(ep \rightarrow e' c\bar{c}X \rightarrow e' \text{jet}_1 \text{jet}_2 X') = [452 \pm 44(\text{stat.}) \pm 109(\text{syst.})] \text{ pb} \quad (5.4)$$

and for beauty

$$\sigma^{\text{vis}}(ep \rightarrow e' b\bar{b}X \rightarrow e' \text{jet}_1 \text{jet}_2 X') = [65.1 \pm 9.1(\text{stat.}) \pm 24.2(\text{syst.})] \text{ pb}, \quad (5.5)$$

where the errors given are statistical and total systematic. The result and values from the NLO calculation are summarized in table 5.4.

An extrapolation to the cross section without jet requirement is unreliable with the all-inclusive MC simulation because heavy quarks are treated as massless in this framework. Therefore no additional extrapolation to a less restrictive kinematical region is performed.

5.2 Systematic uncertainties

The major uncertainties in the calculation of the visible cross section for charm and beauty come from the systematic uncertainty. Since the result of this analysis is not a high-precision measurement, the discussion is restricted to the main contributions of the systematic error. They are

Systematic uncertainty	δ_c [%]	δ_b [%]
Track efficiency	12	21
Track resolution	10	19
Energy scale of jets	15	7
Strangeness rejection	5	14
Fraction of resolved contributions	7	9
Energy scale electron tagger	5	13
Track multiplicities beauty	3	9
Trigger efficiency	2.5	2.5
Luminosity	1.5	1.5
Systematic error	24.2	37.2
Statistical error	9.8	13.9

Table 5.2: Summary of systematic uncertainties.

summarized in table 5.2. In this list the following contributions have been considered:

- The track reconstruction efficiency in data for tracks with $p_T > 500 \text{ MeV}$ is 97%¹. To determine the effect of this inefficiency, 3% of the tracks in MC are rejected. Since this analysis is strongly sensitive to track multiplicities in particular for beauty, this uncertainty has the largest contribution to the systematic error
- The track errors in MC can be tuned to data by increasing the multiple scattering term by a fudge factor. To see the effect of this uncertainty, the fudge factor is increased from 1.09 for the actual H1SIM version to the previous value of 1.24.
- The absolute energy scale of the LAr calorimeter is known to 4%. This uncertainty is taken into account by varying the jet cut in MC by the same value.
- To see the systematic dependence on the strangeness rejection the cut-off parameter l_c was varied by 0.2 cm.

¹This value is measured from $K^0 \rightarrow \pi^+\pi^-$ decays [57].

- Data is better described if the resolved contribution in the all-inclusive MC simulation is scaled down (see section 4.4.1). The effect of this excess is estimated by a reduction of the resolved component in the MC simulation by 25%.
- The absolute energy scale of the electron tagger is 1.5%. For MC events the same variation is applied to the generated energy of the scattered electron.
- The track multiplicity for beauty events is varied by ± 0.1 tracks in MC by reweighting MC events. This variation corresponds to a 1.6 sigma range of the beauty track multiplicity cited in [34].
- The difference between the measured trigger efficiency and the MC simulation of 2.5% is added to the systematic uncertainty.
- The luminosity is known to a relative uncertainty of 1.5%.

The systematic uncertainties are treated independently and the quadratic sum of all is taken as the total systematic error for the measured cross section.

The main contributions to the systematic error come from uncertainties of the tracking, particularly for the beauty cross section. However, this is not surprising since vertices with a track multiplicity of three or more tracks are dominated by beauty events. In addition, the reconstruction of a vertex with three tracks is quite sensitive to the assumed quality of the tracks.

On the other hand, the cross section for charm and beauty are not independent. A small systematic variation of the charm fraction can already significantly change the fraction for beauty as it can be seen in the case for the electron taggers's uncertainty of the energy scale.

5.3 Additional cross-checks

Some additional cross-checks are performed to test the stability of the result.

Since the vertical focussing of the beam in the interaction region is better than in the horizontal direction, the beam spot has an elliptical size of about $25 \mu\text{m} \times 145 \mu\text{m}$. Consequently it is a good test to split the data sample into a horizontal and a vertical sample. Data events with a secondary vertex are divided into a horizontal and a vertical set according to the direction of the corresponding jet axis. The cross section for beauty and charm is quite sensitive to this division. Another division in an upper and a lower subset shows almost no sensitivity. In this case the subsets are symmetric in relation to the beam spot. The influence on the cross section is summarized in table 5.3. The variation of the cross section under these additional cross-checks

Cross-check	δ_c [%]	δ_b [%]
Horizontal subset	-22	+19
Vertical subset	+16	-18
Upper subset	+3	-1
Lower subset	+1	-5
x_γ cut -0.05	-4	-6
x_γ cut $+0.05$	+6	+6

Table 5.3: Relative variation of the cross section under additional cross-checks.

is smaller than the systematic error. However, the separation into two sub-samples halves the statistics and the resulting cross section is more sensitive to statistical fluctuations.

The cross section is also calculated with the other methods mentioned in section 4.5.3. The results are shown in table 5.4. Within the statistical error the results of all three methods are compatible.

Method	Global	Simul23	Simul123	NLO calculation	NLO calculation with jet pedestal corrections
$\sigma^{\text{vis}}(\text{charm})$ [pb]	472 ± 50	369 ± 97	452 ± 44	386	484 - 552
ϵ^{charm}	8.4%	1.5%	8.4%		
$\sigma^{\text{vis}}(\text{beauty})$ [pb]	73 ± 12	72 ± 12	65 ± 9	56	67 - 71
ϵ^{beauty}	14.0%	6.3%	14.0%		

Table 5.4: Visible cross section and overall efficiency for different methods and the results of the NLO calculation. For the measured cross section only the statistical error is given. Since the correct treatment of jet pedestals in the NLO calculation is not clear, a range for the cross section is given (see also section 4.3.1).

5.4 Comparison with other measurements

Charm: The prediction of the NLO calculation (section 2.4) describes within the statistical and systematic error the measured value for the charm cross section. This is still valid if jet pedestals (section 4.3.1) are taken into account in the NLO calculation. In addition, the uncertainty of the NLO calculation is of the order of 30%. Within this large uncertainty, several older and recent measurements of charm show a good agreement between data and NLO calculation and therefore no deviation is expected.

However, due to the large systematic error of this analysis, the measured value for charm is not competitive with actual measurements based on exclusive charm decay channels. Nevertheless, this measurement has different systematics and can be considered complementary to those.

Beauty: Also for the beauty cross section the NLO calculation is compatible with the measured value within the statistical and systematic error, but here the situation is more interesting. Without correcting jet pedestals, the NLO calculation value is about 20% below the measurement. If jet pedestals are corrected in the NLO calculation, data and theory match quite well. It must be mentioned again that the error of the NLO calculation is of the order of 30%.

Other (semi-)inclusive measurements of the beauty cross section from H1 and ZEUS are compared to theory in figure 5.1. The other analyses are performed in a kinematical region where the influence of jet pedestals is expected to be different. Both, the analyses of ZEUS and H1 are performed for jets with $\eta_{\text{jet}} < 2.5$ and jet energies of $E_T > 6$ GeV for the DIS or $E_T^{1(2)} > 7(6)$ GeV for the photoproduction analysis. In the first H1 photoproduction measurement where a ratio data/theory larger than 3 was found, the extrapolation to the kinematical region without jet requirement was performed using a LO MC simulation.

Compared with these analyses their chosen kinematical region is wider, such that influence of jet pedestals may be large. In here, higher jet cuts are applied and therefore resolved processes with larger jet pedestals are suppressed. In addition, the analysis is restricted to the central detector region and avoids the forward direction where jet pedestals are more important.

However, this could be an indication that the effect of jet pedestals were not properly taken into account in previous analyses.

5.5 Summary and Outlook

The production of heavy quarks at HERA was studied in the kinematical regime of tagged photoproduction. The analysis is based on the finite lifetime of heavy quarks and on the fact that the track multiplicity of a charmed hadron is different than that of hadrons with beauty.

Cross section calculation: By fitting the decay-length distribution, the relative fraction of heavy quarks is extracted and from this the visible cross section is calculated. MC events are used to determine the shape of the decay-length distribution and the efficiency to measure events with

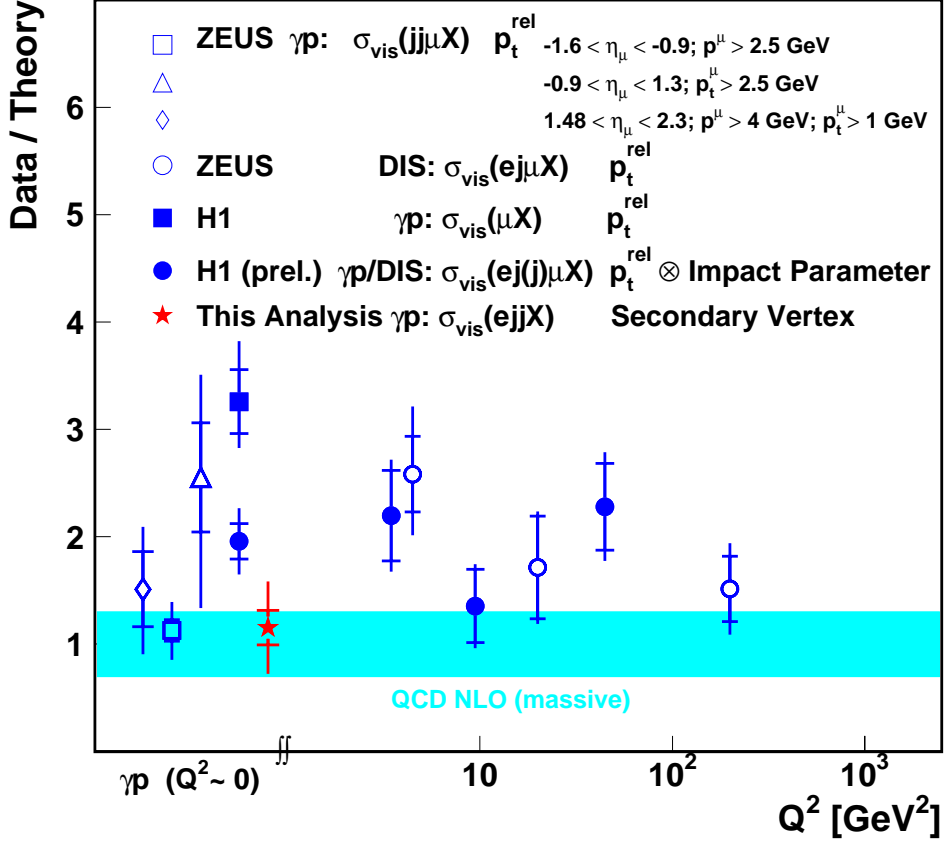


Figure 5.1: Data over theory (NLO calculation without jet pedestal correction) for the beauty cross section. Measurements are from ZEUS in photoproduction [58] and DIS [59]. Also shown are an older measurement from H1 in photoproduction [60] and recent (preliminary) results in photoproduction and DIS.

a secondary vertex. The calculation of the cross section is based on the two following assumptions concerning the MC simulation:

- The shape of the decay-length significance distribution for different quark flavours is correctly described by MC events. The crucial point for this is that tracks from the simulation have the same resolution as data. In addition, the adaptive vertex fitter is sensitive to the track multiplicity and therefore the track multiplicity for different quark flavours must be correctly reproduced by the MC generator.
- The MC simulation is reproducing correctly the kinematical distribution for events and thus can be used to determine the efficiency which allows to extrapolate from the measured kinematical range to the visible cross section.

The cross section in the visible kinematical region of $Q^2 < 0.01$ GeV, $0.28 < y < 0.65$, $E_T^{\text{Jet1}} > 9$ GeV and $E_T^{\text{Jet2}} > 7$ GeV is measured to

$$\sigma^{\text{vis}}(ep \rightarrow e'c\bar{c}X \rightarrow e'\text{jet}_1\text{jet}_2 X') = [0.452 \pm 0.044(\text{stat.}) \pm 0.109(\text{syst.})] \text{ nb} \quad (5.6)$$

for charm and

$$\sigma^{\text{vis}}(ep \rightarrow e' b \bar{b} X \rightarrow e' \text{jet}_1 \text{jet}_2 X') = [0.0651 \pm 0.0091(\text{stat.}) \pm 0.0242(\text{syst.})] \text{ nb} \quad (5.7)$$

for beauty. Within the statistical and systematic error both values are described by the NLO calculation. A still unsolved problem is the correct treatment of jet pedestals. This can substantially alter the value of the NLO prediction and thus the data to theory ratio. In this analysis the kinematical region is restricted to a range where jet pedestals are supposed to have a smaller effect than in other analyses.

A tagger for beauty events Besides the cross section measurement, this analysis indicates the potential of applying this technique for a beauty tagger. Several criteria can be combined to enrich beauty:

- Secondary vertices with a track multiplicity of 3 or more tracks,
- the invariant mass of a secondary vertex and
- the distribution of the first radial momentum M_r^1 of the jet energy distribution.

The efficiency of such a beauty tagger would suffer from a high purity requirement. However, these criteria could be applied to an untagged data sample with higher statistics as is expected for the HERA-II era after the HERA luminosity upgrade.

Part II

The L2 linking algorithm of the Fast Track Trigger FTT

Chapter 6

FTT introduction

At the end of the year 2000 the modification of the HERA storage ring started with the aim of significantly increasing the luminosity. In order to cope with the resulting higher event rate also an improvement of the H1 trigger system was necessary. The required performance can be achieved with the help of the Fast Track Trigger (FTT) which is a new extension of the existing H1 trigger system. After giving an overview of the luminosity upgrade and the trigger system, the basic concept of the FTT is explained in this chapter.

6.1 The HERA luminosity upgrade

During the years 1993-2000 the H1 detector recorded an integrated luminosity of 120 pb^{-1} which allowed some outstanding measurements like the proton structure function F_2 in various kinematical ranges [61, 62]. To extend the topics for physic analysis and to reduce the statistical error for existing measurements in close future, a perceptible increase of the luminosity is unescapable.

The instantaneous luminosity of HERA with the bunch colliding frequency ν is given by

$$L = \frac{N_e \cdot N_p \cdot \nu}{2\pi \cdot \sigma_e^2 \cdot \sigma_p^2} \quad (6.1)$$

with N_x the number of particles per bunch and σ_x the cross section at the interaction point. As can be seen in equation (6.1), a larger luminosity can be achieved by increasing the number of particles per bunch or by decreasing the cross section. A clear raise of the beam currents would have been only possible with a significant modification of the accelerator. Therefore the improvement of the focussing of the particle beams in the interaction region was preferred [63].

Two superconducting magnets for a stronger focussing of the beams were added to the beam pipe in the detector region. They are roughly in-plane with the muon endcaps. As a consequence of the different beam geometry the beam pipe had to be changed from a circular to an elliptic profile and new collimators were necessary to shield the detector from synchrotron radiation.

This upgrade from HERA to HERA-II was realized during a long shutdown from September 2000 until July 2002. With the new configuration an increase of specific luminosity of about a factor of 4.5 was realized and this opens the door to collect an integrated luminosity of $\sim 1 \text{ fb}^{-1}$ within the next years.

The long shutdown was also a good opportunity to upgrade parts of the H1 detector. The silicon strip detectors CST and BST were adapted to the new geometry of the beam pipe and were supplemented by a forward silicon tracker (FST). Parts of the forward tracker (FTD) were modified and renewed. The inner proportional and z -chambers CIP and CIZ were replaced by a new proportional chamber (CIP2k) which now provides the z -vertex trigger information [64, 65]. The backward proportional chamber (BPC) in front of the SpaCal was replaced by a new one which is suitable for the new beam pipe. Also modifications of the electromagnetic and hadronic

SpaCal were necessary due to the changed beam pipe. And finally, as already mentioned above, the capability of the trigger was extended by the FTT – the subject of this part of my thesis.

6.2 The H1 trigger system

In the HERA storage ring the bunch crossing frequency between electrons and protons is 10.4 MHz. Although some of the bunches are empty only a small fraction of registered events with a typical data size of 1 Mbyte can be stored permanently. Also after the HERA-II upgrade the read-out capacity of the storage device is limited to about 10 Hz. The task of the trigger system is to select with high efficiency in respect to the physical interest one event out of about 10^6 events registered by the H1 detector. The H1 trigger is realized as a four level system and is outlined in figure 6.1.

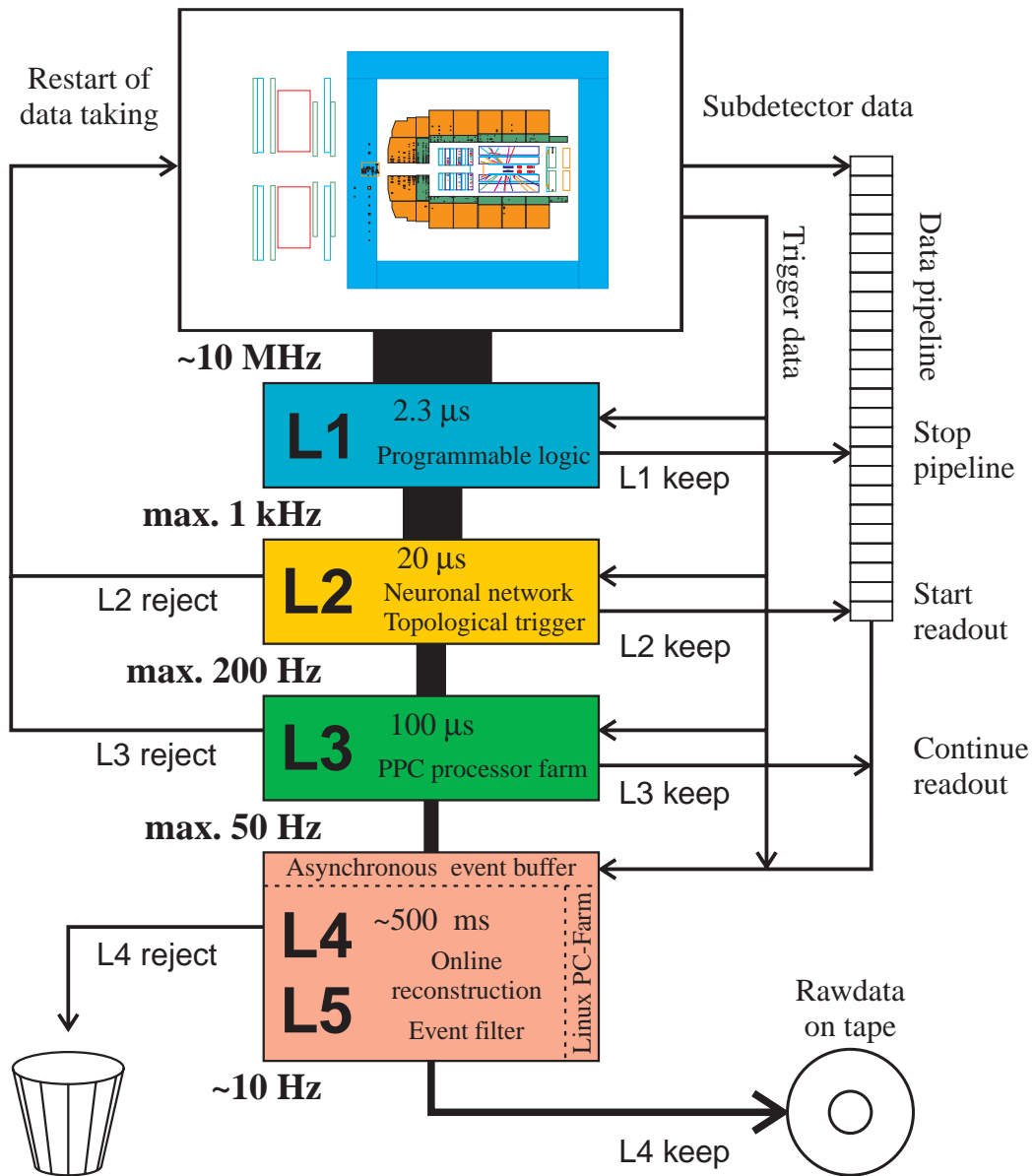


Figure 6.1: The multi-level trigger system of H1

6.2.1 Dead-time free Level 1

At each bunch crossing dedicated sub-detectors send so called trigger elements (TEs) to the Central Trigger Logic (CTL). Up to 256 TE can be processed by the CTL. These TEs are based on topological, energetic, or timing information from these sub-detectors and are logically combined in the CTL to 128 subtrigger bits. The level 1 trigger (L1) decision is based on these subtrigger bits by setting the L1keep flag if one or more subtrigger bits have a positive entry. The L1 decision must be available within $2.3\ \mu\text{s}$ after bunch crossing. During this time the whole detector information is stored in a data pipeline of a depth of 24. The pipelining of the data makes the L1 trigger free of dead-time. With the L1keep signal the pipeline is stopped, dead-time starts to accumulate, and the trigger decision is taken over by level 2.

Some subtrigger bits have a constant high rate, other subtrigger bits are sensitive to the quality of the electron and proton beam. Therefore prescale factors for each subtrigger are foreseen. Prescale factors allow a rate reduction according to a programmable scheme by accepting only every n -th event. The prescale factors are calculated automatically and are largely optimized by requiring a maximal L1 trigger rate of 1 kHz.

6.2.2 Starting readout at Level 2

A decision time of $20\ \mu\text{s}$ for the level 2 trigger (L2) allows the use of more complex systems and the combination of different sub-detector information. The L2 trigger consists of two independent systems:

- the Neuronal Network trigger (L2NN)
- the Topological Trigger (L2TT).

Each system provides a 16 bit word which is used to validate the 128 subtrigger bits from L1. A positive validation results in a L2keep signal and starts the readout of the whole detector which takes about 1 ms. In case of a L2reject the data pipeline is cleared and data taking is restarted.

Since the bulk of data reduction is already performed on the dead-time free L1 trigger, the dead time on L2 is only 2%. The L2 trigger reduces the L1 trigger rate by an additional factor of 5.

6.2.3 Abort readout on Level 3

Although a level 3 trigger (L3) was foreseen from the beginning on of H1 [66] it has never been operating during the HERA-I phase. The reason for this was that the processors available at the end of the eighties with a frequency of 25 MHz didn't have the required computing performance for the complex trigger decisions.

The L3 system was planned to reject mainly background events. A L3reject signal is generated if the L3 found a negative trigger decision and the readout of data is stopped immediately. Although the L3reject signal is not required to be set at a fixed time, a significant reduction of dead time can only be achieved if the signal is generated in less than $100\ \mu\text{s}$.

For HERA-II the old L3 system will be completely replaced by the FTT level 3 trigger. This systems can search for up to 16 independent decay topologies and generates the trigger decision analogous to the L2 system by validating the trigger bits from the previous step [67]. With this setup the L3 system is reducing the data rate to 50 Hz by accumulating a dead-time of about 5% for a complete detector readout.

6.2.4 Event filtering and online reconstruction at Level 4 & 5

Data from an event that survived the first three trigger levels are transferred to the event builder where the event is fully reconstructed. During the HERA-I period this task was split into two steps. On trigger level 4 (L4) only a temporary reconstruction of the event was possible because

only rough calibration information of the subdetectors was available. The final reconstruction with the full calibration information was performed on level 5 (L5) with a temporal delay.

Due to a new calibration scheme these two steps could be merged for HERA-II and are now called L45. Now the events are reconstructed on a commercial Linux PC-farm which takes about 500 ms per event. During the reconstruction the event is classified into physical classes. Events which are not classified (in general soft physics) are rejected according to a fixed downscale scheme. Accepted events are passed to the data logging system which permanently stores the event data on tape.

6.3 Concept of the FTT

As described in section 6.1 the specific luminosity is increased by about a factor of 4.5 after the HERA-II upgrade. Without a modification of the trigger system only events in deep inelastic scattering (high Q^2) can be measured efficiently after the upgrade. As can be seen in table 6.1, data with lower Q^2 (small x region) are required to be downscaled by an additional factor of 5 so that finally the whole benefit of the higher statistics from the upgrade is lost.

Q^2	HERA	HERA II
5	5	25
40	2	10
150	1	1

Table 6.1: Expected level 1 prescale factors before and after the luminosity upgrade without trigger modification [68].

In order to improve the situation, a new trigger based on track information from the CJC was built. With the Fast Track Trigger (FTT) an online analysis of the hadronic final state is possible and prescale factors can be avoided. The FTT is integrated in the multi-level trigger system of H1 and provides trigger decisions to the first three trigger levels with the best possible track information from the CJC [69].

During the latency of the first trigger level the FTT searches for hits from selected CJC wires and combines them to track segments. A coarse linking of these segments to tracks allows a L1 trigger decision based on them. A much more precise track reconstruction is performed on trigger level 2 within $20 \mu s$. The resolution of those tracks is nearly as good as the offline reconstruction. This information is used to generate a L2 trigger decision. Finally this well measured three dimensional track parameters are used on trigger level 3 to search for particle decays [70]. The diverse tasks of the FTT which are performed at different trigger levels are summarized in table 6.2.

	FTT L1	FTT L2	FTT L3
Latency	$2.3 \mu s$	$20 \mu s$	$\sim 100 \mu s$
Tasks	Hit finding	Linking of tracks	Event reconstruction
	Track segment finding	Fit of track parameters	Event analysis
	Coarse linking		
Trigger decision based on	p_T thresholds	Full track information	Invariant mass
	Multiplicities		Topologies
	Charges		
Applied technologies	Programmable logic device	Programmable logic device	Processor farm
	Fast pattern recognition	Digital signal processing	Real-time OS

Table 6.2: Tasks, trigger decision, and technology on the three FTT trigger levels.

6.3.1 Track segment finding on level 1

A subset of CJC1 and CJC2 wires are used as input for the FTT. These wires are grouped into four *trigger layers* with 3 *wire layers* each. The first three trigger layers originate from CJC1 while trigger layer 4 is built from CJC2 wires. In figure 6.2 the three wire layers of each trigger layer are marked. In addition a *trigger group* is defined as a group of CJC wires from one CJC cell and

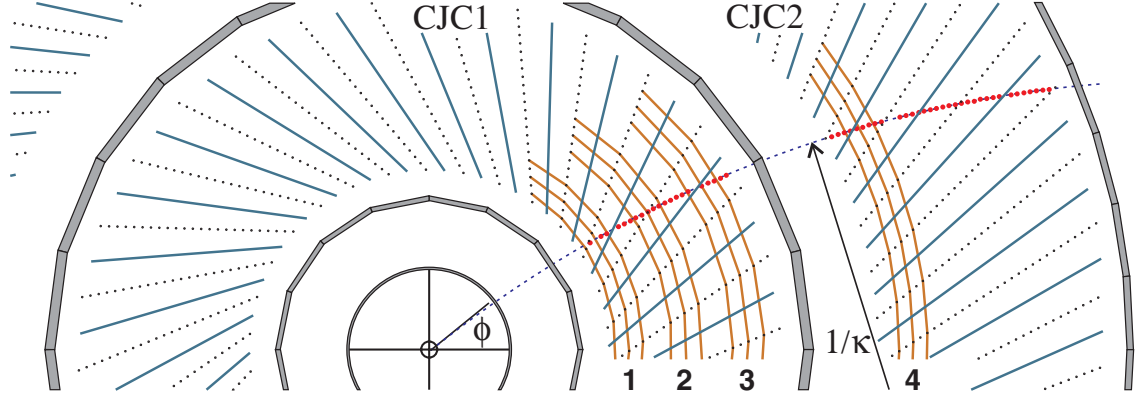


Figure 6.2: The CJC1/CJC2 in the r - ϕ plane showing the four trigger layers. Track hits of a track crossing the CJs are marked along the path. κ and ϕ are the track parameters defined in section 1.4.

one trigger layer. Consequently, a trigger group consists of 3 wires. Table 6.3 lists the wire layers which are used to build the different trigger layers.

Trigger layer	Jet chamber	Wire layers	Average radius	# Trigger groups
1	CJC1	3, 5, 7	25.1 cm	30
2	CJC1	10, 12, 14	31.3 cm	30
3	CJC1	18, 20, 22	38.7 cm	30
4	CJC2	4, 5, 8	58.7 cm	60

Table 6.3: Subset of CJC wires used as input for the FTT.

In a first step FADCs¹ are digitizing the CJC signals from the selected wires at 80 MHz. A Qt -algorithm[69] provides the drift time t_{drift} for a particle hit and the integrated charge Q . Since the charge is measured on both ends of the wire also information on the z position for each wire can be extracted by using equation (6.2) where Q^+ (Q^-) is the charge measured at the $+z$ ($-z$) end of the wire with length l_{wire} .

$$z = \frac{l_{\text{wire}}}{2} \cdot \frac{Q^+ - Q^-}{Q^+ + Q^-} \quad (6.2)$$

The measured z -resolution of a single hit from cosmic muons is $\sigma_z = 7.5$ cm [71].

Hits found by the Qt -algorithm are written into shift registers. Characteristic patterns emerge in the shift registers which can be compared with valid masks within trigger groups [72]. A valid mask is defined by a track originating from the primary vertex and a minimal transverse momentum p_T . Since a validation mask is stored together with its original κ and ϕ value, this two track parameter can be used to describe the valid track segment. In a first step the track segment validation is performed at 20 MHz with a coarse resolution. This provides the track segment parameters for the L1 linker. About 3'000 masks for each trigger layer are required. After a L1 keep the track segment parameters are refined with the full resolution at 80 MHz. This is required for the higher trigger levels in order to get the required precision. Up to 90'000 different masks

¹Flash analog to digital converter

per trigger layer are needed to get the full resolution. Apart from the timing requirement this already imposes a sophisticated demand for the required hardware [73].

6.3.2 Track segment linking and fitting on level 2

After finding track segments on L1 these segments are linked to tracks on L2. Track segments from trigger layer l are characterized in the r - ϕ plane by a curvature $\kappa_{\text{seg}}^l = \frac{1}{r_{\text{seg}}^l}$ and the azimuthal angle ϕ_{seg}^l at the vertex. Segments originating from the same track but different trigger layers have approximately the same parameters $\kappa_{\text{track}} \approx \kappa_{\text{seg}}^l$ and $\phi_{\text{track}} \approx \phi_{\text{seg}}^l$ with $l = 1, 2, 3, 4$. The linking algorithm makes use of this property by looking for clusters in a 2 dimensional histogram in the κ - ϕ plane where all track segments ($\kappa_{\text{seg}}^l, \phi_{\text{seg}}^l$) are plotted. More details of the linking algorithm are given in chapter 8. The L1 linking algorithm mentioned in the previous section operates according to the same concept but with a κ - ϕ histogram which has a much lower resolution. In order to improve the resolution of the track parameters of linked segments, the track segments are fitted to tracks. The track fit is performed in two steps. First a non-iterative helix fit is performed in the r - ϕ plane [74]. This Algorithm [75] uses the least square method to determine the three track parameters κ , ϕ , and d_{ca} as defined in section 1.4. In the second step a fit in the r - z plane provides the parameter θ of the track. In addition to this information the knowledge of the primary collision's z -coordination is necessary. This z -vertex information either can be received from the CIP2k or can be calculated within the FTT itself from a number of tracks [76]. The second method is preferred in order to be independent of other detector components and to have a consistent result.

Compared to the complete H1 track reconstruction the resolution of the FTT at L2 is $\sigma(1/p_T) = 0.02 \text{ GeV}^{-1}$ and $\sigma(\phi) = 1.2 \text{ mrad}$. These well measured tracks can now be used to build a track based L2 trigger decision.

6.3.3 Search for particle resonances on level 3

Starting with the precise track parameters from L2 the primary task of the L3 system is to identify particle decays with the help of invariant masses. A reconstruction processor board for each specific decay channel is foreseen which provides one TE for the CTL. Because the selection algorithm can be programmed in a high-level programming language like *C*, every potential L3 user should be able to write or adapt a particular selection code without profound hardware knowledge.

The method of invariant mass is based on the reconstruction of invariant masses for all combinations of charged tracks and a cut around the expected resonance mass considered rejecting wrong combinations. It is obvious that due to narrower cuts a higher selection purity is reached with more precisely measured tracks.

Chapter 7

Hardware for the FTT

In the previous chapter the concept of and the functional demands on the FTT were outlined. This chapter now treats the technical aspect of the FTT and its hardware implementation. The main focus is put on the hardware for L2 which is important in the next chapter.

One of the main goals of the FTT is to have at L3 an online trigger decision based on invariant masses with help of precisely reconstructed tracks. During the era before the FTT, such a trigger decision was only available offline at L4. It is clear from this stringent timing condition that special demands on the hardware are required and that most parts of the hardware had to be developed first.

The layout of the FTT hardware can be separated into three parts corresponding to the three trigger layers as shown in figure 7.1 and consists in total of more than 60 electronic boards and 150 buffer cards. Each component fits into one of six double height (6U) VME crates located in the H1 electronic trailer. Besides the power supply and cooling by ventilators these crates are equipped on the backside with a backplane which is used for read out, slow control, and communication between different components. For the L3 system a standard VME create with two backplane connectors per card is used whereas for the L1 and L2 system only the upper connector of the backplane is assigned according to the VME standard while the lower connector has a custom assignment. A VIC-8250 card is used in each of the 6 crates to connect the VME bus within the FTT system over a VMV data bus. Additionally there is a Power PC card in each create which is used for read out, configuration and steering of the whole system over an ordinary TCP/IP connection.

The main communication between the L1 and L2 components of the FTT is achieved by LVDS¹ connections which have a maximal data bandwidth per cable of 5.0 Gbit/s. The LVDS channel link offers some advantages over standard optical connections. Not only are the transmitting and receiving components less expensive but also the LVDS cables are cheaper than optical fibres. In addition the FTT system requires nearly the full data bandwidth given above which could only be reached by several optical fibres. And finally the mechanical robustness of a LVDS cable is better than for an optical fibre. On the other hand an optical connection electrically decouples transmitter and receiver while a LVDS connection offers the potential problem of "ground loops" and their components have a sensitivity to electrical noise.

7.1 Hardware for trigger level 1

Buffer cards In a first step a subset of analogue signals from the CJC1 and CJC2 must be tapped from the existing FADC cards of the jet chambers without affecting the existing system. For this reason a *buffer card* was developed which allows a simultaneous supply of the old $DCr\phi$ trigger and the FTT system with CJC signals. No further functionality of this card is required.

¹Low voltage differential signal

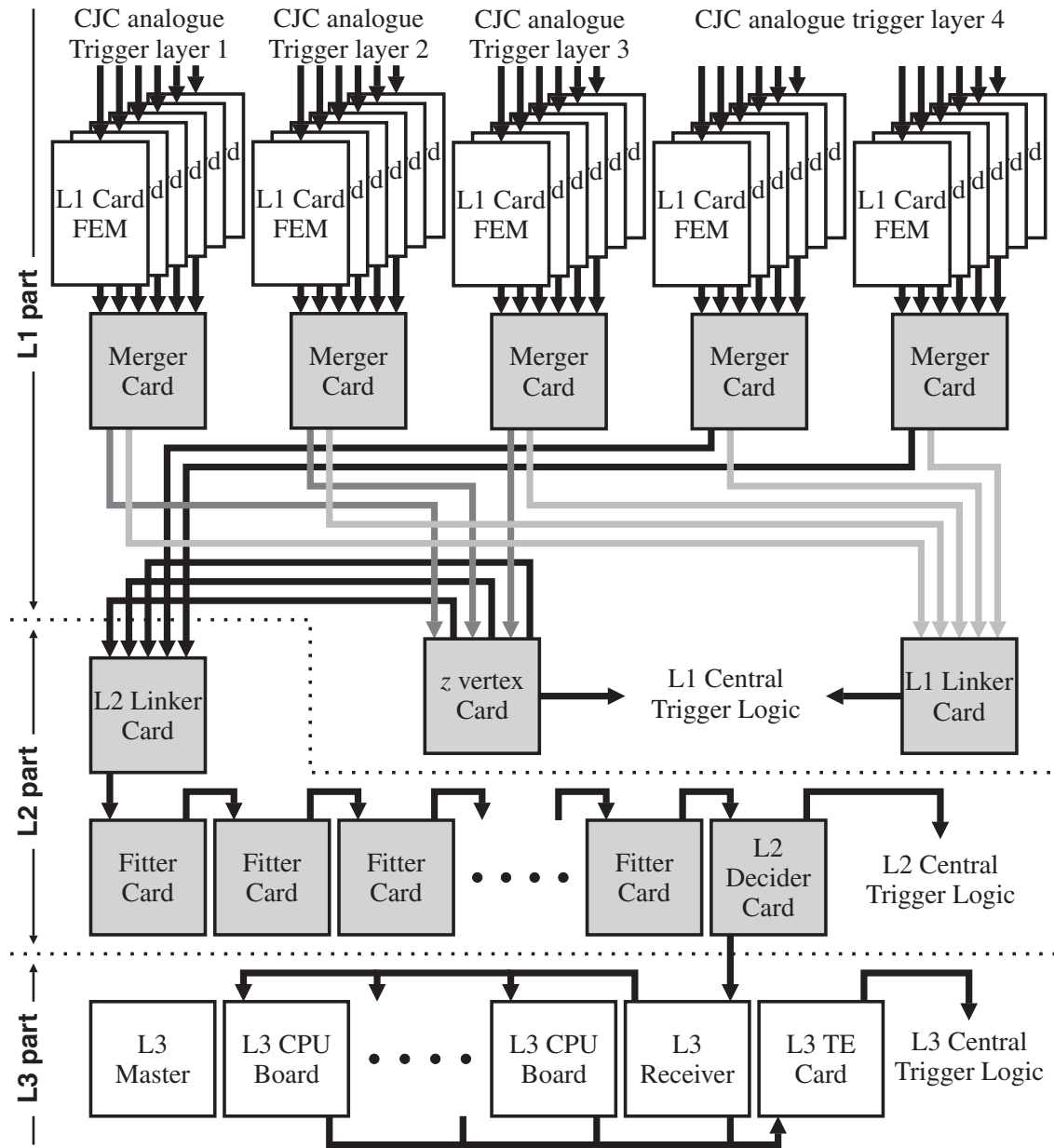


Figure 7.1: Overview of the hardware implementation of the FTT. The multifunctional processing board (shaded board) is used for several tasks.

One buffer card can tap analogue signals of one trigger group (3 CJC wires) so that a total of 150 buffer cards are needed.

Front End Modules Analogue signals from the buffer cards are sent to the Front End Modules (FEMs) which are the main components of the L1 system. CJC signals from 5 trigger groups are collected and processed by one FEM. A schematic overview of the FEM is given in figure 7.2. 15 FADCs² with two input channels are digitizing the analogue CJC signals with a frequency of 80 MHz and a resolution of 10 bit. In order to extract the z information of a CJC hit both ends of the wire are digitized.

²Analog Devices AD9218-80

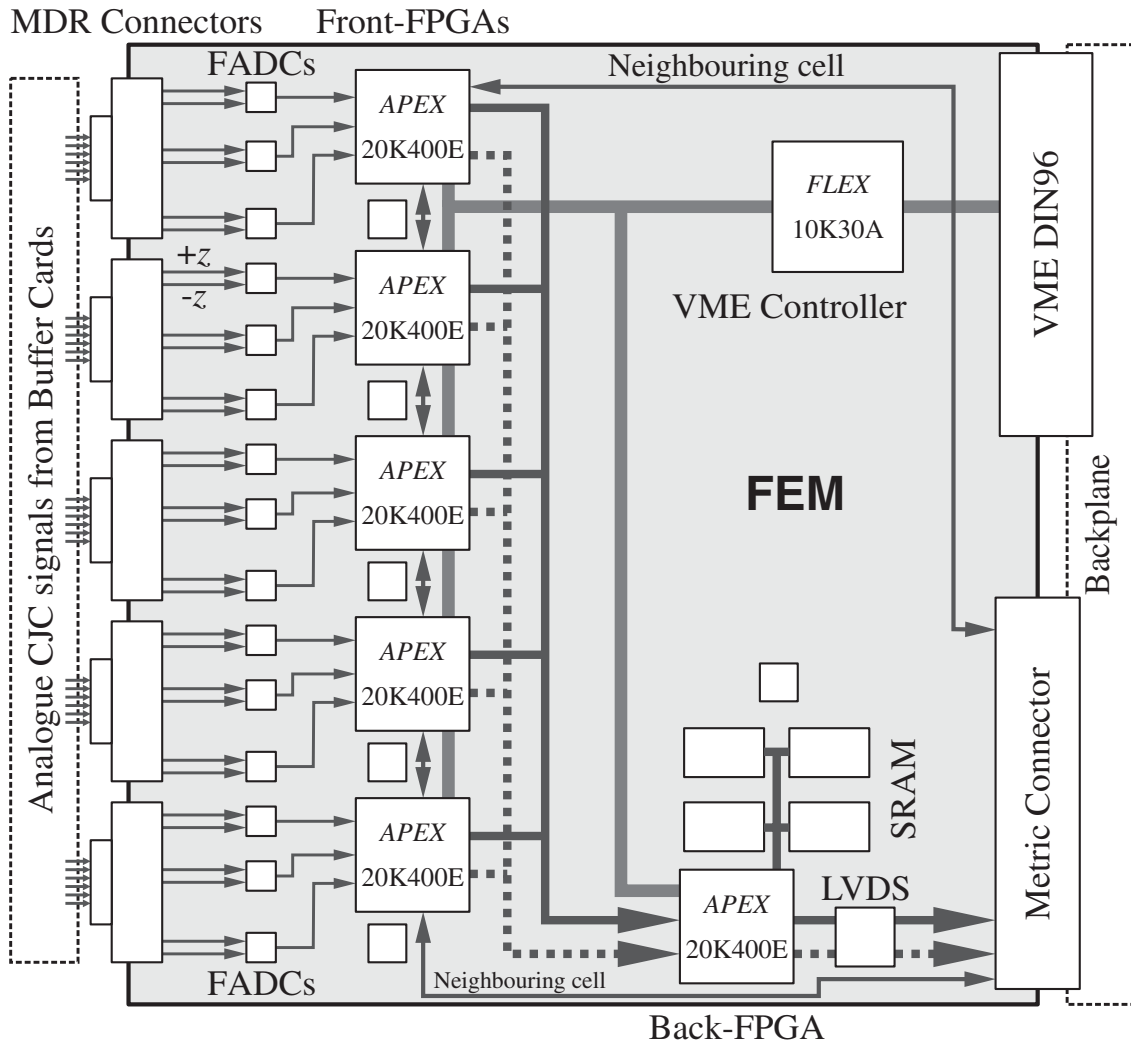


Figure 7.2: Device placement on a FEM

The main component of the FEM are so called FPGAs³, large programmable logic devices (PLDs). Each of the five Front-FPGAs⁴ perform the Qt -algorithm and a coarse track segment finding at 20 MHz for one trigger group. The two algorithms are fully pipelined so that a deadtime free L1 trigger operation is possible. Therefore the track segment finding algorithm must compare the CJC hit pattern with all valid masks within one bunch crossing. This is only possible due to the use of CAMs⁵ which can be implemented directly in the Front-FPGAs. More details on the CAM technology can be found in subsection 7.4. The entry in a CAM provides also the track parameters (κ, ϕ) which are sent immediately to the LVDS port for the L1 linker and the z -vertex card.

After a L1keep signal, the refinement of the track segments at 80 MHz is performed in the Front-FPGA. The refined segments are sent to the Back-FPGA⁶ for looking up the corresponding track segment parameters. Due to the large number of masks, additional external RAMs are required therefore. After finding the corresponding track segment parameters, they are passed to the LVDS transmitter for FTT L2.

³Field programmable gate array

⁴Altera APEX 20K400

⁵Content addressable memories

⁶Altera APEX 20K400

Merger Card, L1 Linker Card and z vertex card Although these cards perform different tasks they use the identical hardware as on L2. The technical description of this card is given in the next section.

The merger card collects all track segments sent by LVDS from the six FEMs and merge them into one single LVDS channel. Although this task seems to be quiet simple a sophisticated implementation was inevitable. The merger cards have to operate in the L1 or L2 mode. In the first mode track segments are sent to the L1 linker and the z -vertex card under very stringent timing conditions. In the second mode they are sent to the L2 linker using other LVDS channels.

For the L1 linker card the timing constraints are even more restrictive. The card collects all track segments from the merger cards and tries to link segments from different trigger layers to one track. The principle of the algorithm is the same as described in 8.1.2 for the L2 linker but with a much smaller κ - ϕ histogram with 16×60 bins. The L1 linker can provide various TEs based on track numbers, p_T -thresholds and topologies.

Studies [76] showed that it is even possible to build a z -vertex trigger decision with coarse measured track segments from CJC1 within $2.2 \mu\text{s}$. The algorithm extrapolates all possible combinations of z -hits from track segments to the beam axis. If an accumulation of combinations is found within the ep -interaction region, a trigger signal is generated. This solution is now implemented on an additional trigger board which is a simple and cheap addition to the CIP2k z -vertex trigger.

The time requirement for the different tasks on level 1 is summarized in table 7.1.

Step	Process	time [μs]	cumulated [μs]
1.	Ionisation and drift	1.056	1.056
2.	Analog cable delay	0.180	1.236
3.	FEM: FADCs	0.060	1.296
4.	FEM: hit finding	0.036	1.332
5.	FEM: segment finding	0.096	1.428
6.	FEM: collection of trigger bits	0.086	1.514
7.	Channel Link: FEM \rightarrow Merger	0.070	1.584
8.	Merger: Merging	0.086	1.671
9.	Channel Link: Merger \rightarrow Linker	0.060	1.731
10.	Linker: receiving & sorting input	0.077	1.808
11.	Linker: linking	0.048	1.856
12.	Linker: pipelining	0.096	1.952
13.	Linker: trigger decision + driver	0.067	2.019
14.	TE transmission FTT-CTL	0.048	2.067

Table 7.1: Time budget at level 1 of FTT.

7.2 Hardware for trigger level 2

For the various tasks on L2 a *Multifunctional Processor Board* (MPB) was developed in collaboration with Supercomputing Systems AG (SCS) from Zurich [77]. The MPB is equipped with four digital signal processors (DSPs) and two FPGAs and is therefore capable to be configured for different tasks. In addition the MPB can be equipped with up to four LVDS transceiver cards (so-called *piggyback* cards) and can thus cope with a large data input and output rate. As already mentioned above, the MBP is not only used for L2 but also for several tasks on L1 due to its flexibility. The possible configurations are listed in table 7.2 The multiple use of the same board design considerably reduces development and production costs.

Simulations have shown that the limitation to the reconstruction of 48 tracks per event is fully sufficient for 98% of all events of interest. Since each DSP can process two track fits during the L2 time a total of six fitter cards is required. The fitter cards are arranged in a daisy chain. This

Function	Input	Output	Key technology
Merger card	Track segments	Track segments	Multiple LVDS channels
L1 linker card	Coarse track segments	L1 TEs	FPGA
z -vertex trigger card	Coarse track segments	L1 TEs	FPGA
L2 linker card	Refined track segments	Linked tracks	FPGA
Fitter card	Linked tracks	Fitted tracks	DSP
L2 decision card	Fitted tracks	L2 TEs	FPGA, DSP

Table 7.2: Possible configuration of the MPB

helps to keep the system simple because the order of data fragments cannot get mixed-up. The additional latency of the daisy chain of about $0.5\ \mu\text{s}$ is only 2.5% of the L2 decision time.

7.2.1 Multifunctional processor board

The core of the MPB is formed by the four DSPs and a large FPGA called *data controller* as can be seen in figure 7.3. The placement of the devices is shown in figure 7.4. Mathematical algorithms which require arithmetical operations like track fitting run on DSPs while the data controller is predestinated for associative and complex logic like the linking of track segments.

The four floating-point DSPs⁷ are running at a frequency of 166 MHz and are equipped with an internal program memory of 64 kB and an internal data memory of the same size. To extend the internal data memory for memory intensive applications, an external SRAM of 512 kB is connected to the 32 bit wide memory interface of each DSP. Since the DSPs have a poor support for multi-processor busses, each of them is also connected to an additional FPGA⁸ by the same memory interface. Because this FPGA controls the memory bus of each DSP it is called *DSP controller*. In addition the DSP controller is responsible for the data distribution among the four DSPs within the shortest possible time.

The memory bus of each DSP can be connected to a dual-ported RAM (DPRAM) by bus switches. This is required at startup of the system where the DSP code is loaded via the VME interface into the DPRAM, from which each DSP can download its own program code. For each DSP two switches are required. One for toggling the 32 bit wide data bus and an other for switching the 16 address bits and some additional control bits. Since a DPRAM has a data width of only 16 bits, the upper half-word and lower half-word are stored into separate DPRAMs.

The DSP controller is connected to the *data controller* FPGA by a 48 bit wide data bus which is connected to each of up to four piggyback connectors of same data bus width. Consequently, the data controller must handle a lot of data lines simultaneously. On the other hand this high rate of data throughput in combination with a full programmable logic allows the implementation of fast and complex algorithms in this device. Besides the 48 bit wide data bus the FPGAs are also connected by a number of control lines. Their functionality is not assigned in a fixed manner and depends on the MPB configuration.

A third FPGA⁹ (*VME interface*) is used to connect the VME bus of the backplane to the local bus. Data controller, DSP controller and DPRAM interface are also connected to this 16 bit wide bus. The local bus is mainly used for slow control and read out. In addition to the VME access the backplane provides also other trigger relevant signals like the $Lx\text{keep}$ / $Lx\text{reject}$ signal and the trigger elements.

Clocking The main clock frequency of the MPB is 104 MHz. Like all other frequencies, this frequency is also derived from the HERA bunch crossing frequency of 10.4 MHz. There are some strong arguments for this clock frequency. The maximal possible LVDS clock frequency of about 110 MHz is only marginally higher than the base clock frequency of the MPB. According to this

⁷Texas Instruments TM320C6701

⁸Altera APEX 20K200E

⁹Altera FLEX EPF10K30A

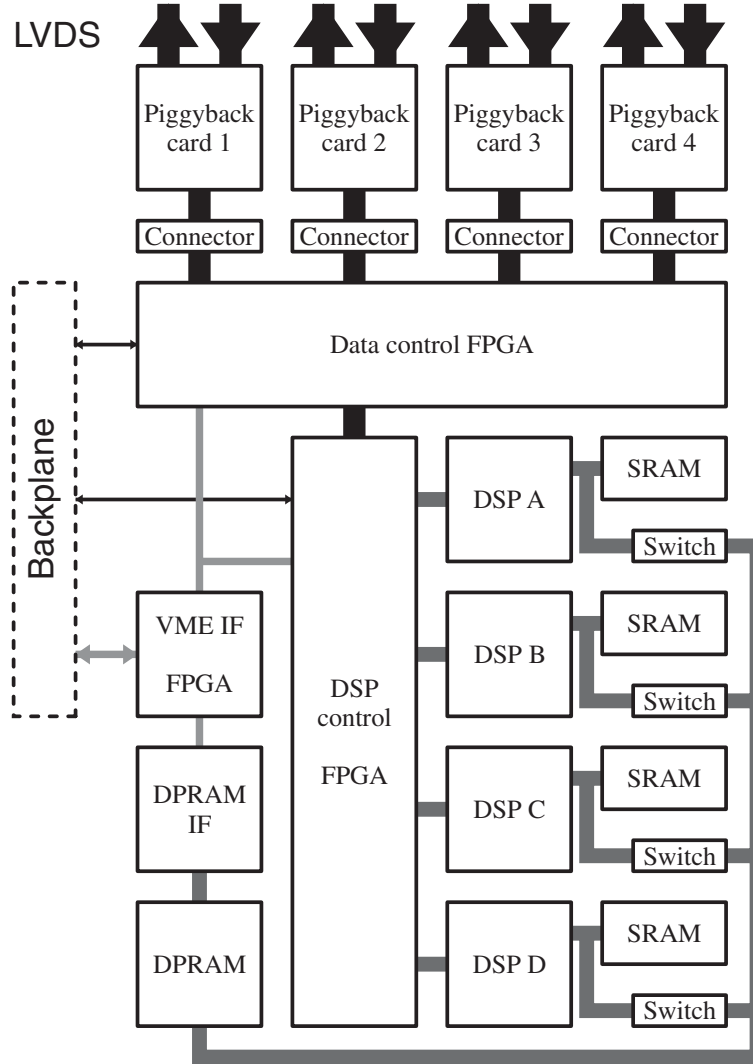


Figure 7.3: Functional block diagram of the MPB with four connected piggybacks.

the LVDS transmitter can be operated without an additional synchronization step. On the other hand a FPGA's logical algorithm with a medium complexity can't run significantly faster than 100 MHz. And finally the clock setup time¹⁰ (t_{su}) as well as the clock to output time¹¹ (t_{co}) of several devices are in the order of 3 ns. A synchronous design running at a frequency $\nu = 1/t_{clock}$ is only possible if the following equation is valid for each signal between two devices i and j with path length l_{path}^{ij} :

$$t_{co}^i + t_{su}^j + t_{delay}^{ij} + t_{spare} = t_{co}^i + t_{su}^j + \frac{3}{2} \frac{l_{path}^{ij}}{c} + t_{spare} \leq \frac{1}{\nu} = t_{clock} \quad (7.1)$$

In equation (7.1) the signal propagation delay t_{delay} between two devices i and j is approximated with the empirical value of $l_{path}^{ij}/\frac{2}{3}c$. In the layout of the MPB the longest signal path between piggyback and data controller has a length of 25 cm. With equation (7.1) the resulting spare time t_{spare} per clock cycle is smaller than 2.4 ns.

¹⁰The clock setup time t_{su} is the time interval for which a data signal must be present at an input pin before the clock signal.

¹¹The clock to output time t_{co} is the time required to obtain a valid output signal at an output pin that is fed by a register after a clock signal transition on an input pin that clocks the register.

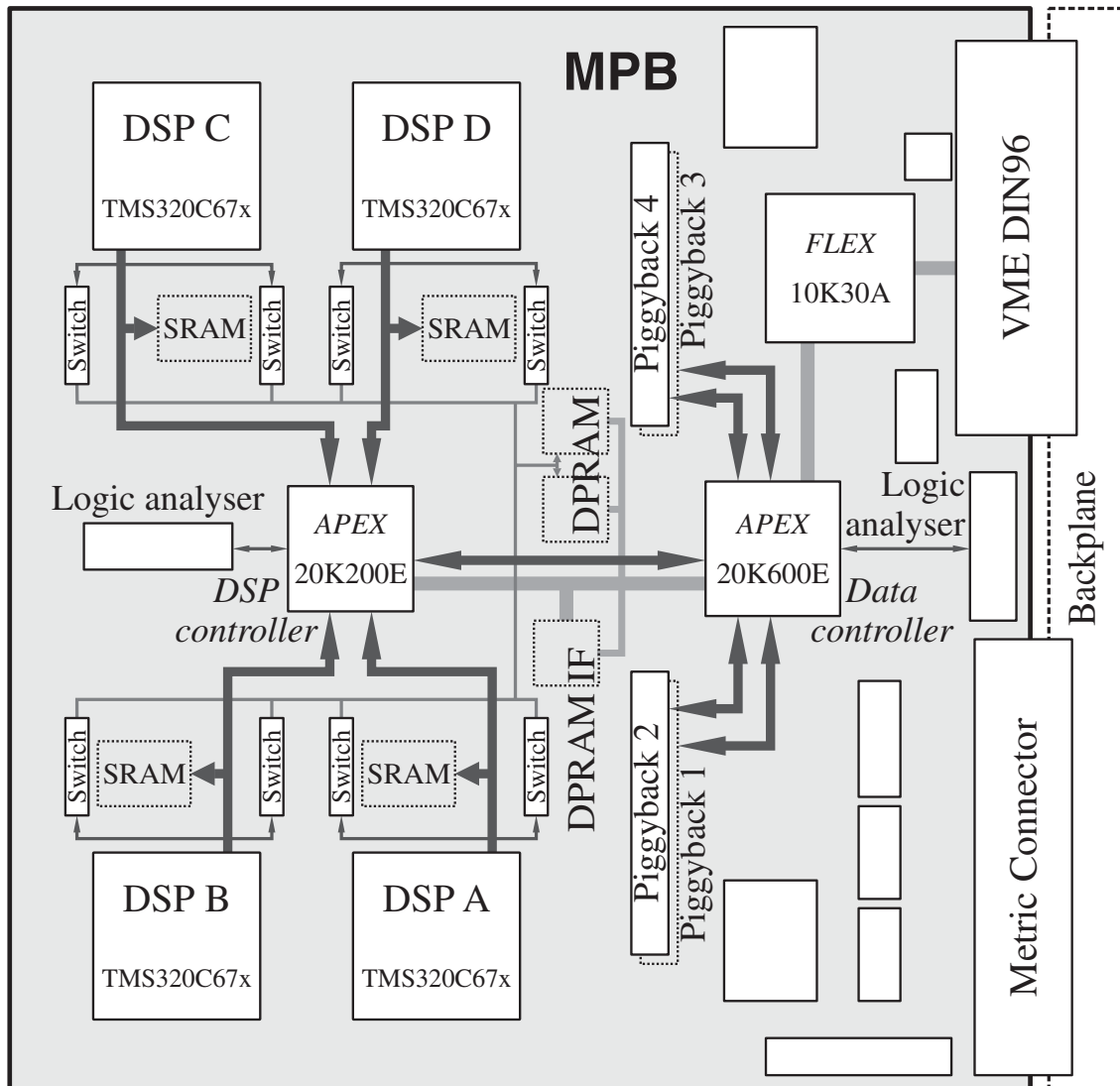


Figure 7.4: Device placement of the MPB. Dotted devices are mounted on the bottom side.

These important timings were checked in several tests. No transmission errors were recorded between FPGAs within the MPB. Figure 7.5 shows the quality of a bidirectional inter-device signal line. The signal has been superimposed several times for a bidirectional signal. In the resulting diagram two superimposed eye diagrams are visible, one for each signal direction. A clear open eye is required for an errorless transmission.

Besides the 104 MHz clock domain, a clock of 41.5 MHz is required for the DSPs. The DSP's core frequency of 166 MHz is derived by an internal phase-locked loop inside the DSP.

The last clock domain is formed by the local bus running with the HERA frequency at 10.4 MHz.

Power supply All devices of the 14-layer PCB board use the low-voltage TTL standard of 3.3 V with exception of some VME devices which are operating at 5 V TTL. The core voltage needed by the APEX FPGAs is 1.8 V. All voltages are supplied by the customized backplane with exception of the DSP core voltage of 1.9 V which is generated on the MPB from the 3.3 V.

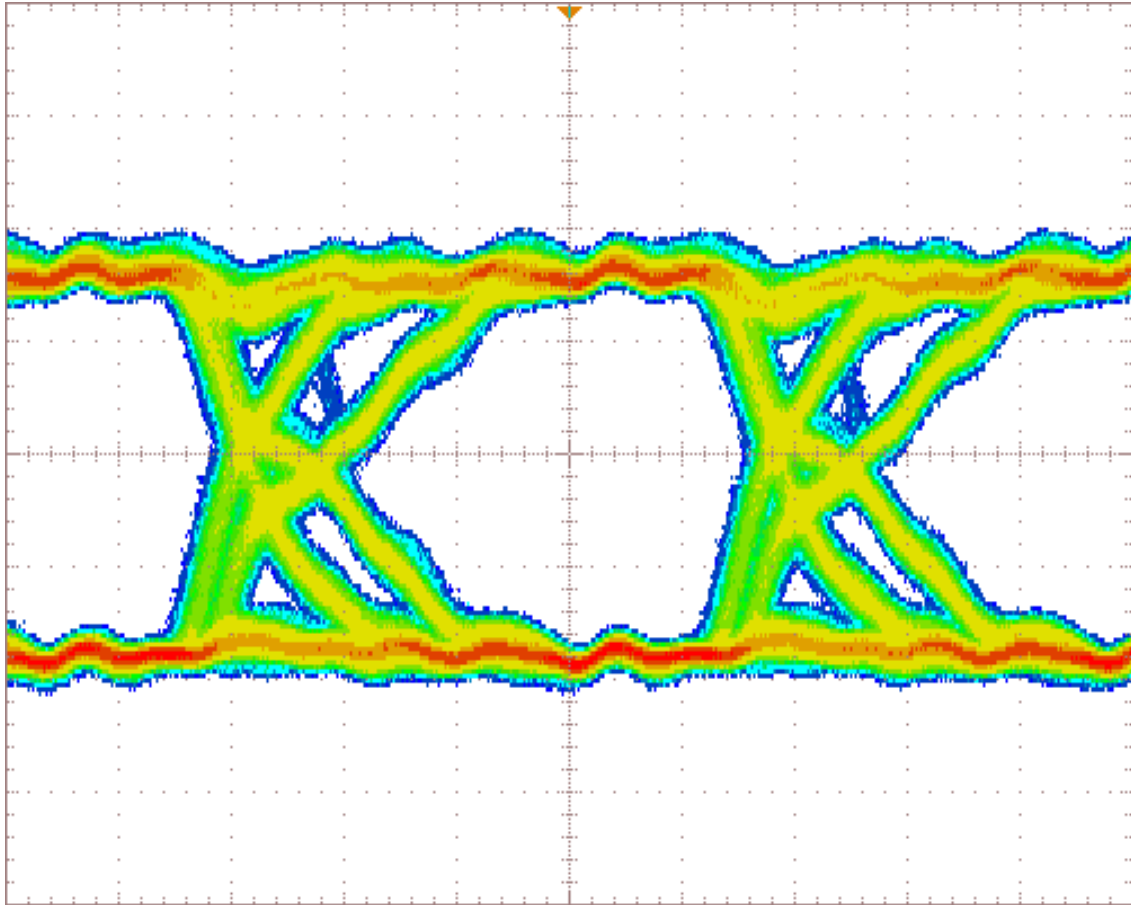


Figure 7.5: Eye diagram of the bidirectional signal between the main board and a piggyback running at a frequency of 104 MHz. The horizontal scale is 2 ns, the vertical 1 V per large division. The picture was taken with a digital oscilloscope running at 25 GSamples/s.

7.2.2 Piggyback cards

The piggyback cards allow for a flexible interfacing of the MPBs with LVDS channel links. Besides the LVDS transmitter and receiver the piggyback is equipped with a small FPGA¹². This FPGA serves as controller and data switch between the LVDS input, the LVDS output and the bidirectional connection to the MPB. The main tasks of the FPGA are the buffering of data coming from different inputs and the distribution of data. Another task is the synchronization of incoming data from the LVDS channel to the MPB clock.

The essential components on the piggyback are the LVDS transmitter¹³ and the LVDS receiver¹⁴. The LVDS transmitter serializes the 48-bit wide input into 8 differential signal lines [78, 79]. Therefore the base clock of 104 MHz is internally increased sevenfold to 728 MHz. Per differential signal line 7 data bits could be sent during one clock cycle but only $48/8 = 6$ bits of input data are available. This over-capacity is used to minimize the short- and long-term DC bias on the signal lines by sending the data bits either unmodified or inverted. An additional DC balance bit which is sent after the six data bits indicates whether the previous six data bits have to be inverted or not. The DC balanced bit is determined by the transmitter from the sign of the continuous sum of data bits with value 1 subtracting the sum of data bits with value 0.

¹²Altera APEX 20K60E

¹³National Semiconductor DS90C387

¹⁴National Semiconductor DS90CF388

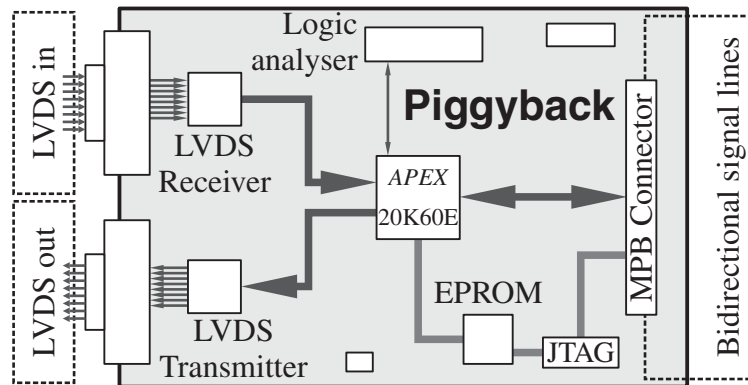


Figure 7.6: Device placement on a piggyback card.

A pseudo random binary sequence (PRBS) was used to test the LVDS channel link. PRBSs with long repetition periods are often used for testing digital hardware communications and in contrast to a real random sequence, their sequence is predictable. The PRBS for the test of the channel link is based on linear feedback shift registers (LFSR). A LFSR consists of n cascaded registers where some of the register outputs are fed back to the input of the first register. As shown in figure 7.7 the output of the registers is connected by XNOR¹⁵ gates to generate the input signal. Depending on the set of tapped registers a LFSR can have a maximal sequence length of $2^n - 1$.

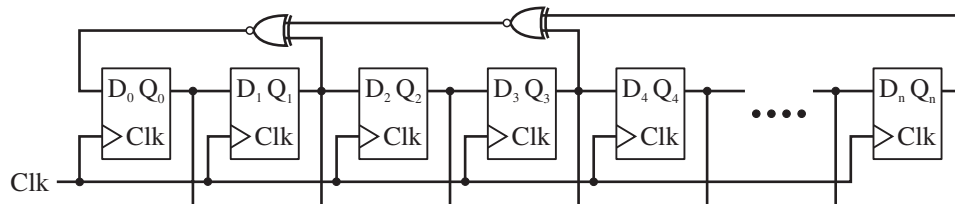


Figure 7.7: A LFSR with feed-back signals tapped from the second, fourth, and last register. The signals are connected by XNOR gates and fed back to the input of the first register.

Note that the state where all registers are set to '1' is always stationary. To build a 48 bit wide LFSR with maximal sequence length the output of the registers 20, 21, 47, and 48 must be tapped [80].

The implementation of a LFSR in the piggyback's FPGA to generate the 48 bit wide PRBS is rather simple. On the receiving side the transmitted word is compared with the correct word, which is determined from previous received words, and eventual bit errors can be counted. The measured bit error rate of the LVDS channel link is better than 10^{-9} s^{-1} under well-defined conditions.

Input-input piggyback Since the merger cards require in total six LVDS input streams per board a variant of the piggyback with two LVDS receivers was also developed. These input-input piggybacks have the LVDS transmitter replaced by a second receiver.

7.2.3 Message system

Within the L2 system of FTT nearly each device (large FPGA or DSP) must have the possibility to send data to other devices. This can be realized by a sophisticated static coding of the end device into all data words which must be interpreted by each intermediate device. But such a

¹⁵The XNOR operator is the inversion of the logical exclusive OR operator

system is inflexible for extensions and has a cumbersome handling in particular during the test phase.

Hence a more flexible message system for the data transfer was realized which is based on channel numbers and routing tables. A channel number is reserved for each required connection between two devices and is part of each data word. Routing tables in intermediate devices help to forward the message to the final destination. In case of a system extension only the routing tables have to be renewed without changing the code of each device. The generation of the routing tables for all devices is automated with the help of a software tool. For the L2 system 512 channels are foreseen which is sufficient to ensure the required flexibility. An example of a routing table implemented in a FPGA is shown in figure 7.8.

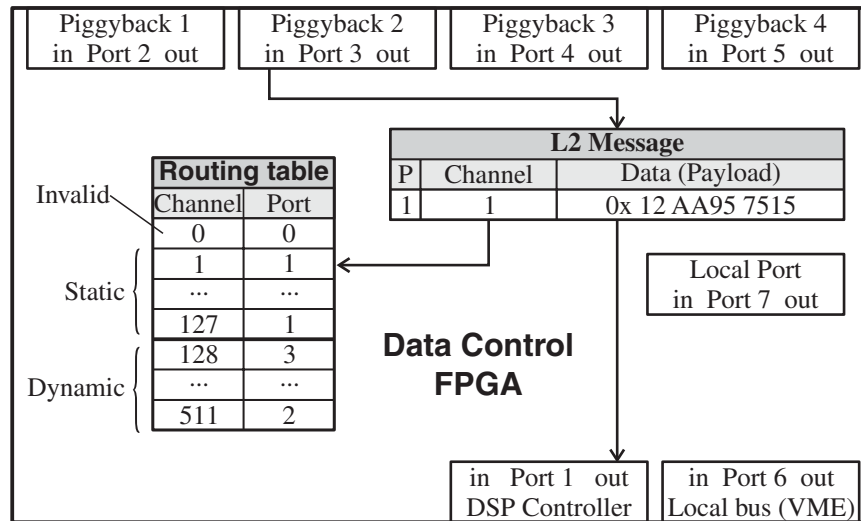


Figure 7.8: Example of a routing table in the Data control FPGA. A message from piggyback 2 is received by port 3 and sent through port 1 to the DSP controller.

The use of the message system is so convincing that it is even used for configuration and writing of the routing tables. Therefore the channel numbers are divided into a static and a dynamic range. The static channel numbers (0–127) are hard-coded in each device and are available at startup. They allow minimal communication and the configuration of the remaining dynamic channels.

A L2 message includes also an additional parity bit which is used to check the consistency of the channel number. The parity bit is set (unset) for an odd (even) number of bits in the channel number. Messages with a wrong channel number are ignored. This ensures a minimal protection against transmission errors.

The transmission security is increased for susceptible messages like writing to the routing table or other configuration by adding a *reply channel* into the data part of the message. After executing the transmitted command, the target device sends a reply message containing a confirmation of the command to the source of the original message using the reply channel. In this way the correct execution of this command on the target device can be reconstructed.

7.3 Hardware for trigger level 3

Track information from the L2 system is distributed within the L3 system by a dedicated receiver board. This ensures that each L3 processor board receives the track information at the same time and is also required to make the system scalable. The L3 system consists of commercial VME processor boards¹⁶ manufactured by Motorola which are equipped with a PowerPC 750 processor running at 450 MHz.

¹⁶MVME2400

Besides the performance and power consumption also the availability, the costs and the quality of documentation were deciding facts to purchase this board. But the crucial factor is the good support of realtime software by the PowerPC. Since the timing demands on L3 are still restrictive only a realtime operation system can be considered. The employed VxWorks realtime operation system from the manufacturer WindRiver supports the Motorola processor board to a large extent.

More details on the L3 processor board and the complete L3 system can be found in [67].

7.4 Key technology

The implementation of the FTT with the given constraints was only possible due to some recent developments in the field of integrated electronics. Of vital importance for the first two trigger levels is the application of FPGAs. With their programmability they offer the flexibility of a processor but still operate with the speed of logic devices. Depending on the size of the FPGA, they can handle up to several 100 input and output pins.

There is a wide range of applications for FPGAs. The following description is restricted to the APEX 20K family of FPGAs [81] which is used on L1 and L2 of the FTT system.

7.4.1 Logic element

A FPGA consists of several thousands of *logic elements*, which is the smallest programmable unit. A functional block diagram of a logic element is shown in figure 7.9. The core of a logic element is

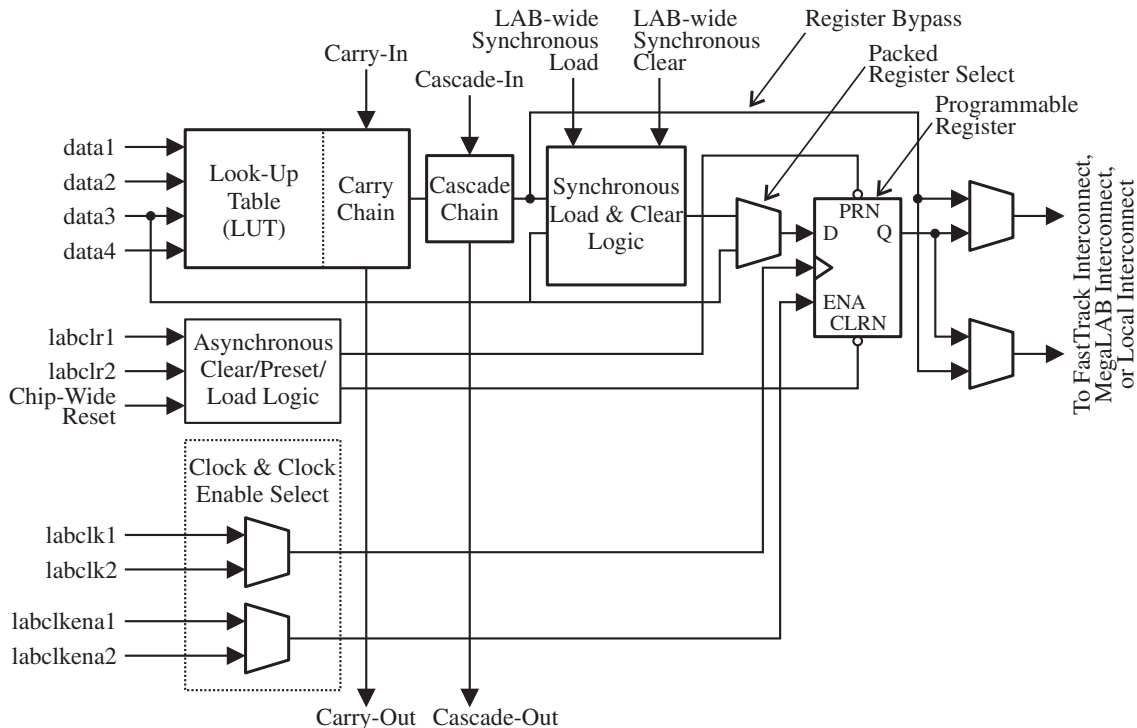


Figure 7.9: Schematic view of a FPGA's logic element [81].

a lookup table (LUT) for each logical combination of the four input signals. If a logical function requires more than four input signals, logical elements must be combined. On the other hand the space is wasted if only three or less input signals are used.

The other important component of a logic element is a register which holds the output of the lookup table for one clock cycle. If required, this register can be bypassed.

Besides these two main components there are elements for clearing the register and combining logic cells of a counter by a carry chain.

7.4.2 Embedded system blocks

The FPGA offers also so-called embedded system (ESB) blocks with a memory structure since logic elements are not the adequate structure to store larger amount of data. A large FPGA has more than 100 ESB while an ESB offers 2kbit of memory. ESBs can be configured for several operation modes like Dual-Ported RAMs or ROMs.

CAMs

The APEX FPGA supports *content addressable memories* (CAMs) which are implemented in ESBs. A CAM can be regarded as inverse RAM where the input patterns are compared with pre-loaded values and matches are indicated by the corresponding address location in a single clock step [82].

CAMs can work in three different APEX specific operation modes. During configuration one of the following operation modes must be selected [83].

Single-match mode In this mode the storage of multiple patterns that match the same input pattern is not allowed; otherwise the CAM will not operate properly. To ensure this when writing a new pattern, the CAM must be checked first if this pattern is already stored. The benefit of this mode is that only one clock cycle is needed to read stored data.

Multiple-match mode To store the same input pattern more than once the multiple-match mode can be used. After searching the CAM for a pattern the first match address is shown after two clock cycles and other match addresses are presented on subsequent cycles. The drawback of this mode is the access time of two clock cycles which makes this mode unusable for pipelined processes. In addition the timing performance is only half as good as in the other modes.

Fast multiple-match mode This mode is identical to multiple-match mode except that the fast multiple-match mode only takes one clock cycle to read. However, this quick generation uses only half of the memory available in each ESB. As a result, only 16 instead of 32 patterns can be stored in a CAM, but data can be read out in one clock cycle.

The combination of a CAM with a RAM can be used to implement lookup tables very efficiently as shown in figure 7.10 [84].

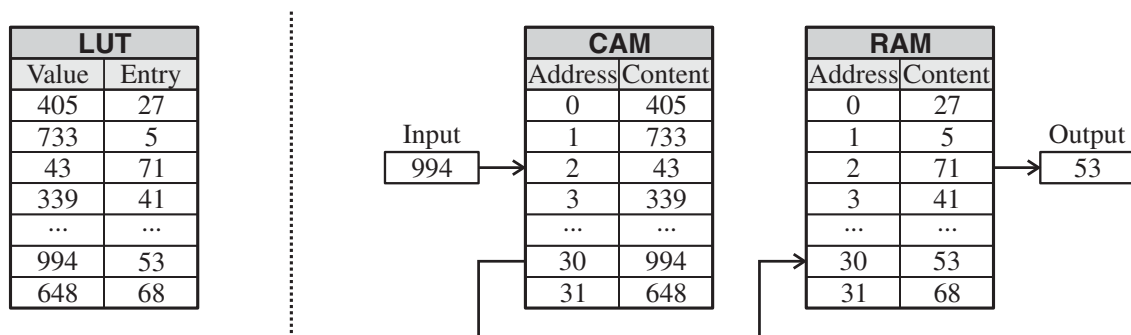


Figure 7.10: Example of a combination of a CAM with a RAM to implement a lookup table LUT.

7.4.3 Phase-locked loops (PLLs)

To modify the clock's frequency and phase relation up to four PLLs are integrated in the FPGA [85]. With help of the PLL almost any frequency in the range of 1.25 MHz to 335 MHz for internal signals can be generated from an input clock. This allows to implement several clock domains within the same FPGA driven by only a single clock. This can be useful to speed up internal algorithms or to synchronize on a slower clock. The PLL even allows to generate a clock signal for external devices.

The other feature of the PLL is to shift the phase relation of the input clock in fine steps which can be combined with a frequency modification. With this skew control it is possible to optimize the setup t_{su} and clock-to-out t_{co} time.

7.4.4 Software tools for developers

This final points merits to be mentioned since all recent developments in this technological field would be worthless if the hardware programmer was not supported by powerful software tools [86]. They allow to formulate an algorithm or a logical function in a high-level programming language and translate them to the gate level of the FPGA. This translation happens together with an optimization of the timing performance and resource usage of the FPGA.

Besides the functional simulation of the algorithm, the timing of the complete FPGA can be simulated. This is absolutely essential to implement complex algorithms running at high clock frequencies. An additional convenience of these software tools is that the bulk of the algorithm can be developed without the presence of the 'real' hardware.

7.5 Overall FTT simulation

A software simulation of the complete FTT system is indispensable to study the efficiency and performance of the FTT during the design phase. For this the software package FTTEMU was written [74]. In a later step this simulation was adapted to be integrated into the existing framework of the H1 detector simulation. FTTEMU is now interfacing the response of the CJC simulation and the simulated analogue CJC signals are used as basic input.

The structure of the software package has a modular layout which is adapted to the hardware implementation. This allows to crosscheck the output of a hardware board with the simulation especially during commissioning of the system. During full operation of the H1 detector it is planned to run FTTEMU in the *verification modus*. For that purpose the FTT trigger decision of real data is compared periodically with the output of the simulation. This allows a simple and comprehensive monitoring of the complete system.

Chapter 8

The L2 Linking Algorithm

Within the L2 system of the FTT the L2 linking algorithm is one of the most complex logic algorithms and is implemented in the Data controller FPGA of the L2 linker board. In this chapter a description of this algorithm is given.

8.1 Functional description of the L2 linker

After a L1Keep signal track segments from the FEMs are collected by the merger cards and sent to the L2 linker board where they are processed by the L2 linker algorithm. The linker algorithm operates in three steps:

Receiving mode The Data Controller receives track segments from trigger layer 1 to 4 and stores them in four 2-dimensional κ - ϕ histograms according to their trigger layer.

Link mode After receiving the last track segment from all trigger layers the real linking process starts. The algorithm searches for correlations in all 4 κ - ϕ histograms which denote a valid combination of track segments. Linked track segments are "encoded" to L2 messages and sent to a L2 fitter card for fitting.

Init Mode After sending the last linked segments the linker algorithm clears the κ - ϕ histograms and is ready for the next L1 Keep signal.

8.1.1 General requirements

Because the track segment finding algorithm on the FEM is limited to 128 track segments per trigger layer, the L2 linker must be able to process the same number of tracks. This number of track segments includes also the mirror hits which are found by the track segment finding algorithm. These mirror hits are a consequence of the ambiguity of the drift direction in the CJC and can only be rejected by a linking algorithm. After the linking process a maximum of 48 linked tracks are provided to the L2 system for fitting. This limit comes from the fact that the 24 DSP can perform the fitting algorithm only twice during the L2 latency.

8.1.2 The κ - ϕ histogram

The κ - ϕ histogram in which the track linking is performed has a resolution of 40 bins in κ and 640 bins in ϕ . This size is adjusted to the resolution of the track segment finder and covers the full available bit range for κ and ϕ .

Besides the center bin the algorithm has also to account for adjacent bins in order to make it independent of binning effects. Starting from a bin (search seed) there are nine possible positions to put a 3×3 sliding window containing this bin. As can be seen in figure 8.1 it is necessary to

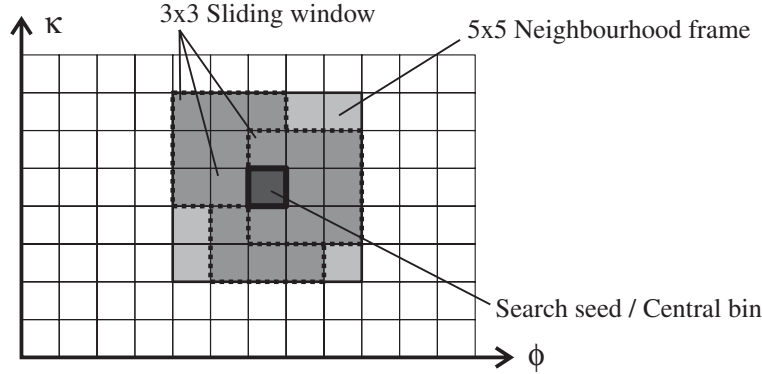


Figure 8.1: Sliding window technique

account for all bins in a 5×5 neighborhood frame around the central bin. Consequently 25 bins must be evaluated at the same time in order to apply the sliding window technique.

It is obvious that a standard way to store and search the four κ - ϕ histograms accounting for more than 100'000 bins is not adequate to the problem. In addition the histograms are only filled with up to 0.5% of all histogram bins even in the worst case of 128 track segments per trigger layer. To handle this the histograms are stored in a compressed and appropriate form which allows a fast parallel and efficient search.

The storage of a 'virtual' κ - ϕ histogram from one trigger layer is based on CAMs which are convenient for fast search algorithms. With this method, information of track segments is written to a *Segment RAM* and is accessible by the address of this RAM. A combination of a CAM with a *Tag RAM* according to section 7.4 is now used as a lookup table (LUT) to give the translation from the κ - ϕ bin number into the address range of the Segment RAM. This configuration is very compact and allows access to the track segment information from a given histogram bin within five clock cycles.

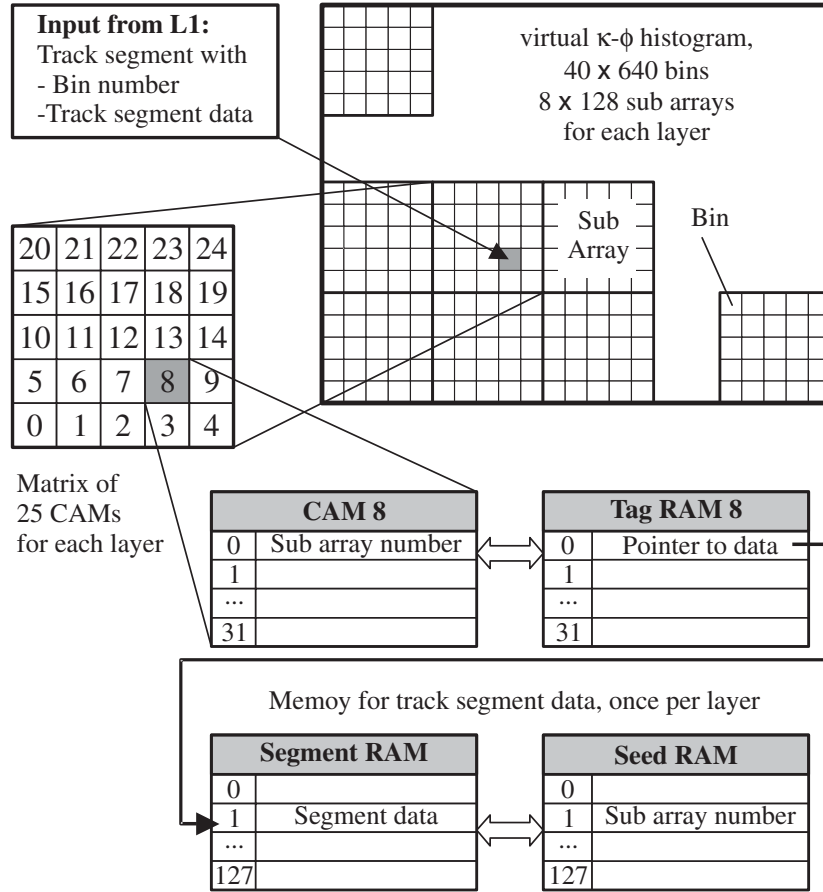
The bin number of each track segment is also written to the *Seed RAM*. In the linking step this list of search seeds is worked off. In principle this redundant information is also available from the Segment RAM. But these two memories must be independently accessible if the algorithm should be fully pipelined.

With this configuration one bin per clock cycle can be searched for. But to apply the sliding window technique as mentioned above, a 5×5 neighborhood must be evaluated. This can only be realized by copying the CAM-Tag RAM structure 25 times since the linking algorithm should be fully pipelined and the complete neighborhood is required to be evaluated within the same clock cycle.

The implementation of 25 CAMs per layer requires a rearrangement of the 'virtual' κ - ϕ histogram. The histogram is divided into arrays of 5×5 bins that form sub-arrays. Each sub-array bin is associated to one CAM as can be seen in figure 8.2. From now on the (κ, ϕ) values are used to label a sub-array. As a consequence the maximum range for κ is $2^3 = 8$ respectively $2^7 = 128$ for ϕ . Track segments from L1 carry κ , ϕ and CAM number which are looked-up in tables during track segment finding. A detailed configuration of the different memories used by the linker is given in appendix B.1.

Figure 8.2 shows how a track segment is written to the virtual κ - ϕ histogram of a trigger layer. The following list describes the requirements when writing track segments to the memory structure.

1. Only the first 128 track segments per trigger layer are considered for the linking algorithm. Additional segments are rejected.
2. If several track segments from one trigger group have the same κ , ϕ , and CAM number only the first segment is stored. This is required by the CAMs which are operated in the 'Single

Figure 8.2: Storage of a track segment in the virtual κ - ϕ histogram.

match mode’.

- Only the first 32 track segments from one trigger layer with the same CAM number can be stored since the CAMs have a depth of 32 entries.
- When writing track segments, an interval of 5 clock cycles is required between two track segments from the same layer and the same CAM number. There are two reasons for this. First, before writing to the corresponding CAM it must be checked if an entry with the same sub array number already exists. If the sub array number of the new track segment is already present in the CAM then this track segment is dropped. The second reason is that writing a sub array number to a CAM takes two clock cycles. This requirement is given by the FPGA architecture.

To ensure a delay of 5 clock cycles for segments with the same CAM number, the stream of incoming track segments must be buffered in a FIFO for each trigger layer. Since the Data controller FPGA has no additional resources to implement these FIFOs, they are displaced to the piggybacks. Consequently, the piggybacks have to guarantee this delay.

The impact on the physical selectivity by these requirements are marginal. The limitation to 128 tracks segments per layer is unimportant for more than 95% of the events. Events with a higher track multiplicity are expected to be triggered by other triggers.

The second limitation to only one track segment per CAM with the same sub array number was simulated assuming an uniform distribution within the κ - ϕ histogram of 128 track segments. The results for this case are shown in table 8.1. About 8 track segments are dropped on average for the

Multiplicity of sub array	1	2	3 or more
Track segments	112.9 ± 5.1	7.1 ± 2.4	0.3 ± 0.5

Table 8.1: Simulated multiplicity of sub array number for 128 track segments. Only the first track segment is considered for segments with a multiplicity larger than 1.

case with maximal segment number. In about half of these cases the wrong segment of a possible track link is rejected. As a consequence the track fit is performed with a wrong track segment. This failure is a general limitation of the algorithm which is related to the finite resolution of the CJC. Nevertheless, the effect of this problem is in the order of percents and will be absorbed in the overall efficiency of the trigger system.

The third limitation to 32 track segments per CAM is negligible since the overflow probability for one CAM is smaller the 10^{-15} for 128 uniformly distributed track segments.

The last requirement has only an impact on the overall timing of the linking step, see section 8.2.3.

8.1.3 Pipelined linking process

Each piggyback card indicates the transmission of the last track segment by an additional control signal. After receiving the *last segment* control signal from all trigger layers the linking process is started.

The first (κ, ϕ) sub array number of the first trigger layer (search seed) is sent to the 25 CAMs of each trigger layer. The matches from all 100 CAMs are entered in the *hit matrix* as shown in figure 8.3.

If the search seed is not in the center bin of a sub array, the sub array number that is used for searching the CAMs must be adapted for each CAM according to its position in the sub array. The search range has to be adapted such that the search seed again is in the center of a 5×5 neighborhood frame. An example of sub array number adaptation is shown in figure 8.4. Special care is needed when adapting the sub array number at the boarder of the κ - ϕ histogram. In contrast to κ boarder, the histogram is cyclically continued at the ϕ boarder.

In the next step the 3×3 sliding window is applied to the hit matrix. A *weighted sum* is calculated for each of the 9 possible positions of the window. It is the sum of all track segments weighted with the *weight matrix* from table 8.2. Only one track segment from each trigger layer

1	2	1
2	4	2
1	2	1

Table 8.2: The weight matrix of a sliding 3×3 window.

may account for the weighted sum. In case of multiple segments within a 3×3 sliding window, the track segment with the highest priority given in table 8.3 is selected. The weighted sum of all

7	4	9
3	1	2
6	5	8

Table 8.3: Priority of track segments from the same trigger layer within a 3×3 sliding window. The track segment in the center of the window has the highest priority.

9 sliding windows are written to the *link quality matrix* (LQM). On the basis of the LQM the link decision is calculated as explained in the next section.

During the calculation and evaluation of the LQM, the additional track segment data is read from the Segment RAM using the Tag RAM as described above. In case of multiple matches of

track segments from one layer, the segment with the highest priority with reference to the search seed is selected. In case of a positive link evaluation the track segments are passed to the message generator and the pipeline of the linking process is terminated.

Already one clock cycle after reading the first search seed from the Seed RAM, the next search seed is read and is passed to the linking process pipeline. In this way all search seeds from all trigger layers are worked off. After the last track segment has left the linking pipeline, all CAMs are cleared and the memory counters are reset to zero.

8.1.4 Evaluation of the link quality matrix

In the previous section the calculation of the link quality matrix (LQM) was explained. In this section now the evaluation of the LQM is described in more detail.

The LQM is representing a 3×3 fraction of the complete κ - ϕ histogram around the seed. The entries of the LQM describe the goodness of a track link with a search seed located in the corresponding bin. The aim of the evaluation step is to search the best link position within this 3×3 histogram fraction according to the values of the LQM. If a minimal link quality is fulfilled and the best link position is identical with the search seed (which is equivalent to the central bin of the 3×3 window) the link is accepted as valid. If the best link position is located in an other bin, the link was or will be found when the search seed is located in this bin.

In the first step the bins of the LQM which have no track segment in the corresponding bin are masked by setting them to 0. This is necessary since even when such bins would have the best LQM value, it can't be found since it has no search seed and therefore must be excluded from the comparison.

Then a link is declared as valid if the following points are satisfied:

- The search seed must be the track segment with the smallest trigger layer number. If not, the link would have been found in a previous step since linking goes from the inner to the outer trigger layer.
- The search seed entry of the LQM must be greater or equal to 5. With the given weight matrix this implies that at least 2 track segments per link are required.
- The search seed value lvs of the LQM is compared with all other values lv_i of the LQM:
 1. $lvs < lv_i$: The link is not valid. A better link may be found when the track segment from bin i is the search seed.
 2. $lvs > lv_i$: The link is valid.
 3. $lvs = lv_i$: Depending on the absolute CAM number of the search seed, the link will be valid or not. Among bins with the same LQM values the bin with the highest CAM number is selected.

8.1.5 Message generator

In case of a valid link, up to four track segments are passed to the message generator within one clock cycle. Since the message generator can only send track segments one by one, the valid track segments must be buffered in FIFOs.

The main task of the message generator is to read one track segment of a linked track from the FIFO and complete it to a L2 message. The message format of a linked track segment is shown in table B.6 of the appendix. Besides track segment information, the message contains also the channel number which is important to route the segment to a dedicated DSP for fitting. The Channel RAM is used as a lookup table for the channel number and ensures the even distribution of track segments among all DSPs. After sending the last segment of a linked track, the lookup pointer of the Channel RAM is increased and the next linked track is worked off.

The generation of messages is completed by sending the *Last segment* message to the L2 system.

8.2 The VHDL implementation

The L2 linking algorithm was programmed using VHDL¹ [87]. A typical production cycle of FPGA code includes the following steps:

- Programming of the FPGA's functionality in a hardware description language like VHDL.
- Functional simulation of the algorithm with a simulation tool.
- Synthesizing of the programmed logic into logical elements which are adapted to the inner structure of the selected FPGA.
- Place and route (fitting) of the synthesized logic in the FPGA. Often the two last steps are performed by the same software from the FPGA manufacturer.

VHDL allows the programming of hierarchical designs based on *entities*. An entity is a self contained design unit which allows to instantiate further entities.

The complete hierarchical design of entities for the data controller FPGA from the L2 linker card is shown in figure 8.5.

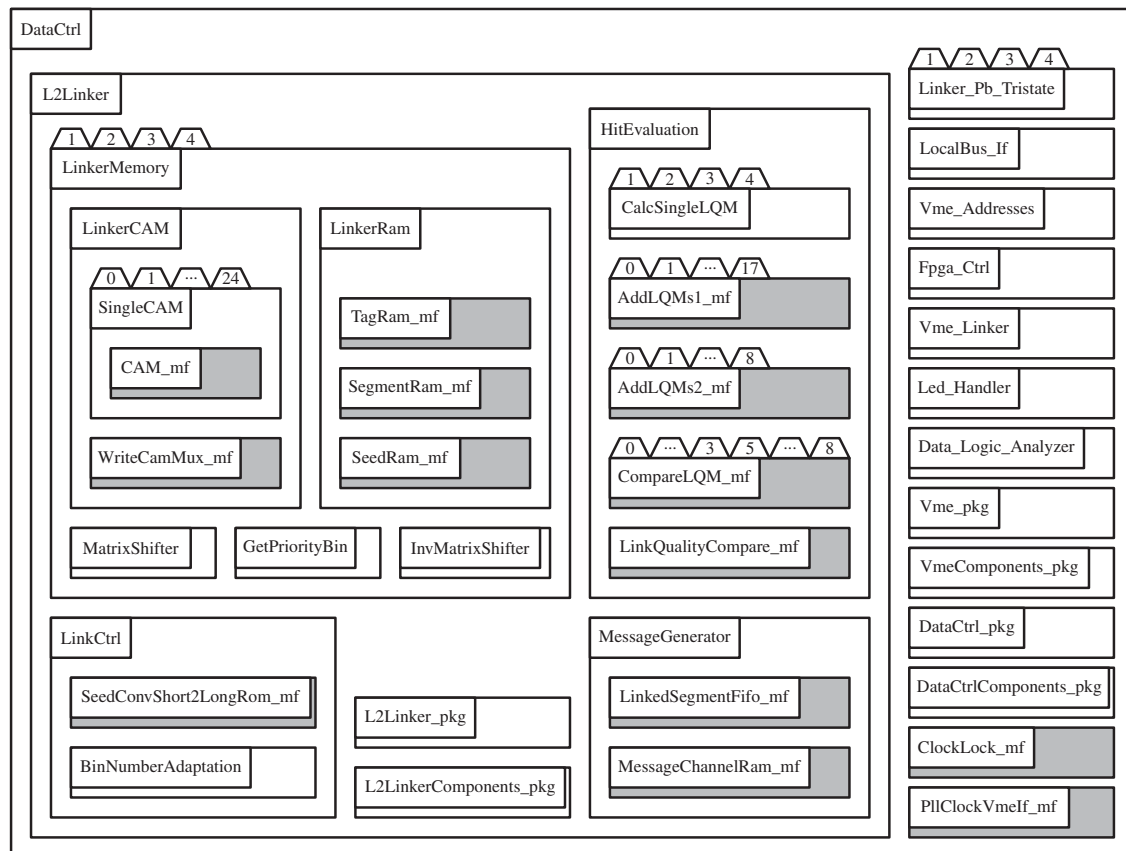


Figure 8.5: Entities of the data controller FPGA of the L2 linker card. Shaded entities are so-called megafunctions which are provided by the FPGA manufacturer.

¹VHSIC Hardware Description Language; VHSIC stands for Very High Speed Integrated Circuits

8.2.1 The core of the L2 linker

The main functionality of the linking algorithm is contained in the *L2Linker* entity and forms the core of the L2 linker. The design of the linker core is shown in figure 8.6 and consists of four parts of which each of them has its corresponding entity described in the following subsections.

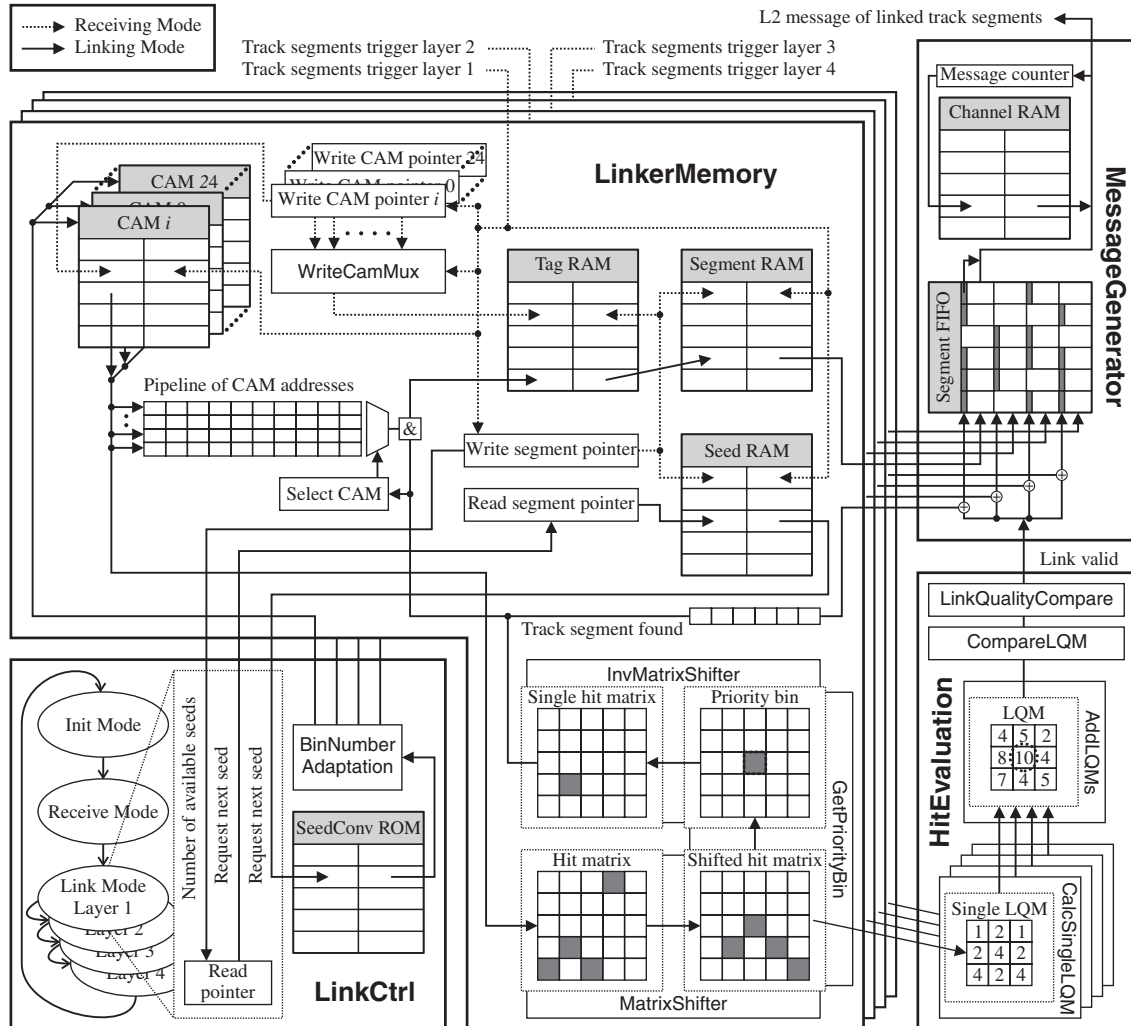


Figure 8.6: Block diagram of the L2 linker core.

Linker memory

This is the main part of the linker core and uses the most resources. It consists mainly of the predefined memory blocks and its control logic. For each trigger layer there is a separate entity.

In the receive mode, track segments from each trigger layer are written to the corresponding memory entity. In a first step the CAM corresponding to the CAM number of the track segment is checked for an already existing entry with the same sub array number. If not, the sub array number is stored in this CAM and the corresponding address pointer is increased. Parts of the track segment information are also written to the Segment and Seed RAM. Finally the lookup relation between the CAM and the RAMs is stored in the Tag RAM.

Since the instance of a Tag RAM associated to a CAM wastes a complete ESB even if less than 10% of the ESB is used, it is more efficient to collect the 25 Tag RAMs in one big Tag RAM.

Such a combined Tag RAM occupies only 4 ESB, see also section B.1.

In the link mode the adapted search seed is presented to all CAMs in all four trigger layers. CAMs with a matching content are marked in a hit matrix while their matching address is stored in a pipeline as long as the CAM with the highest priority in relation to the search seed is found. For this the hit matrix is transformed so that the search seed is in the central bin of the matrix. Then the CAM according to the priority bin (Table 8.3) is selected and finally the matrix is transformed back. Now the CAM with the highest priority is known and the matching address of this CAM can be read from the pipeline. This address is used together with the CAM number to lookup the memory location of the remaining segment data in the Tag RAM.

Link controller

The main task of the link controller is to connect the four memories of each trigger layer and give them a common interface. Besides providing search seeds to all memories this part controls also the operation mode of the linker core. A state machine with six states containing the initialization (init) mode, the receive mode and the four linking modes for each trigger layer controls the functionality of this entity.

In the init mode all CAMs and the pointers containing the addresses of RAMs are cleared. Since writing to the 32 bit deep CAM requires two clock cycles, the complete init modes lasts for at least 64 clock cycles.

In the linking mode the functionality of the link controller is complex. For each layer this entity requests search seeds from the corresponding trigger layer according to the number of available track segments. These search seeds are then presented to all CAMs of the Linker memory. Before that, their sub array number must be adapted according to the position of the search seed in the sub array (section 8.1.3). For this purpose the CAM number is first translated into a binary representation called *long CAM number* which is more appropriate for the bin number adaptation. The long CAM number format is shown in table B.9 of the appendix. The transformation of the search seed's CAM number is implemented as a lookup-table in the SeedConvShort2Long ROM.

Hit evaluation

This part of the L2 linker contains the calculation of the link quality matrix and the evaluation of this matrix as explained in section 8.1.4. The hit evaluation is performed in parallel to the lookup of the track segments in order to keep the pipeline of the linking process short. Since this part requires some mathematical operations many standard functional blocks provided by the manufacturer are used.

The calculation of the LQM is performed by adding the *single LQM* of each trigger layer whereas the single LQM is built up by evaluating the shifted hit matrix of the corresponding trigger layer. In the next step the LQM is examined according to the rules of section 8.1.4 and finally the *link valid* signal is generated for accepted track links.

Message generator

The task of this part is to buffer track segments which are provided simultaneously by the linker memory in a large FIFO and to convert them into L2 messages. The message generator is only active during the linking process.

With every clock cycle up to four track segments of a possible track link are sent from the linker memory to the message generator. The validity of this link is determined by the hit evaluation entity. The latency of looking up track segments and hit evaluation are adjusted so that the link valid signal from the hit evaluation entity is sent to the message generator with the same clock cycle as the track segments from the linker memory.

If the link is valid, the corresponding track segments are written to the Segment FIFO. Instead of four FIFOs for each trigger layer, a larger combined FIFO is used which allows a better usage of ESBs. An additional bit per track segment is also written to the FIFO. This bit is used to indicate if a track segment of the corresponding trigger layer was found.

The message generator converts each track segment buffered in the FIFO into a L2 message which is sent to a piggyback and finally is routed to a DSP for fitting. The channel number of the message is looked-up in the Channel RAM. After sending all track segments of a valid link, the pointer in the Channel RAM is increased by one to read the new channel number of the next DSP.

8.2.2 Peripheral connection

Operation modi of the FPGA

Outside of the L2linker core the *Fpga_Ctrl* entity controls the basic function of the L2 linker core. The L2 linker core can be set to the Init mode, the Receive mode, or the Link mode by this entity. The *Fpga_Ctrl* entity itself operates in three different modes:

- Run mode
- Debug mode
- Command mode

During standard operation (*Run Mode*) the modi of the L2 linker core are automatically set by the trigger signals, control signals, or timeout counters as shown in table 8.4.

L2 linker mode	Condition
Init Mode	Fast Clear
Receive Mode	L1keep
Linking Mode	<i>Last segment</i> signal from all piggybacks or timeout counter after L1keep

Table 8.4: Conditions for switching the L2 linker mode.

Besides the automatic setting of the modi, they can be set by VME commands for test operation (*Debug Mode*). This feature is planned for the commissioning of the system and is useful for debugging.

The *Fpga_Ctrl* entity is also responsible for switching the data bus from/to the piggybacks. In the *Receive Mode* of the L2 linker core, track segments from the L1 part of FTT are received by the piggybacks and are transmitted through the 48 bit wide connector to the data controller FPGA. The data format of unlinked track segments is given in table B.5. Each piggyback receives the unlinked track segments from one trigger layer. Since trigger layer four has twice as many cells than the other layers, an input-input piggyback is needed to handle the two LVDS channel links. To transmit the additional bit of the cell number from layer four, one out of the twelve control lines is used. The assignment of the remaining control lines is given in table B.7.

In the *Link Mode* of the L2 linker core, the direction of the data lines to the piggyback must be switched in order to send the 48 bit wide L2 message. The format of a L2 message containing a linked segment is shown in table B.6. The switching of the bus direction is implemented in the *Linker_Pb_Tristate* entities which are controlled by the *Fpga_Ctrl* entity.

To enable VME communication with the piggybacks the local bus is extended to the FPGA of the piggybacks. For this an additional *Command Mode* is invented. In this mode the data bus is split asymmetrically according to table 8.5 in order to have direct VME access to the piggybacks.

The handling of the command mode and the different linker standard modes are implemented as a state machine in the *Fpga_Ctrl* entity. The state machine is shown in figure 8.7. Switching the states of the standard linker modes is performed automatically in the Run Mode and can be set by hand with a VME command in the Debug Mode. Invoking and leaving the command mode requires always a VME command.

Bits	Content	Direction
47 – 32	VME Address bit 11 – 0	out
33 – 16	Data	out
15 – 0	Reply	in

Table 8.5: Splitting of the piggyback data bus in the command mode

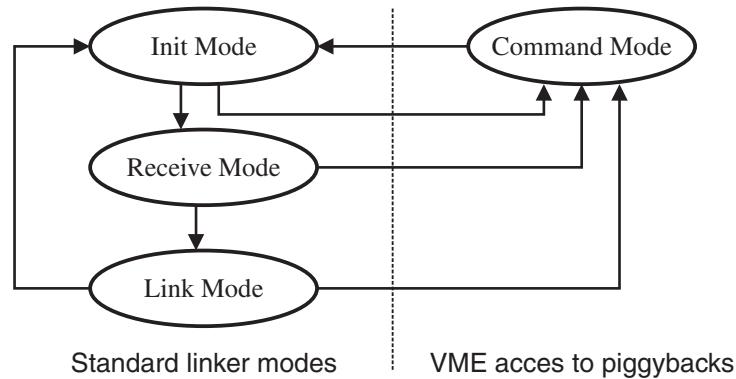


Figure 8.7: State machine of the Fpga_Ctrl entity.

VME control

Since the Data controller is connected to the local bus, VME commands can be used for readout and slow control.

Especially for debugging it is highly desirable to have the possibility to readout the linked track segments by VME. But linked track segments are neither stored in the data control FPGA nor is there additional memory (ESBs) left to store them. Since the DSP controller has no functionality on the L2 linker card it is used to intermediately store the linked track segments. The linked segments are sent on the 48 bit wide data bus to the DSP controller in the same format as used for the transmission to the piggybacks (Table B.6).

On the DSP controller the segments are buffered in a large FIFO from where they can be read by VME. The FIFO is flushed after a Fast clear which is transmitted on a control line. The definition of the remaining control lines between the DSP controller and the data controller is given in table B.8.

8.2.3 Place and route

The complete L2 linking algorithm was successfully implemented in the Data controller FPGA². This FPGA contains 24'320 logic elements of which about 90% are used by the linker design. The usage of the internal Memory (ESB) is shown in table 8.6.

The main demand for place and route is the need to operate the algorithm at the MPB frequency of 104 MHz. This goal is marginally achieved and is mainly limited by the peripheral bidirectional connection to the piggyback cards.

Timing An estimation of the timing for the L2 linking is given in table 8.7. The timing in this table gives an upper limit for the linking time since it is calculated with the maximal possible number of track segments per trigger layer. A more realistic calculation with 20 tracks would reduce the overall timing by a factor of three. In addition the first linked tracks will be already available just after start of the linking process. Anyhow this upper limit for the linker algorithm

²ALTERA APEX EP20K600CF672C7

Memory type	per trigger layer	number of layers	ESBs
CAM	25	4	100
Tag RAM	4	4	16
Segment RAM	3	4	12
Seed RAM	1	4	4
Seed conversion RAM		1	1
Outgoing FIFO		9	9
Message Channel RAM		1	1
Spare		1	9
Total			152

Table 8.6: Usage of embedded system blocks (ESB) in FPGA.

Task	Repetitions	Pipeline	Total steps	time
Receiving track segments	-	3	3	0.03 μ s
Filling memory ³	2×128	3	3	2.6 μ s
Linking process	4×128	15	527	5.27 μ s
Link control		5	5	5.27 μ s
Total	6×128	27	795	7.59 μ s

Table 8.7: Performance of the L2 linker.

is important to give an estimation on the overall timing of the whole L2 FTT system.

Tests of place and routing only the linker core have shown that a frequency of 125 MHz with the same FPGA is possible.

Example of a L2 linker simulation

Figure 8.8 shows the simulation of a linking cycle starting with the receiving of track segments from the four trigger layers. In this simulation some showcase data were used to test the performance of the algorithm. After switching to the link mode the first output is delivered with a delay of 22 clock cycles. This time of 212 ns corresponds to the length of the linking process pipeline. Note that the track segments with the best match to the search seed are always delivered by the linker core even if the link is not valid. The validation of the output is done by an additional *LinkValid* signal. In this example the difference between track 3 and 4 is that the track segment with the highest CAM number comes from different layers. Consequently the link is found when using search seeds from trigger layer 2 respectively 4. Tracks 5 and 6 are located in the adjacent bins. In this case only one track link is found which is a principal limitation of the link algorithm.

³The total latency of the memory filling depends on the order of the CAM number, since a second track segment with the same CAM number must be delayed for at least 5 clock cycles (see also section 8.1.2). Assuming a uniform distribution of the CAM number, a simulation shows that the average value is about 1.36. However, the value of 2 gives a strong upper limit.

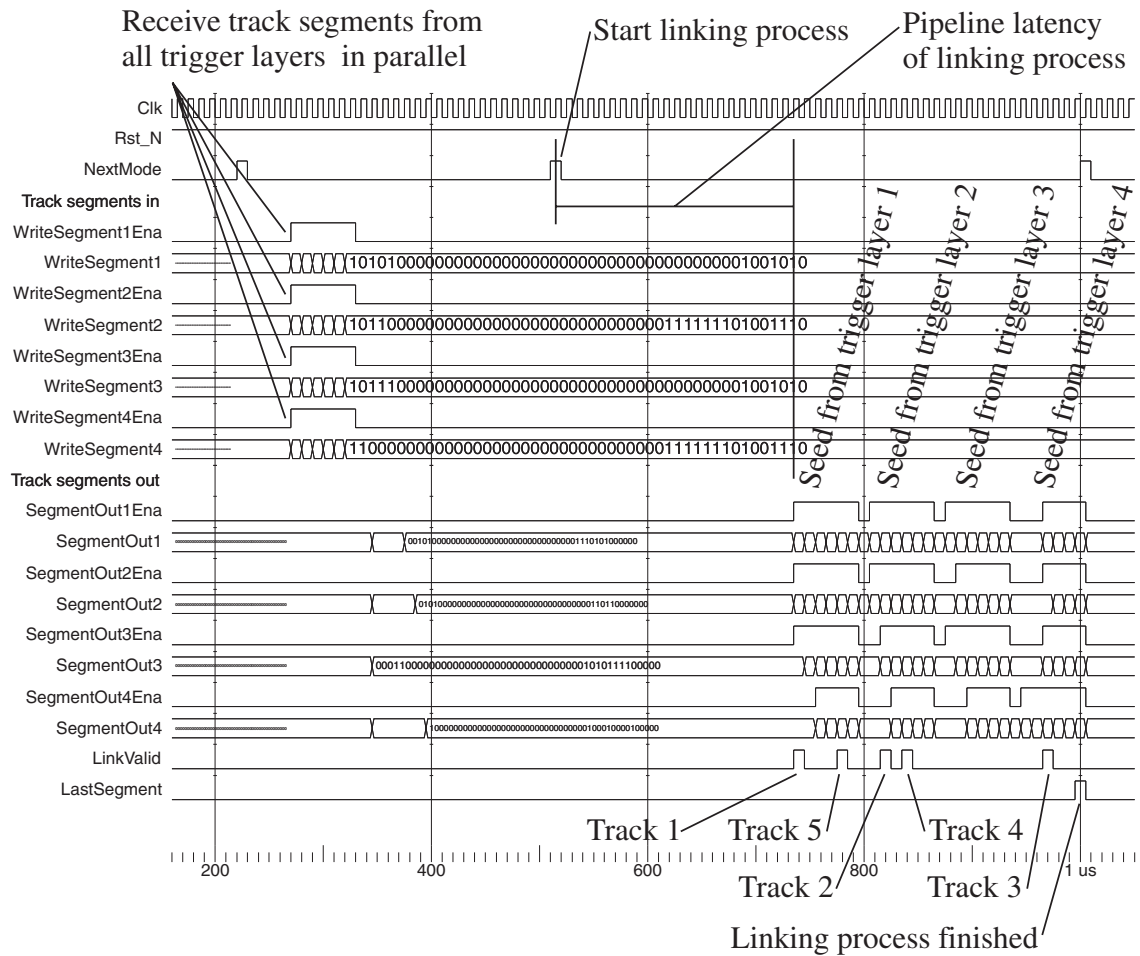
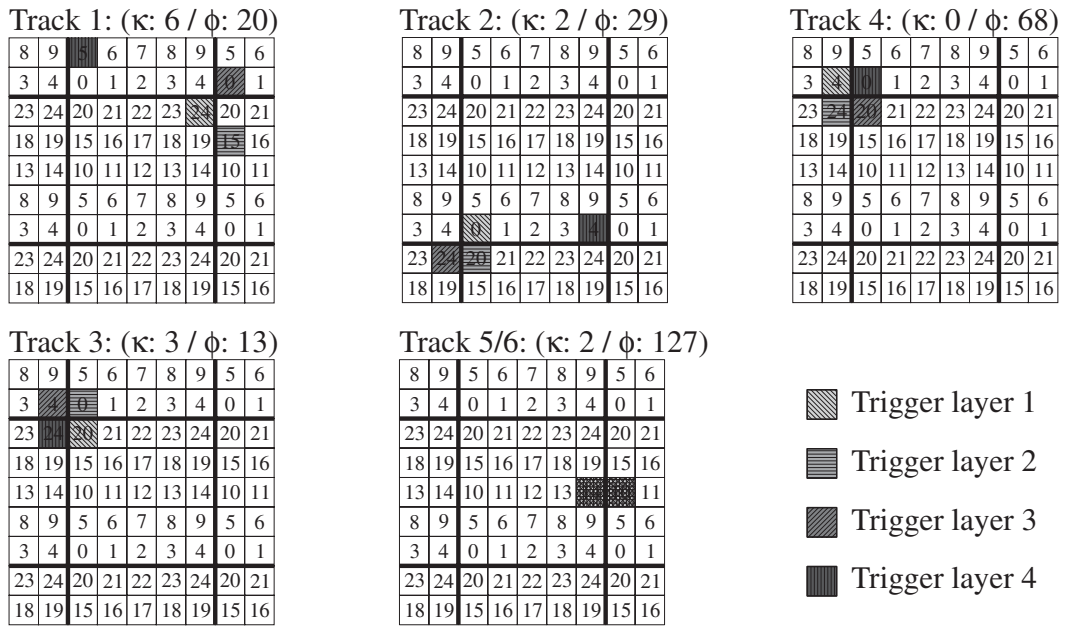


Figure 8.8: Simulation of a L2 linking cycle with some showcase data. This simulation shows some selected signals of the interface to the L2 linker core.

Bibliography

- [1] J. J. Aubert et al., Experimental observation of a heavy particle J, Phys. Rev. Lett. **33**, 1404–1406 (1974).
- [2] J. E. Augustin et al., Discovery of a narrow resonance in $e^+ e^-$ annihilation, Phys. Rev. Lett. **33**, 1406–1408 (1974).
- [3] S. W. Herb et al., Observation of a dimuon resonance at 9.5 GeV in 400-GeV proton-nucleus collisions, Phys. Rev. Lett. **39**, 252–255 (1977).
- [4] W. R. Innes et al., Observation of structure in the Υ region, Phys. Rev. Lett. **39**, 1240–1242 (1977).
- [5] F. Abe et al., Observation of top quark production in $\bar{p}p$ collisions with the collider detector at Fermilab, Phys. Rev. Lett. **74**, 2626–2631 (1995).
- [6] S. Abachi et al., Observation of the top quark, Phys. Rev. Lett. **74**, 2632–2637 (1995).
- [7] S. Eidelman et al., Review of particle physics, Phys. Lett. **B592**, 1 (2004).
- [8] I. Abt et al., The H1 detector at HERA, Nucl. Instrum. Methods **A386**, 310–347 (1997).
- [9] I. Abt et al., The tracking, calorimeter and muon detectors of the H1 experiment at HERA, Nucl. Instrum. Methods **A386**, 348–396 (1997).
- [10] J. Bürger et al., The central jet chamber of the H1 experiment, Nucl. Instrum. Methods **A279**, 217–222 (1989).
- [11] S. Egli, C. A. Meyer, P. Robmann, U. Straumann, P. Truöl, R. Eichler, and R. Holzreuter, The central inner z drift chamber of the H1 experiment, Nucl. Instrum. Methods **A283**, 487–491 (1989).
- [12] K. Müller et al., Construction and performance of a thin cylindrical multiwire proportional chamber with cathode pad readout for the H1 experiment, Nucl. Instrum. Methods **A312**, 457–466 (1992).
- [13] D. Pitzl et al., The H1 silicon vertex detector, Nucl. Instrum. Methods **A454**, 334–349 (2000).
- [14] B. Andrieu et al., The H1 liquid argon calorimeter system, Nucl. Instrum. Methods **A386**, 460–498 (1993).
- [15] R. D. Appuhn et al., The H1 lead/scintillating-fibre calorimeter, Nucl. Instrum. Meth. **A386**, 397–408 (1997).
- [16] H. Bethe and W. Heitler, On the Stopping of fast particles and on the creation of positive electrons, Proc. Roy. Soc. Lond. **A146**, 83–112 (1934).
- [17] F. Halzen and A. D. Martin, *Quarks & Leptons: An introductory course in modern particle physics*, Wiley, 1984.

- [18] Y. L. Dokshitzer, Calculation of the structure functions for deep inelastic scattering and e^+e^- annihilation by perturbation theory in quantum chromodynamics, *Sov. Phys. JETP* **46**, 641–653 (1977), in Russian.
- [19] V. N. Gribov and L. N. Lipatov, Deep inelastic ep scattering in perturbation theory, *Yad. Fiz.* **15**, 781–807 (1972).
- [20] G. Altarelli and G. Parisi, Asymptotic freedom in parton language, *Nucl. Phys.* **B126**, 298–318 (1977).
- [21] S. Frixione, M. L. Mangano, P. Nason, and G. Ridolfi, Improving the Weizsäcker-Williams approximation in electron-proton collisions, *Phys. Lett.* **B319**, 339–345 (1993).
- [22] J. J. Sakurai, Vector meson dominance and high-energy electron proton inelastic scattering, *Phys. Rev. Lett.* **22**, 981–984 (1969).
- [23] E. Witten, Anomalous cross-section for photon - photon scattering in gauge theories, *Nucl. Phys.* **B120**, 189–202 (1977).
- [24] S. Frixione, M. L. Mangano, P. Nason, and G. Ridolfi, Heavy-quark production, *Adv. Ser. Direct. High Energy Phys.* **15**, 609–706 (1998).
- [25] V. M. Abazov et al., A precision measurement of the mass of the top quark, *Nature* **429**, 638–642 (2004).
- [26] S. Frixione, M. L. Mangano, P. Nason, and G. Ridolfi, Heavy quark correlations in photon - hadron collisions, *Nucl. Phys.* **B412**, 225–259 (1994).
- [27] H. L. Lai et al., Global QCD analysis of parton structure of the nucleon: CTEQ5 parton distributions, *Eur. Phys. J.* **C12**, 375–392 (2000).
- [28] M. Glück, E. Reya, and A. Vogt, Parton structure of the photon beyond the leading order, *Phys. Rev.* **D45**, 3986–3994 (1992).
- [29] B. Andersson, G. Gustafson, G. Ingelman, and T. Sjöstrand, Parton fragmentation and string dynamics, *Phys. Rept.* **97**, 31–145 (1983).
- [30] C. Peterson, D. Schlatter, I. Schmitt, and P. M. Zerwas, scaling violations in inclusive e^+e^- annihilation spectra, *Phys. Rev.* **D27**, 105–111 (1983).
- [31] T. Sjöstrand et al., High-energy-physics event generation with PYTHIA 6.1, *Comput. Phys. Commun.* **135**, 238–259 (2001).
- [32] P. Nason and C. Oleari, A phenomenological study of heavy-quark fragmentation functions in e^+e^- annihilation, *Nucl. Phys.* **B565**, 245–266 (2000).
- [33] L. Gladilin, Charm hadron production fractions, hep-ex/9912064, Dec. 1999.
- [34] D. Abbaneo et al., Combined results on b -hadron production rates and decay properties, CERN-EP/2001-050, hep-ex/0112028, June 2001.
- [35] J. Gassner, *A measurement of D -meson production at HERA by decay vertex identification*, PhD thesis, ETH Zürich, Aug. 1998, Diss. ETH No. 14774.
- [36] B. Guberina, S. Nussinov, R. D. Peccei, and R. Rückl, D -meson lifetimes and decays, *Phys. Lett.* **B89**, 111–115 (1979).
- [37] F. Jacquet and A. Blondel, Detection and study of the charged current event, in *Study of an ep facility for Europe*, pages 391–396, Hamburg, Aug. 1979, DESY, Amaldi, U. and others.

- [38] G. Sterman and S. Weinberg, Jets from quantum chromodynamics, *Phys. Rev. Lett.* **39**, 14361439 (1977).
- [39] W. Bartel et al., Experimental studies on multi-jet production in $e^+ e^-$ annihilation at PETRA energies, *Z. Phys.* **C33**, 23 (1986).
- [40] C. Adloff et al., Measurement and QCD analysis of jet cross sections in deep-inelastic positron-proton collisions at \sqrt{s} of 300 GeV, *Eur. Phys. J.* **C19**, 289–311 (2001).
- [41] S. D. Ellis and D. E. Soper, Successive combination jet algorithm for hadron collisions, *Phys. Rev.* **D48**, 3160–3166 (1993).
- [42] S. Catani, Y. L. Dokshitzer, M. H. Seymour, and B. R. Webber, Longitudinally-invariant k_{\perp} -clustering algorithms for hadron-hadron collisions, *Nucl. Phys.* **B406**, 187–224 (1993).
- [43] S. Catani, Y. L. Dokshitzer, and B. R. Webber, The k_{\perp} -clustering algorithm for jets in deep inelastic scattering and hadron collisions, *Phys. Lett.* **B285**, 291–299 (1992).
- [44] S. Frixione and G. Ridolfi, Jet photoproduction at HERA, *Nucl. Phys.* **B507**, 315–333 (1997).
- [45] L. Finke, Untersuchungen zum Erkennen von B-Mesonen im H1-Detektor, Master’s thesis, TH Aachen, May 2003.
- [46] S. German and D. German, Stochastic relaxation, Gibbs distribution, and the Bayesian restoration of images, *IEEE Trans. Pattern Anal. Machine Intell.* **6**, 721–741 (Nov. 1984).
- [47] K. Rose, Deterministic annealing for clustering, compression, classification, regression, and related optimization problems, *Proc. IEEE* **86**(11), 2210–2239 (Nov. 1998).
- [48] P. Billoir, R. Frühwirth, and M. Regler, Track element merging strategy and vertex fitting in complex modular detectors, *Nucl. Instrum. Meth.* **A241**, 115–131 (1985).
- [49] R. Frühwirth, W. Waltenberger, K. Prokofiev, T. Speer, and P. Vanlaer, New developments in vertex reconstruction for CMS, *Nucl. Instrum. Meth.* **A502**, 699–701 (2003).
- [50] R. J. Barlow and C. Beeston, Fitting using finite Monte Carlo samples, *Computer Phys. Comm.* **77**, 219–228 (1993).
- [51] V. Andreev, Acceptance determination of electron tagger (ET44) in 1995, H1 internal note H1-10/96-493, 1996.
- [52] N. Gogitidze and S. Levonian, An offline luminosity determination for the 1995 e^+p data, H1 internal note H1-02/96-471, 1996.
- [53] E. Chabert et al., QBGMAR: An updated PHAN package for cosmic and halo muon topological rejection in high p_T physics analysis, H1 internal note H1-11/98-556, 1998.
- [54] T. Sjöstrand and M. van Zijl, A multiple-interaction model for the event structure in hadron collisions, *Phys. Rev.* **D36**, 2019–2041 (1987).
- [55] O. Kaufmann, *Messung des Zweijet-Wirkungsquerschnitts in Photon-Proton-Kollisionen und Bestimmung der Gluondichte im Photon*, PhD thesis, Uni Heidelberg, Feb. 1999.
- [56] S. Caron, *Jets in photoproduction at HERA*, PhD thesis, TH Aachen, July 2002, DESY-THESIS-2002-035.
- [57] W. Erdmann, *Untersuchung der Photoproduktion von D^* -Mesonen am ep-Speichering HERA*, PhD thesis, ETH Zürich, Jan. 1996, Diss. ETH No. 11441.
- [58] J. Breitweg et al., Measurement of open beauty production in photoproduction at HERA, *Eur. Phys. J.* **C18**, 625–637 (2001).

- [59] S. Chekanov et al., Measurement of beauty production in deep inelastic scattering at HERA, Phys. Lett. **B599**, 173–189 (2004).
- [60] C. Adloff et al., Measurement of open beauty production at HERA, Phys. Lett. **B467**, 156–164 (1999).
- [61] C. Adloff et al., Measurement and QCD analysis of neutral and charged current cross sections at HERA, Eur. Phys. J. **C30**, 1–32 (2003).
- [62] S. Chekanov et al., Measurement of the neutral current cross section and F2 structure function for deep inelastic e^+p scattering at HERA, Eur. Phys. J. **C21**, 443–471 (2001).
- [63] H1 Collaboration, ep physics beyond 1999, H1 internal note H1-10/97-531, 1997.
- [64] J. Becker et al., A first level trigger subsystem CIP2k for the H1 experiment at HERA, Nucl. Phys. Proc. Suppl. **125**, 277–281 (2003).
- [65] M. Urban, J. Becker, S. Schmitt, and U. Straumann, The CIP2k first-level trigger system at the H1 experiment at HERA, IEEE Trans. Nucl. Sci. **50**, 903–908 (2003).
- [66] E. Barrelet, The software L3 triggers in H1, H1 internal note H1-09/88-92, 1988.
- [67] J. Naumann, *Entwicklung und Test der dritten H1-Triggerstufe*, PhD thesis, Uni Dortmund, Dec. 2002, DESY-THESIS-2003-009.
- [68] S. Baird, Addendum to the Proposal "A Fast Track Trigger with high resolution for H1", H1 internal note H1-09/99-576, 1999.
- [69] S. Baird, A Fast Track Trigger with high resolution for H1, H1 internal note H1-06/99-573, 1999.
- [70] A. Baird et al., A fast high resolution track trigger for the H1 experiment, IEEE Trans. Nucl. Sci. **48**, 1276–1285 (2001).
- [71] A. Schöning, A fast track trigger for the H1 collaboration, Nucl. Instrum. Meth. **A518**, 542–543 (2004).
- [72] A. Baird, H. Schultz-Coulon, E. Elsen, Y. H. Fleming, C. Grab, J. Naumann, P. Newman, C. Niebuhr, D. Sankey, A. Schöning, and C. Wissing, A fast track trigger for the H1 collaboration, Nucl. Instrum. Meth. **A461**, 461–464 (2001).
- [73] Y. H. Fleming, *The H1 first level fast track trigger*, PhD thesis, Uni Birmingham, Sept. 2003, DESY-THESIS-2003-045.
- [74] C. Wissing, *Entwicklung eines Simulationsprogramms und Implementierung schneller Spurfitalgorithmen für den neuen H1-Driftkammertrigger*, PhD thesis, Uni Dortmund, Dec. 2002, DESY-THESIS-2003-003.
- [75] V. Karimäki, Effective circle fitting for particle trajectories, Nucl. Instrum. Meth. **A305**, 187–191 (1991).
- [76] N. Berger, Development of a z -vertex trigger based on drift chamber signals at H1, Master's thesis, ETH Zürich, July 2001.
- [77] D. Meer, D. Müller, J. Müller, A. Schöning, and C. Wissing, A multifunctional processing board for the fast track trigger of the H1 experiment, IEEE Trans. Nucl. Sci. **49**, 357–361 (2002).
- [78] S. Poniatowski, High speed transmission with LVDS link devices, Application Note 1059, National Semiconductor, June 1998.

- [79] National Semiconductor, *VHDL Owners's manual*, 2000.
- [80] P. Alfke, Efficient shift registres, LFSR counters, and long pseudo-random sequence generators, Application Note 052, XILINX, July 1996.
- [81] ALTERA, *APEX 20K programmable logic device family*, Mar. 2004, Data sheet.
- [82] Using APEX 20KE CAM for fast search applications, Technical Brief 56, ALTERA, July 1999.
- [83] Using APEX 20KE CAM with the Quartus software design tool, White paper, ALTERA, Feb. 2000.
- [84] Implementing high-speed search applications with Altera CAM, Application Note 119, ALTERA, July 2001.
- [85] Using the ClockLock & ClockBoost PLL features in APEX devices, Application Note 115, ALTERA, Nov. 2003.
- [86] ALTERA, *Quartus II development software handbook*, June 2004.
- [87] P. J. Ashenden, *The designer's guide to VHDL*, Morgan Kaufmann, 1991.

Appendix A

Data analysis

A.1 Definition of the subtrigger 83

In this analysis tagged photoproduction events are selected with the subtrigger 83. This level 1 trigger is a logical combination of trigger elements and is defined as

```
str83 = DCRPh_Tc&&(zVtx_sig:2>1)&&(LU_ET&&!LU_PD_low)&&!CIPB_noSPCLE_T_E1&&  
!VLQToF_BG&&zVtx_TO&&((FToF_IA||FIT_IA)||(!FToF_BG&&!FIT_BG))&&!SPCLE_AToF_E_1.
```

The logical operators used in this definition to concatenate the trigger elements are:

Connector	Logical operator
&&	and
	or
!	negotiation

A trigger element is a logical trigger decision provided by a detector component. The meaning of each trigger element in this definition is explained in the following list:

- **DCRPh_Tc**
At least 3 masks of the $DCr\phi$ trigger have fired. This corresponds to at least 3 tracks with a transverse momentum $p_T \gtrsim 400$ MeV
- **zVtx_sig:2>1**
The histogram of the z -vertex trigger from the proportional chambers must have significance 1.
- **LU_ET**
The energy measured by the electron tagger at $z = -33.4$ m must be in the range of $E_{ET_{low}} < E_{ET} < E_{ET_{high}}$
- **LU_PD_low**
The measured energy of the photon detector $E_{PD} > 6$ GeV
- **CIPB_noSPCLe_ToF_E1**
This TE is composed of **CIP_Backward** and not **SPCLe_ToF_E1**. The composition of this two TE intents to flag beam-gas interactions in the backward region of the detector. Hits in the backward quarter of the CIP with no energy deposition in the SpaCal cannot originate from the nominal interaction region.
- **VLQTOF_BG**
Time-of-flight from the VLQ hits the proton time window.

- **zVtx_T0**
At least one ray is compatible with the nominal interaction region.
- **FToF_IA**
Hit of the forward time-of-flight system in the main proton time window.
- **FIT_IA**
Hit of the forward interacting timing in the proton time window
- **FToF_BG**
Hit of the forward time-of-flight system in the background or late proton satellite time window
- **FIT_BG**
Hit of forward interacting timing in the background or late proton satellite time window
- **SPCLE_AToF_E_1**
The total energy of the AToF of the SpaCal is above threshold 1.

The efficiency of the subtrigger 83 is determined using the subtrigger 80 as reference trigger. The subtrigger 83 is a subset of the subtrigger 80 and is defined as

```
str80 = (LU_ET&&!LU_PD_low)&&!VLQToF_BG&&zVtx_T0&&
((FToF_IA|FIT_IA)|(!FToF_BG&&!FIT_BG)).
```

A.2 Alternative jet cuts on generator level

The loss of events for different jet cuts after reconstruction was studied for events with a jet cut of $E_T^{1(2)} > 4(3)$ GeV and $|\eta_{\text{jet}}| < 2.5$ on generator level. Some of them are summarized in table A.1.

Jet cut after reconstruction $E_T^{\text{jet}1} / E_T^{\text{jet}2}, \eta_{\text{jet}} $	G: \neg R: \neg	G: \surd R: \neg	G: \neg R: \surd	G: \surd R: \surd
5 GeV / 4 GeV, 1.5	87.792%	7.836%	1.104%	3.269%
6 GeV / 5 GeV, 1.5	88.742%	9.628%	0.153%	1.476%
7 GeV / 6 GeV, 1.5	88.876%	10.402%	0.019%	0.703%
8 GeV / 6 GeV, 1.5	88.887%	10.558%	0.009%	0.546%
8 GeV / 7 GeV, 1.5	88.892%	10.746%	0.004%	0.358%
9 GeV / 7 GeV, 1.5	88.894%	10.816%	0.002%	0.288%
8 GeV / 6 GeV, 1.0	88.893%	10.849%	0.003%	0.255%
9 GeV / 8 GeV, 1.5	88.895%	10.902%	0.001%	0.202%
9 GeV / 7 GeV, 1.0	88.895%	10.968%	0.001%	0.136%
9 GeV / 8 GeV, 1.0	88.895%	11.012%	0.001%	0.092%

Table A.1: Accepted events for several jet cuts after reconstruction compared with a cut at generator level of 4/3 GeV and $|\eta| < 2.5$. G: generator level, R: after reconstruction, \neg : event rejected, \surd : event accepted

Appendix B

Technical specification of the FTT L2 linker

B.1 L2 linker memory

In this appendix a detailed layout of the L2 linker memory structure is given. The description follows the linking step for one trigger layer.

The L2 linker algorithm starts with the first entry of the Seed RAM (Tab. B.1). The 16 bit wide memory contains the (κ, ϕ) sub array number and the CAM number cs of the seed. The

Seed RAM (1 ESB)	
Address	Content (15 bits)
0	
...	
$s_6 s_5 s_4 s_3 s_2 s_1 s_0$	$\phi_6 \phi_5 \phi_4 \phi_3 \phi_2 \phi_1 \phi_0 \kappa_2 \kappa_1 \kappa_0 cs_4 cs_3 cs_2 cs_1 cs_0$
...	
127	

Table B.1: Configuration of the Seed RAM.

CAM number cs is later needed for transforming the 5×5 search window and selecting the closest entry to the seed.

The (κ, ϕ) sub array number from the Seed RAM is presented to all CAMs (Tab. B.2) in all trigger layers. An additional bit v is required to mark a valid entry in the CAM and to distinguish it from empty entries. All 25 CAMs provided the location a in the CAM if the corresponding

CAM $c_4 c_3 c_2 c_1 c_0$ (25×1 ESB)	
Address	Content (11 bits)
0	
...	
$a_4 a_3 a_2 a_1 a_0$	$v \phi_6 \phi_5 \phi_4 \phi_3 \phi_2 \phi_1 \phi_0 \kappa_2 \kappa_1 \kappa_0$
...	
31	

Table B.2: Configuration of a CAM.

(κ, ϕ) sub array number was existing. For further lookup the output of the CAM c closest to the seed CAM cs is selected according to a fixed priority matrix (Table 8.3). A depth of 32 entries for each CAMs should be sufficient even if there is a small possibility of overflow. Assuming a

random distribution of 128 track segments within a (κ, ϕ) sub array, the overflow probability for one CAM is smaller than 10^{-15} . Supernumerous track segments of a CAM are dropped. Also dropped are track segments with same (κ, ϕ) sub array since each CAM can contain a concrete (κ, ϕ) sub array number not more than once. This limitation is required to let the CAM work in the single-match-mode.

The Tag RAM address is builded up from the selected CAM number c and its location a . With the content t of the Tag RAM (Tab. B.3) the remaining segment data is accessible. In principle

Tag RAM (4 ESB)	
Address	Content (7 bits)
0	
...	
$c_4c_3c_2c_1c_0 a_4a_3a_2a_1a_0$	$t_6t_5t_4t_3t_2t_1t_0$
...	
799	

Table B.3: Configuration of the Tag RAM.

a Tag RAM for every CAM is needed. Since such a Tag RAM requires less than 10% of an ESB it is more efficient to merge them into a common Tag RAM for all CAMs.

For the track fitting the cell number C , the drift time d , and the z -position for each of the three wire (z^3, z^2, z^1) is required. This information is accessible in the Segment RAM (Tab. B.4) at address t . The combination of 3 ESB could allow to use up to 48 bits per track segment. Even

Segment RAM (3 ESB)	
Address	Content (34 bit)
0	
...	
$t_6t_5t_4t_3t_2t_1t_0$	$C_5C_4C_3C_2C_1C_0 d_9d_8d_7d_6d_5d_4d_3d_2d_1d_0 z_5^3z_4^3z_3^3z_2^3z_1^3z_0^3 z_5^2z_4^2z_3^2z_2^2z_1^2z_0^2 z_5^1z_4^1z_3^1z_2^1z_1^1z_0^1$
...	
127	

Table B.4: Configuration of the Seed RAM.

if κ , ϕ , and CAM number c of a track segment is not required for track fitting it could be useful for debugging to store them also in the Segment RAM since it can be read by VME.

B.2 Assignment of data and control lines

Bits	Content
47 – 43	Cell number
42 – 38	CAM bin number
37 – 35	κ bin number
34 – 28	ϕ bin number
27 – 18	Drift time
17 – 12	z -coordinate wire 3
11 – 6	z -coordinate wire 2
5 – 0	z -coordinate wire 1

Table B.5: Data format of unlinked track segments. The most significant bit of the cell number is decoded by the piggy back and transmitted by a control line. Since track segments from different layers are sent over different LVDS channels no indication of the trigger layer is required.

Bits	Content
47	Parity of channel number
46 – 38	Channel number
37 – 33	Cell number
31 – 30	Track segment counter
29 – 28	Trigger layer
27 – 18	Drift time
17 – 12	z -coordinate wire 3
11 – 6	z -coordinate wire 2
5 – 0	z -coordinate wire 1

Table B.6: Data format of L2 messages containing linked track segments.

Signal name	Function	Port name	Port name PB x
PB x \rightarrow DataCtrl			
PB x _CTRL0	Cell MSB	PB x _CTRL_IN0	PB_CTRL_OUT0
PB x _CTRL1	PB not ready	PB x _CTRL_IN1	PB_CTRL_OUT1
PB x _CTRL2	Lvds A not connected	PB x _CTRL_IN2	PB_CTRL_OUT2
PB x _CTRL3	Lvds B not connected	PB x _CTRL_IN3	PB_CTRL_OUT3
PB x _CTRL4	Data enable	PB x _CTRL_IN4	PB_CTRL_OUT4
PB x _CTRL5	No more segments	PB x _CTRL_IN5	PB_CTRL_OUT5
DataCtrl \rightarrow PB x			
PB x _CTRL6	Reset	PB x _CTRL_OUT0	PB_CTRL_IN0
PB x _CTRL7	Trigger mode	PB x _CTRL_OUT1	PB_CTRL_IN1
PB x _CTRL8	L2 bit	PB x _CTRL_OUT2	PB_CTRL_IN2
PB x _CTRL9	Clear	PB x _CTRL_OUT3	PB_CTRL_IN3
PB x _CTRL10	Bus direction from PB	PB x _CTRL_OUT4	PB_CTRL_IN4
PB x _CTRL11	Data enable	PB x _CTRL_OUT5	PB_CTRL_IN5

Table B.7: Assignment of the control lines between the piggyback card x ($x = 1, 2, 3, 4$) and the data controller.

Signal name	Function	Port name	Port name DspCtrl
DspCtrl → DataCtrl			
FPGA_CTRL0	DspCtrl not ready	FPGA_CTRL_IN0	FPGA_CTRL_OUT0
FPGA_CTRL1	Data enable	FPGA_CTRL_IN1	FPGA_CTRL_OUT1
FPGA_CTRL2	Serial data	FPGA_CTRL_IN2	FPGA_CTRL_OUT2
DataCtrl → DspCtrl			
FPGA_CTRL3	DataCtrl not ready	FPGA_CTRL_OUT0	FPGA_CTRL_IN0
FPGA_CTRL4	Data enable	FPGA_CTRL_OUT1	FPGA_CTRL_IN1
FPGA_CTRL5	Pipeline enable	FPGA_CTRL_OUT2	FPGA_CTRL_IN2
FPGA_CTRL6	Fast clear	FPGA_CTRL_OUT3	FPGA_CTRL_IN3
FPGA_CTRL7	Error enable	FPGA_CTRL_OUT4	FPGA_CTRL_IN4

Table B.8: Assignment of the control lines between the DSP controller and the data controller.

B.3 Long search seed format

20	21	22	23	24
100 000	100 001	100 010	100 011	100 100
15	16	17	18	19
011 000	011 001	011 010	011 011	011 100
10	11	12	13	14
010 000	010 001	010 010	010 011	010 100
5	6	7	8	9
001 000	001 001	001 010	001 011	001 100
0	1	2	3	4
000 000	000 001	000 010	000 011	000 100

Table B.9: Binary representation of the CAM number in the *long CAM number* format. The upper number indicates the CAM number in decimal representation.

Danksagung

Diese Arbeit wurde erst durch die Zusammenarbeit mit verschiedenen Leuten am DESY, an der ETH sowie in der Firma SCS ermöglicht. Ihnen allen gilt mein Dank. Im folgenden möchte ich jedoch einige hervorheben, die zum Gelingen der Arbeit einen besonderen Beitrag geleistet haben.

Grosser Dank geht an meinen Doktorvater Ralph Eichler, der mir diese Arbeit ermöglichte, mich stets unterstützte und mir die nötige Freiheit gewährte. Er war auch der Initiator der unkonventionellen Lösung für meinen Arbeitseinsatz in der Privatwirtschaft, welcher für mich eine interessante und lehrreiche Zeit war.

Für Detailfragen zum H1 Experiment stand mir Christoph Grab mit seinem fundierten Wissen zur Verfügung. Er leistete auch die entscheidenden Beiträge zur analytischen Rechnung. Bei technischen Fragen zur Analyse konnte ich mich immer an Wolfram Erdmann wenden und ich konnte viel von seiner Erfahrung im Vertexing profitieren. Benno List leistete mir Hilfe bei der Programmierung und gab auch zur Analyse entscheidende Hinweise. Salvatore Mangano, meinem Bürokollegen auf dem Hönningerberg, danke ich für die hilfreichen Diskussionen und die angenehme Zusammenarbeit. Zusammen mit ihm und den anderen Doktorandenkollegen Simon Baumgartner und Markus Bischofsberger verbrachten wir auch ausserhalb der Arbeitszeit gesellige Stunden.

Im FTT Projekt war André Schöning in Funktion des Projektleiters ein unermüdlicher Motivator. Er hat meine Leidenschaft für dieses Projekt geweckt und dank seinen kreativen Lösungen war er auch in schwierigen Situationen ein geschätzter Diskussionspartner. Die Zusammenarbeit mit Niklaus Berger, der nun in Hamburg einen Teil meiner Arbeit weiter führt, hat von Anfang an geklappt. Dank geht auch an die beiden Mitarbeiter David Müller und Jörg Müller bei der SCS, die mich sofort in ihr Team integriert haben. Sie haben mir viel Wissen in der Hardwareentwicklung und -programmierung vermittelt. An dieser Stelle möchte ich auch Anton Gunziger erwähnen, der mit seiner wertschätzenden Art sowie seinen innovativen Ideen ein angenehmes Arbeitsklima geschaffen hat.

Für die Bereitschaft zur Begutachtung dieser Arbeit danke ich meinem Korreferenten Günther Dissertori.

Auch meiner Familie und insbesondere Astrid Berger möchte ich meinen herzlichen Dank für die konsequente Unterstützung während den letzten Jahren aussprechen. Ihr entgegengebrachtes Verständnis ist nicht selbstverständlich und gab mir Rückhalt und Motivation.

Curriculum Vitae

Personal Data

Full Name David Martin Meer
Date of Birth April 10, 1973
Place of Birth Bern (Switzerland)
Nationality Swiss, citizen of Eriswil (BE)

Education

1980 – 1984 Primarschule Steinenbrünnen / BE
1984 – 1986 Sekundarschule Schwarzenburg / BE
1986 – 1988 Progymnasium Köniz / BE
1988 – 1993 Gymnasium Köniz / BE, Maturitätstypus C
1993 – 2000 Studies of physics at the Swiss Federal Institute of Technology (ETH)
in Zurich
2000 Diploma in physics at the ETH Zurich. Title of the thesis:
“Bau und Messen eines Multichip Pixelmoduls als Prototyp für den CMS-Tracker”
2000 – 2004 Graduate education in experimental particle physics at the ETH Zurich

Military service

1993 Rekrutenschule
1996 Unteroffiziers- und Offiziersschule
1998 Practical service as officer